

Nonlinear Oscillations of Supernova Neutrinos

A thesis submitted to the
Tata Institute of Fundamental Research, Mumbai
for the degree of
Doctor of Philosophy in Physics

by

Basudeb Dasgupta

Department of Theoretical Physics, School of Natural Sciences

Tata Institute of Fundamental Research, Mumbai

April 21, 2009

Declaration

This thesis is a presentation of my original research work. Wherever contributions of others are involved, every effort is made to indicate this clearly, with due reference to the literature, and acknowledgement of collaborative research and discussions.

The work was done under the guidance of Professor Amol Dighe, at the Tata Institute of Fundamental Research, Mumbai.

Basudeb Dasgupta

In my capacity as supervisor of the candidate's thesis, I certify that the above statements are true to the best of my knowledge.

Professor Amol Dighe

April 21, 2009

Acknowledgements

As I submit this thesis, I feel compelled to express my gratitude to many people. Foremost, I gratefully acknowledge the guidance and support that I have received from Prof. Amol Dighe, my thesis advisor. I also thank my collaborators for a pleasant and satisfying experience of working together.

I would like to express my gratitude to my teachers from Jadavpur University who inspired me to study physics. The faculty at TIFR have all been very helpful and friendly and I thank them for enjoyable and exciting courses, and stimulating discussions. Thanks are due to the DTP office staff and the institute administration staff for their help and unsurpassable efficiency in sorting out every trouble I took to them.

I acknowledge the financial support received from Max Planck India Partner Group and from TIFR.

I also wish to take this opportunity to convey my love and regards for my parents and my brother. Without their encouragement I could not have come this far. And finally, my heartfelt gratitude to all my friends, who made these years absolutely delightful.

Foreword

The cosmos has remained a favorite laboratory to test the laws of fundamental physics - tests of the laws of gravity being the most well-known example. However, over the last century we have progressed from merely charting the gross motion of astrophysical objects, to observing more subtle phenomena associated with them. Many of these phenomena depend crucially on the laws of particle physics. As a result, astrophysics and particle physics are now connected more intimately than ever, with a promise to yield valuable insights into the laws of Nature. Neutrinos, being ubiquitous and weakly interacting, explore regions that are out of bounds to other particles, and are an ideal candidate to probe this deep connection.

Our knowledge of neutrinos has seen a revolution of sorts in the last few decades, thanks to a number of experiments on atmospheric, solar and terrestrial neutrinos. These experiments lead us to believe that there are three flavors of massive neutrinos ν_e , ν_μ and ν_τ which are related to the mass eigenstates by the leptonic mixing matrix. As a result, they can transform into each other through neutrino oscillations. Precision measurement of neutrino masses and mixing parameters is an active area of research and much progress is expected in the years to come.

The detection of astrophysical neutrinos, i.e. neutrinos from supernovae, active galactic nuclei etc., is expected to lead to deep insights into astrophysical processes and particle physics. Similarly, neutrinos from the all-pervading cosmological relic neutrino background, which owing to their extremely low energies are practically impossible to observe directly and only indirectly probed through measurements of the cosmic microwave background radiation, will reveal facets of the large scale structure and evolution of the Universe.

Among astrophysical sources of neutrinos, supernovae stand out, literally by virtue of their brilliance. During a supernova core-collapse, the star emits almost all of its gravitational binding energy into neutrinos, over a duration of a few seconds. The luminosity in neutrinos, for the duration of the burst, outshines the optical emission from all other stars in the galaxy. These neutrinos, that arrive a few hours before the explosion is seen optically, could serve as an early warning signal for astronomers. It is expected that the high statistics neutrino signal from a future galactic supernova will allow detailed studies of the emitted neutrinos. Such a study could reveal the pattern of neutrino masses, necessary to reconstruct the neutrino mass matrix and its possible underlying symmetries. The supernova neutrino signal may also allow us to probe the leptonic mixing angle θ_{13} that determines the strength of the CP violation effects in neutrino oscillations. These are some of the frontier goals of the neutrino physics community, and are believed to be an important step towards identifying the nature of physics beyond the Standard Model. Moreover, one may observe time-dependent signatures of turbulence and shock-wave propagation in the stellar matter and thus monitor the explosion mechanism in real-time. These measurements are likely to shed light on a problem that has eluded astrophysicists for a very long time, i.e. how do supernovae explode? Supernova cores are also a probable site for the synthesis of heavier nuclei, and neutrino observations could be useful to test such a possibility. An interplay between supernova neutrinos and cosmology can be investigated in the context of the diffuse neutrino background coming from all past core-collapse supernovae in the Universe. This diffuse supernova neutrino signal is sensitive to the supernova rate, closely related to the cosmic star formation rate which is an essential probe of the evolution of galaxies and the Universe.

Supernova neutrinos have thus been a topic of interest for physicists and astrophysicists alike. A satisfactory understanding of neutrino flavor conversion in supernovae will be necessary to correctly predict and interpret many of these observations. Previous studies on this subject took into account neutrino oscillations and their resonant flavor conversions in the stellar mantle. It was assumed that neutrino-neutrino interactions are too feeble to be important. However, recent studies indicate that this assumption is not generally true. The neutrino density itself is very large

near the supernova core, leading to extremely drastic effects. It is unavoidable to include neutrino-neutrino interactions which give the neutrinos an additional “effective mass” through elastic forward scattering off other neutrinos. The effective mass is flavor-dependent, since it depends on the flavor of the other background neutrinos. This gives rise to nonlinear neutrino oscillations, by coupling the flavor histories of all neutrinos and antineutrinos. The nonlinear oscillations manifest themselves in various ways, depending on the initial conditions, and have a rich phenomenology. The study of neutrinos from these astrophysical sources therefore demands careful consideration of these nonlinear effects.

In this thesis, we put forward a framework to study nonlinear flavor oscillations of neutrinos. This concerns astrophysical neutrinos in general, but we concentrate mainly on neutrinos from a galactic core-collapse supernova where these effects are the most complicated and interesting. A large body of recent work has been devoted to understanding the rich and complex behavior of the nonlinear neutrino oscillations, near the supernova core. It is evident that these effects significantly modify the spectra of emerging neutrinos. Building on the insights gained from these recent studies, we develop a complete three-flavor framework, including the effects of non-sphericity of the source, and predict the flavor evolution. This treatment is largely independent of supernova phenomenology and applies equally well to dense ensembles of neutrinos elsewhere, e.g. neutrinos in the early Universe or neutron star mergers. We discuss phenomenological implications of nonlinear oscillations for supernova neutrinos and show that these effects occurring deep inside the supernova leave unmistakable signatures in the emerging neutrino spectra. We claim that it could allow a determination of the pattern of neutrino masses even at vanishingly small θ_{13} , thought to be a very challenging task otherwise. We show that the nonlinear effects depend on the progenitor in the early stages of the explosion, and speculate that this could identify the progenitor based on the observed neutrino signal. The expected diffuse supernova neutrino flux is also shown to be modified due to these effects. We are thus led to conclude that these results will contribute towards a better understanding of neutrino masses and mixing, as well as supernova astrophysics and cosmology.

Contents

Declaration	iii
Acknowledgements	v
Foreword	vii
1 Introduction	1
1.1 Neutrinos in a nutshell	1
1.2 Neutrinos from core-collapse supernovae	5
1.3 Phenomenology of supernova neutrinos	10
2 Formalism for Dense Neutrinos	15
2.1 General framework	15
2.2 Effects of source geometry	19
2.3 Spherically symmetric and isotropic source	21
3 Nonlinear Neutrino Oscillations	25
3.1 Bloch vector notation	25
3.2 Generalized gyroscope equations	30
3.3 Heavy-Light factorization of dynamics	33
3.4 Three-flavor dynamics	36
3.5 Flavor conversion mechanisms	40
4 Flavor Conversions of Supernova Neutrinos	57
4.1 Reference SN model	57
4.2 Flavor conversions inside a supernova	61

5	Signatures of Nonlinear Supernova Neutrino Oscillations	69
5.1	Determination of mass hierarchy using Earth matter effects	69
5.2	Progenitor dependence of SN neutronization burst signal	75
6	Impact on the Diffuse Supernova Neutrino Background	79
6.1	Diffuse SN neutrino background	79
6.2	Estimation of DSNB flux	80
6.3	Expected event rate at detectors	82
7	Conclusions	85
	Bibliography	91
	Thesis Synopsis	

Chapter 1

Introduction

In this chapter, we outline our present understanding of neutrinos, stellar collapse leading to a supernova (SN), and the nature of associated neutrino emission. We then present a short review of SN neutrino phenomenology.

1.1 Neutrinos in a nutshell

There are three known neutrinos ν_e , ν_μ and ν_τ , produced in association with the corresponding charged leptons e , μ and τ respectively [1]. These are called “flavor eigenstates”, because they are the eigenstates of the weak interactions. These aren’t the same as the “mass eigenstates”, which are by definition the vacuum-propagation eigenstates.

The mass eigenstates ν_1 , ν_2 and ν_3 are related to the flavor eigenstates as

$$\begin{pmatrix} \nu_e \\ \nu_\mu \\ \nu_\tau \end{pmatrix} = U \begin{pmatrix} \nu_1 \\ \nu_2 \\ \nu_3 \end{pmatrix}, \quad (1.1)$$

where U is known as the Pontecorvo-Maki-Nakagawa-Sakata mixing matrix, or simply the leptonic mixing matrix [2, 3]. This matrix is parameterized, following

the Particle Data Group, as [1]

$$U = R_{23}\Gamma_{13}R_{13}\Gamma_{13}^\dagger R_{12}, \quad (1.2)$$

where R_{ij} is a Euler rotation matrix in the plane i - j with an angle θ_{ij} and $\Gamma_{13} = \text{Diag}(1, 1, e^{i\delta})$ encodes the CP violating phase. The antineutrinos are similarly called $\bar{\nu}_e, \bar{\nu}_\mu$ and $\bar{\nu}_\tau$ and related to their mass eigenstates by U^* . It is clear that neutrinos produced as flavor eigenstates will propagate as a linear combination of the mass eigenstates which will acquire non-trivial relative phases if the energy eigenvalues are different. This naturally leads to a non-zero probability of the neutrino being detected in another flavor at a later time. Let's illustrate this idea using two neutrino flavors. We start with a ν_e at time $t = 0$, which is written in terms of the mass eigenstates and the mixing angle θ as

$$|\nu(0)\rangle = \nu_e = \cos\theta|\nu_1\rangle + \sin\theta|\nu_2\rangle. \quad (1.3)$$

If the energy difference of the two mass eigenstates is ΔE , then the state (up to a global phase) at time t is given by

$$|\nu(t)\rangle = \cos\theta|\nu_1\rangle + e^{-i\Delta Et} \sin\theta|\nu_2\rangle. \quad (1.4)$$

Now, the probability of this state to be observed as a ν_e is $|\langle\nu_e|\nu(t)\rangle|^2$, which is called the survival probability P_{ee} of the initial state ν_e . For relativistic neutrinos travelling in vacuum with momentum \mathbf{p} we have

$$\Delta E = \sqrt{|\mathbf{p}|^2 + m_2^2} - \sqrt{|\mathbf{p}|^2 + m_1^2} \approx \frac{\Delta m^2}{2E}, \quad (1.5)$$

where $\Delta m^2 = m_2^2 - m_1^2$ is called the mass-squared difference. One therefore finds

$$P_{ee} = 1 - \sin^2 2\theta \sin^2 \left(\frac{\Delta m^2 t}{4E} \right) \quad (1.6)$$

This sinusoidal dependence of the flavor composition on time (sometimes rewritten using the pathlength $L = ct$) is called ‘‘Neutrino Flavor Oscillations’’ [4].

Neutrinos interact through the usual weak interactions which allow them to scatter off e , p and n in the background matter. For neutrino oscillations, we mainly consider elastic forward scattering which appear through interference with just one power of the coupling G_F [5]. Almost all these contributions are flavor-blind, except the charged scattering processes which mainly affect ν_e , but not ν_μ or ν_τ , because of the absence of μ or τ leptons in matter. The effective potential energy for ν_e due to matter is thus $\sqrt{2}G_F n_e(\mathbf{r})$, where $n_e(\mathbf{r})$ is the local electron density of the medium. For the $\bar{\nu}_e$ the potential has a relative minus sign. This extra contribution changes the Hamiltonian, thus changing both the effective θ and Δm^2 . The matter density can satisfy the condition

$$\Delta m^2/(2E) = \pm\sqrt{2}G_F n_e(\mathbf{r}) \quad (1.7)$$

and the energy eigenvalues can become effectively degenerate for either neutrinos or antineutrinos, depending on the sign of Δm^2 . This makes the effective mixing angle approximately $\pi/4$ causing large amplitude flavor conversions. This is called a Mikheyev-Smirnov-Wolfenstein (MSW) resonance [5, 6]. This resonance is said to be adiabatic if $n_e(\mathbf{r})$ does not vary too fast along the neutrino trajectory at the resonance, i.e

$$\gamma = \frac{\Delta m^2 \sin^2 2\theta}{2E \cos 2\theta} \left(\frac{1}{n_e(\mathbf{r})} \frac{dn_e(\mathbf{r})}{dr} \right)_{res}^{-1} \gg 1. \quad (1.8)$$

If $\gamma < 1$ at the resonance then the resonance is said to be nonadiabatic. The Landau-Zener level-crossing probability at the resonance, which measures the chance of one instantaneous mass eigenstate converting to another due to the non-adiabaticity, is given by [7, 8]

$$P_{res} = e^{-\pi\gamma/2}. \quad (1.9)$$

A similar potential $\sqrt{2}G_F n_{\nu,\bar{\nu}}(\mathbf{r})$ is also generated due to neutrinos and antineutrinos in the background, as was first pointed out by Pantaleone [9, 10]. While it is negligible in most circumstances, it plays a crucial role for SN neutrinos, and its effects are the main subject of this thesis. We shall therefore discuss this issue in detail later.

The above understanding of neutrino oscillations and experiments using atmospheric, solar and man-made reactor and accelerator neutrinos, allow us to measure the relevant mass and mixing parameters (See e.g. the update as of 2008 in [11]). The data is now described satisfactorily in the three-neutrino oscillation framework defined by two mass squared differences Δm_{\odot}^2 and Δm_{atm}^2 , three mixing angles θ_{12} , θ_{23} and θ_{13} , and the CP -violating phase δ . The parameters θ_{23} and $|\Delta m_{\text{atm}}^2|$ are determined by atmospheric neutrino experiments and long baseline experiments to be

$$\sin^2 \theta_{23} = 0.50_{-0.06}^{+0.07}, \quad (1.10)$$

$$|\Delta m_{\text{atm}}^2| = 2.40_{-0.11}^{+0.12} \times 10^{-3} \text{eV}^2, \quad (1.11)$$

the errors being specified at 1σ . The parameters Δm_{\odot}^2 and θ_{12} are determined by solar and reactor experiments to be

$$\sin^2 \theta_{12} = 0.304_{-0.016}^{+0.022}, \quad (1.12)$$

$$\Delta m_{\odot}^2 = 7.65_{-0.20}^{+0.23} \times 10^{-5} \text{eV}^2. \quad (1.13)$$

Current data on neutrino oscillations do not determine the sign of Δm_{atm}^2 . One refers to $\Delta m_{\text{atm}}^2 > 0$ as normal mass hierarchy and $\Delta m_{\text{atm}}^2 < 0$ as inverted mass hierarchy. For θ_{13} we know from reactor experiments

$$\sin^2 \theta_{13} = 0.01_{-0.011}^{+0.016}. \quad (1.14)$$

The phase δ is completely unknown. The smallness of θ_{13} and $\Delta m_{\odot}^2/|\Delta m_{\text{atm}}^2|$ tell us that $\Delta m_{\odot}^2 \approx \Delta m_{12}^2$ and $\Delta m_{\text{atm}}^2 \approx \Delta m_{13}^2 \approx \Delta m_{23}^2$. The absolute neutrino mass is not known, but the sum of neutrino masses is expected to be less than about 1 eV from cosmology [12].

1.2 Neutrinos from core-collapse supernovae¹

A star with a mass more than $(8 - 10) M_{\odot}$, where M_{\odot} denotes the mass of the Sun, becomes a red or a blue super giant in the final states of its life. Such stars usually have an onion like structure, with each successive inner shell producing successively heavier elements via nuclear reactions. The core is mainly made of iron ², because iron is stable and does not undergo fusion. When the mass of the iron core reaches the Chandrasekhar limit ($\approx 1.4 M_{\odot}$), the electron degeneracy pressure is insufficient to counter-balance the inward gravitational force. When nuclear fuel for fusion runs out, then the core starts collapsing in the absence of radiation pressure. As the core collapses to a radius of about 10 km, the density reaches a few times the nuclear density and the core stiffens. The gravitational binding energy is released mainly as neutrinos and antineutrinos of all flavors, which are copiously produced inside the core of the SN. Most of these neutrinos cannot easily escape because the density is very high. They remain trapped due to total internal reflection, inside what can be crudely thought of as a neutrinosphere. The outer material, which is not in acoustic communication with the bouncing core, keeps falling in and the energy density at the boundary of the core and mantle keeps increasing until eventually the stellar matter bounces off the core creating a shock-wave which goes through the star and blasts off the outer envelope. This scenario where the shock-wave is the source of the explosion is known as the “prompt explosion scenario” [15, 16]. However, simulations suggest that the shock-wave loses a lot of its kinetic energy by dissociating the nuclei in the stellar matter, as it propagates outward. As a result, the shock-wave stops after about 100ms and doesn’t robustly cause a successful explosion.

It is therefore conjectured that more energy must be deposited in the shock-wave while it moves outwards, for the explosion to be successful. This can happen if neutrinos diffuse from the neutrinosphere and interact with the dense matter behind the shockwave, and deposit some of their energy. If enough energy is transferred to the shock-wave then the dying shock-wave can be revived and it can cause a

¹We follow closely the discussion in [13].

²Some supernovae have a degenerate Oxygen-Neon-Magnesium core. They typically have a mass of $(8 - 10) M_{\odot}$. [14]

successful explosion by blowing off the envelope of the star. This scenario is known as the “delayed explosion scenario” [17, 18]. The fact that almost 99% of the energy of a SN goes out in neutrinos, makes this scenario quite plausible from energetic grounds.

The explosion is thus essentially a complex hydrodynamic phenomenon that must be described by elaborate numerical modelling. Although we have come a long way since the celebrated review by Bethe [19], the exact mechanism of the explosion is still not pinned down. The older simulations when repeated with refined physics inputs have failed to produce robust explosions. Even the state-of-the-art simulations do not always end in successful explosions, indicating that our understanding of SN explosions may still be incomplete. Ongoing attempts to improve the simulations to produce robust explosions indicate that magnetohydrodynamics or large-scale convection leading to efficient energy transport may be a key ingredient [20]. With ever-increasing computational power, detailed three-dimensional simulations may soon become possible and be able to shed some light on this issue.

For the purpose of neutrino phenomenology, what is relevant is the electron density profile of the SN, which is proportional to the matter density itself. The static profile (ignoring effects of shockwave propagation) is often taken to have a power-law dependence on the radius, i.e. $n_e(\mathbf{r}) \propto 1/r^3$. This agrees well with most simulations, e.g. Fig. 1.1 ($t = 0.1$ sec) taken from [21]. In the presence of the shock-wave it becomes quite complicated, as shown in Fig. 1.1 (at later times). Realistically, even these are to be thought of as gross over-simplifications. The SN density profile is not likely to be spherically symmetric, or even smooth. In fact it is expected from simulations that the region behind the shock-wave could have large fluctuations in density, due to turbulence.

Neutrinos are emitted from a SN in roughly four distinct phases as shown in Fig. 1.2. In the collapse phase (labelled as (1) in Fig. 1.2) when the star is collapsing and the bounce has not taken place, the flux and the average energies are comparatively low [22]. It steeply rises when the shock-wave travels through the neutrinosphere, breaking apart the nuclei. This suddenly releases a flavor-specific burst of ν_e for

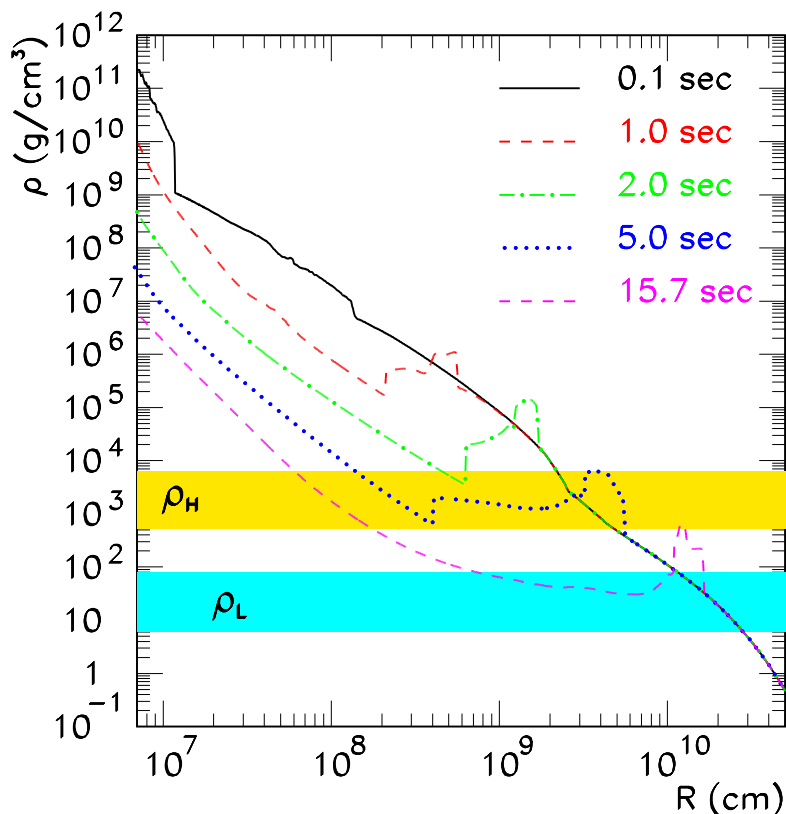


Figure 1.1: SN matter density profiles: In the static limit and including the motion of the shock-wave. The figure has been taken from [21].

about a few milliseconds. This is known as the neutronization burst phase (labelled as (2) in Fig. 1.2). In the accretion phase that follows (labelled as (3) in Fig. 1.2), the mantle cools off by emitting neutrinos for about 1 second, while material is still infalling and accreting. Then the shock-wave travels outwards and the proto-neutron star at the centre cools by radiating away neutrinos for about 10 seconds. This final phase is called the Kelvin-Helmholtz cooling phase (labelled as (4) in Fig. 1.2).

Let us now focus on the neutrinos that are expected from a SN. As the simplest approximation one can assume that the entire binding energy E_b of the star is converted to neutrinos. For a star that explodes and leaves aside a neutron star with radius R and mass M , the released binding energy is $E_b \approx 3G_N M^2/5R$ which is in the ball-park of 10^{53} ergs for a typical SN. If one assumes equipartition of

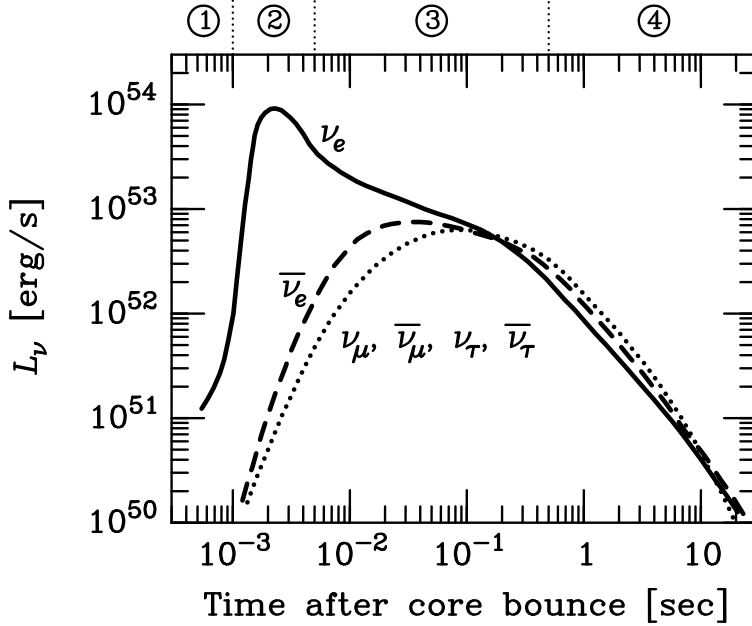


Figure 1.2: Neutrino emission in different stages of SN explosion. The figure has been taken from [13].

energies among ν_e, ν_μ, ν_τ and their antiparticles, the total energy is split six-ways. We know that the neutrinos are emitted from the surface of the neutrinosphere whose radius is about 10 km (roughly the same as the surface of the neutron star). If we apply the virial theorem to estimate the average kinetic energy E_{kin} of the particles escaping from the surface of the neutron star, we have $E_{kin} = G_N M / 2R$ which is about 10 MeV. Thus the number flux of neutrinos is about 10^{57} . These neutrinos are emitted over a duration of order 10 seconds, a timescale that is set by diffusion-time of the neutrinos trapped in the core.

There is a typical flavor dependence of the neutrino spectra. The ν_e and $\bar{\nu}_e$ are produced mainly by electron capture on nuclei. Since there are more neutrons than protons, the $\bar{\nu}_e$ interact less than the ν_e , and thus have slightly higher energies. The ν_μ and ν_τ and the corresponding antiparticles, do not have charged current interactions and thus decouple even before the $\bar{\nu}_e$, and therefore have a larger average energy. It is thus expected that there will be a hierarchy of energies

$$\langle E_{\nu_e} \rangle < \langle E_{\bar{\nu}_e} \rangle < \langle E_{\nu_\mu} \rangle = \langle E_{\nu_\tau} \rangle = \langle E_{\bar{\nu}_\mu} \rangle = \langle E_{\bar{\nu}_\tau} \rangle. \quad (1.15)$$

There is no compelling reason to expect that the binding energy gets exactly equipartitioned, however if approximate equipartitioning does indeed take place, the above hierarchy predicts that the number fluxes have the opposite hierarchy

$$\Phi_{\nu_e} > \Phi_{\bar{\nu}_e} > \Phi_{\nu_\mu} = \Phi_{\nu_\tau} = \Phi_{\bar{\nu}_\mu} = \Phi_{\bar{\nu}_\tau} . \quad (1.16)$$

This is as far as one can argue on general grounds. For more quantitative predictions about neutrino fluxes from a SN one has to appeal to the detailed simulations. The simulations of the Livermore group [23] are again in agreement with these expectations. On the other hand, refined simulations by the Garching group [24] also obtained similar results. Although they did not obtain robust explosions, their simulations employed very detailed neutrino transport and additional interactions that were previously ignored. The neutrino fluxes predicted by the Livermore simulation are shown in Fig. 1.3.

Note that the luminosities are time-dependent, but the average energies do not depend strongly on time. The luminosity is very high in the early stages and decreases slowly with time. Moreover, the relative number fluxes are seen to change. Initially, there more $\bar{\nu}_e$ than ν_μ or ν_τ or the corresponding antiparticles, but this can change at late-times [24]. We will often ignore the time-dependence of the primary spectra in the present analysis for simplicity. In principle, one should include effects of a time dependent spectra and density profile for a more complete treatment.

We could use data from the supernova SN1987A [25, 26], that occurred in the Large Magellanic Cloud about 50 kpc away, to compare with the above estimates for the explosion time-scale and the neutrino spectra. While it put stringent bounds on a variety of things, it did not constrain the simulations strongly owing to low statistics (19 events at two detectors). With present detectors like Super-Kamiokande, a galactic SN could result in up to 10000 events in the first ten seconds of the explosion, which will allow us to learn a lot more about SN neutrino fluxes.

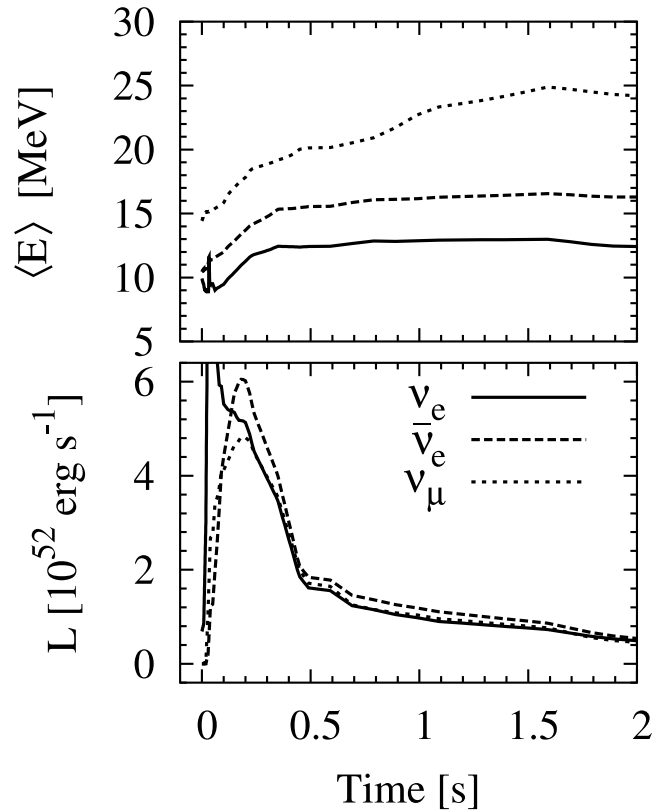


Figure 1.3: Luminosity and average energy of neutrinos as a function of post-bounce time. The figure has been taken from [23].

1.3 Phenomenology of supernova neutrinos

Neutrinos emitted from a core collapse SN carry information about the primary fluxes, neutrino masses and mixing, and SN dynamics. This information gets embedded into the observed neutrino spectra, and needs to be carefully extracted.

In galaxies such as ours, supernovae occur with an estimated rate of about 1 to 3 per century [27]. It is thus expected that a future galactic SN will eventually be observed at existing or planned experiments. This will allow detailed studies of the emitted neutrinos [28]. Detecting neutrinos accumulated in the Universe from all the SN explosions in the past and present epoch form a cosmic background, known as the diffuse supernova neutrino background (DSNB) or supernova relic neutrinos [29, 30], is also a possibility. The expected fluxes [31] are tantalizingly close to detection thresholds at present-day detectors [32].

A detailed interpretation of a neutrino signal from a galactic/extra-galactic SN will depend quite sensitively on our understanding of neutrino flavor conversions. Neutrinos, produced in the region of the neutrinosphere, freestream outwards and pass through the core, mantle and envelope of the star. The drastically different environments in these regions, consisting of varying densities of ordinary matter and neutrinos, affect flavor conversions among neutrinos. The nature of neutrino flavor conversions depends on an interplay of these densities and the natural frequency of a neutrino $\Delta m^2/(2E)$. Close to the neutrinosphere, neutrinos interact with matter and other neutrinos which introduces a matter potential that is $\sqrt{2}G_F n_e(\mathbf{r})$ and a neutrino potential $\sqrt{2}G_F(n_\nu(\mathbf{r}) + n_{\bar{\nu}}(\mathbf{r}))$ respectively. Enhanced conversion can happen in two ways - either due to matter effects, or due to the neutrino potential.

The traditional picture of flavor conversions in a SN is based on the assumption that the effect of neutrino potential is negligible. In this picture, neutrinos that are produced approximately as mass eigenstates at very high ambient matter density in the core propagate outwards from the neutrinosphere. As the matter density becomes smaller, at some \mathbf{r} one encounters the MSW resonances. When the density corresponds to Δm_{atm}^2 , it is called an H resonance that happens at matter densities of about (1000 – 10000) g/cc. When the density corresponds to Δm_{\odot}^2 , it is called an L resonance that happens at matter densities of about (30 – 300) g/cc. The H resonance takes place for neutrinos in the normal hierarchy ($\Delta m_{\text{atm}}^2 > 0$), and for antineutrinos in the inverted hierarchy ($\Delta m_{\text{atm}}^2 < 0$). The L resonance always takes place for neutrinos, since we know $\Delta m_{\odot}^2 > 0$. The conversion efficiency also depends on the gradient of $n_e(\mathbf{r})$ at the MSW resonance, which if large can cause further non-adiabatic flavor conversion. In the static limit of the matter density profile, the H resonance is adiabatic for a large 1 – 3 mixing angle ($\sin^2 \theta_{13} > 10^{-3}$) and non-adiabatic for small mixing angle ($\sin^2 \theta_{13} < 10^{-5}$). When the shock-wave passes through the resonance region, it makes the resonances non-adiabatic temporarily. Multiple shock fronts can give rise to interference effects, and turbulence generated during the explosion may also effectively depolarize the neutrino ensemble giving an “equal” mixture of all flavors.

The outgoing incoherent mixture of vacuum mass eigenstates from the star travels through the interstellar space and is observed at a detector to be a combination of primary fluxes of the three neutrino flavors. This scenario of resonant neutrino conversions in a SN [33] has been studied extensively to probe neutrino mixings and SN dynamics. The work has focussed on the determination of mass hierarchy and signatures of a non-zero θ_{13} [34, 35], matter effects on the neutrino fluxes when they pass through the Earth [36, 37, 38], shock wave effects on observable neutrino spectra and their model independent signatures [21, 39, 40, 41, 42, 43]. Recently, possible interference effects for multiple resonances [44], the role of turbulence in washing out shock wave effects [45, 46, 47], and time variation of the signal [48] have also been explored. Interesting attempts have been also made to investigate if SN and neutrino parameters could be extracted out of potential experimental data [49], and to consider non-standard neutrino interactions [50] or additional neutrino flavors [51].

However, neutrino and antineutrino densities are about 10^{30-35} per cm^3 near the neutrinosphere, which makes the neutrino potential extremely significant. The thing to be noted is that the contribution $\sqrt{2}G_F(n_\nu(\mathbf{r}) + n_{\bar{\nu}}(\mathbf{r}))$ is not flavor diagonal in general; $n_\nu, n_{\bar{\nu}}$ are matrices in flavor space and depend on the flavor composition of the entire neutrino ensemble. Such a dense gas of neutrinos and antineutrinos is coupled to itself, making its evolution nonlinear [9, 10]. A formalism to study flavor evolution of such dense relativistic neutrino gases was developed in [52, 53, 54], where a set of quantum kinetic equations for their evolution were written down. These equations have been studied in detail, though mostly in the two-flavor approximation, and the nature of flavor evolution has been identified [55, 56, 57, 58]. It was eventually understood that a dense gas of neutrinos displays collective flavor conversion, i.e. neutrinos of all energies oscillate together, through synchronized oscillations [59] and/or bipolar oscillations [60, 61]. Another remarkable effect of these interactions is a partial or complete swapping of the energy spectra of two neutrino flavors, called step-wise spectral swapping or simply spectral splits, as the neutrinos transit from a region where nonlinear effects dominate to a region where neutrino density is low [62, 63].

The nonlinear effects in the context of supernovae were considered in [64, 65, 66, 67, 68]. Recent two-flavor simulations showed that the nonlinear effects affect neutrino flavor conversions substantially [69, 70]. Different nonlinear flavor transformations seem to play a part in different regions of the star [71]. Many features of the results of these simulations can be understood from the “single-angle” approximation, i.e. ignoring the dependence of the initial launching angle of neutrinos on the evolutions of neutrino trajectories. Angular dependence of flavor evolution can give rise to additional angle dependent features observed in two-flavor simulations [72, 73], or to decoherence effects [57, 74]. For a realistic asymmetry between neutrino and antineutrino fluxes, such angle dependent effects are likely to be small [75, 76]. Three-flavor effects have been studied in [77, 78, 79, 80, 81]. The dependence on geometry of the neutrinosphere was studied in [82]. It was also shown that nonstandard neutrino interactions can trigger these nonlinear effects for a vanishing mixing angle [83]. A number of studies have concerned themselves with signatures of these nonlinear effects. It is understood that nonlinear oscillations distinguish the normal and inverted mass hierarchies even at extremely small θ_{13} [84, 85]. Nonlinear effects have peculiar manifestations in the neutronization-burst phase of O-Ne-Mg supernovae [79, 80, 86, 87] leading to very specific signatures. Finally, the impact of these nonlinear effects on the DSNB has also been studied [88].

The impact of this nonlinear evolution has also been studied in the context of cosmological neutrino flavor equilibration in the early Universe where the synchronized oscillations play a significant part [89, 90, 91, 92, 93, 94, 95, 96].

Our present work addresses some aspects of this problem that were not considered in previous literature. We investigate effects of the geometry of the emitting source, since it is not apparent that in the absence of spherical symmetry the results would still stay valid. We find however that under an assumption of coherence, flavor evolution can be treated as one-dimensional, similar to sources with spherical symmetry. A major part of our work however, concerns itself with three-flavor effects, i.e. understanding nonlinear flavor conversions in the full three-flavor framework. Two-flavor results are fairly well understood, with the exception of possibly two issues,

viz. decoherence (or lack of it) for asymmetric systems [75], and the existence of the antineutrino spectral split [97]. We show that the two-flavor treatment is valid in most circumstances. However, “decoupling” of the third state is not as obvious as in ordinary neutrino oscillations, and there can be unexpected three-flavor effects. With this formal understanding, we look at flavor conversions in a SN, and attempt to design smoking-gun signatures of these novel effects. One of the striking signatures is related to the presence/absence of Earth matter effects that could allow us to determine the mass hierarchy, even at extremely small θ_{13} , where long baseline oscillation experiments may be ineffective. We also find a SN progenitor dependence of the neutrino signal, which may be interesting for astrophysics. Finally we show that these nonlinear effects can drastically change the expected flux of DSNB neutrinos. We believe that these results will be useful for neutrino physics and SN astrophysics.

Chapter 2

Formalism for Dense Neutrinos

The purpose of this chapter is to present a treatment for the flavor evolution of free-streaming neutrinos emitted from a given source. We show that even for non-spherical sources, the flavor evolution is similar to a spherical source. We then specialize to a spherical source emitting neutrinos isotropically from its surface. The results in this chapter are based on the papers: B. Dasgupta, A. Dighe, A. Mirizzi and G. G. Raffelt, “*Collective neutrino oscillations in non-spherical geometry,*” *Physical Review D* **78** (2008) 033014, [arXiv:0805.3300 [hep-ph]] and B. Dasgupta and A. Dighe, “*Collective three-flavor oscillations of supernova neutrinos,*” *Physical Review D* **77**, 113002 (2008), [arXiv:0712.3798 [hep-ph]].

2.1 General framework

Our framework for SN neutrinos is constructed in a modified flavor basis (ν_e, ν_x, ν_y) defined such that

$$(\nu_e \ \nu_x \ \nu_y)^T = R_{23}^\dagger(\theta_{23})(\nu_e \ \nu_\mu \ \nu_\tau)^T, \quad (2.1)$$

where R_{23}^\dagger is the rotation matrix with an argument θ_{23} that explicitly removes the dependence on the mixing angle θ_{23} ¹. We denote a neutrino of momentum \mathbf{p} at

¹This basis has also been denoted in the literature as $(\nu_e, \nu_{\mu'}, \nu_{\tau'})$ [34]. This is motivated by the observation that we observe ν_e and $\bar{\nu}_e$ at our detectors, whose survival probability is independent of θ_{23} if the initial fluxes are identical in the μ and τ flavors.

time t at position \mathbf{r} by $\nu(\mathbf{p}, \mathbf{r}, t)$. The density matrix for $n_\nu(\mathbf{p}, \mathbf{r}, t)$ neutrinos with momenta between \mathbf{p} and $\mathbf{p} + d\mathbf{p}$ at any position between \mathbf{r} and $\mathbf{r} + d\mathbf{r}$ may be written as

$$\rho_{\nu_\alpha \nu_\beta}(\mathbf{p}, \mathbf{r}, t) \equiv \frac{1}{n_\nu(\mathbf{p}, \mathbf{r}, t)} \sum |\nu(\mathbf{p}, \mathbf{r}, t)\rangle \langle \nu(\mathbf{p}, \mathbf{r}, t)|_{\alpha\beta}, \quad (2.2)$$

where $\alpha, \beta = e, x, y$ are the flavor indices, and the summation is over all $n_\nu(\mathbf{p}, \mathbf{r}, t)$ neutrinos. Note that the density matrix is normalized to have unit trace, but the neutrino density itself is $n_\nu(\mathbf{p}, \mathbf{r}, t)$, which typically falls off as $1/r^2$ from the source. The number density of neutrinos with flavor α is obtained through

$$n_{\nu_\alpha}(\mathbf{p}, \mathbf{r}, t) = n_\nu(\mathbf{p}, \mathbf{r}, t) \rho_{\nu_\alpha \nu_\alpha}(\mathbf{p}, \mathbf{r}, t). \quad (2.3)$$

If $a_{\nu_\alpha}^\dagger$ and a_{ν_α} are the creation and annihilation operators of a neutrino in the flavor eigenstate ν_α we have $\rho_{\nu_\alpha \nu_\beta}(\mathbf{p}) \propto \langle a_{\nu_\beta}^\dagger a_{\nu_\alpha} \rangle$ so that the diagonal entries $\rho_{\nu_\alpha \nu_\alpha}(\mathbf{p}, \mathbf{r}, t)$ are the usual occupation numbers (expectation values of number operators), whereas the off-diagonal elements encode the phase relations that allow one to follow flavor oscillations. Such a description assumes that higher-order correlations beyond field bilinears play no role, probably a good approximation for neutrinos produced from essentially thermal sources such as the early-universe plasma or a SN core.

Antineutrinos are described in an analogous way by $\bar{\rho}_{\nu_\alpha \nu_\beta}(\mathbf{p}, \mathbf{r}, t) = \langle \bar{a}_{\nu_\alpha}^\dagger \bar{a}_{\nu_\beta} \rangle$. Note that we always use overbars to characterize antiparticle quantities. The order of flavor indices was deliberately interchanged on the r.h.s. so that the matrices $\rho(\mathbf{p}, \mathbf{r}, t)$ and $\bar{\rho}(\mathbf{p}, \mathbf{r}, t)$ have identical equations of motion [53].

The effective Hamiltonian in the modified flavor basis for neutrinos $\nu(\mathbf{p}, \mathbf{r}, t)$ of energy $E \approx p = |\mathbf{p}|$ in vacuum is

$$H_{vac}(p) = UM^2U^\dagger/2p, \quad (2.4)$$

where the masses and the mixing matrix are parameterized as

$$M \equiv \text{Diag}(m_1, m_2, m_3), \quad (2.5)$$

$$U \equiv R_{23}^\dagger(\theta_{23})R_{23}(\theta_{23})R_{13}(\theta_{13})R_{12}(\theta_{12}), \quad (2.6)$$

with R_{ij} being the rotation matrices in the i - j plane. In this work, we take the value of the CP -violating phase in neutrino sector to be zero. Now $H_{vac}(p)$ may be explicitly written as

$$H_{vac}(p) = \frac{\Delta m_{13}^2}{2p} \begin{pmatrix} s_{13}^2 & 0 & c_{13}s_{13} \\ 0 & 0 & 0 \\ c_{13}s_{13} & 0 & c_{13}^2 \end{pmatrix} + \frac{\Delta m_{12}^2}{2p} \begin{pmatrix} c_{13}^2 s_{12}^2 & c_{12}c_{13}s_{12} & -c_{13}s_{12}^2 s_{13} \\ c_{12}c_{13}s_{12} & c_{12}^2 & -c_{12}s_{12}s_{13} \\ -c_{13}s_{12}^2 s_{13} & -c_{12}s_{12}s_{13} & s_{12}^2 s_{13}^2 \end{pmatrix}, \quad (2.7)$$

where $\Delta m_{ij}^2 = m_j^2 - m_i^2$ and other symbols have their usual meanings. In matter, neutrinos feel the MSW potential due to charged leptons ²

$$V(\mathbf{r}, t) = \sqrt{2}G_F n_{e^-}(\mathbf{r}, t) \text{Diag}(1, 0, 0) \quad (2.8)$$

that adds to the Hamiltonian, where $n_{e^-}(\mathbf{r})$ is the net electron number density at \mathbf{r} . The effective Hamiltonian also includes the effects of neutrino-neutrino interactions, which to the leading order in G_F depend only on forward scattering and contribute [52, 53, 54]

$$H_{\nu\nu}(\mathbf{p}, \mathbf{r}, t) = \sqrt{2}G_F \int d\mathbf{q} \kappa_{\mathbf{p}\mathbf{q}} \left(n_\nu(\mathbf{q}, \mathbf{r}, t) \rho(\mathbf{q}, \mathbf{r}, t) - \bar{n}_\nu(\mathbf{q}, \mathbf{r}, t) \bar{\rho}(\mathbf{q}, \mathbf{r}, t) \right), \quad (2.9)$$

where $d\mathbf{q}$ is short-hand for $d^3\mathbf{q}/(2\pi^3)$. The interaction strength is dependent on the angular separation of the momenta of the interacting particles, and is given by

²We assume that the density of e^+ , μ^\pm and τ^\pm is negligible, and that ν_μ and ν_τ feel approximately identical potentials, which have been taken to be zero by convention. An analysis of nonlinear effects including a $\mu - \tau$ potential has recently been carried out [77].

$\kappa_{\mathbf{p}\mathbf{q}} \equiv 1 - \cos \theta_{\mathbf{p}\mathbf{q}}$, where $\theta_{\mathbf{p}\mathbf{q}}$ is the angle between \mathbf{p} and \mathbf{q} . Writing the velocity $\mathbf{v}(\mathbf{p}, \mathbf{r}, t) = d\mathbf{r}/dt$, we express $\cos \theta_{\mathbf{p}\mathbf{q}}$ as $\mathbf{v}(\mathbf{p}, \mathbf{r}, t) \cdot \mathbf{v}(\mathbf{q}, \mathbf{r}, t)$.

The equation of motion for the density matrix is

$$\frac{d}{dt}\rho(\mathbf{p}, \mathbf{r}, t) = -i \left[H(\mathbf{p}, \mathbf{r}, t), \rho(\mathbf{p}, \mathbf{r}, t) \right] + \frac{\partial}{\partial t}\rho(\mathbf{p}, \mathbf{r}, t). \quad (2.10)$$

In the steady state (no explicit time dependence in the Hamiltonian and initial conditions) we can drop the time dependence in the problem. The total derivative with time can be expanded then simply as partial derivatives w.r.t \mathbf{p} and \mathbf{r} . Ignoring external forces (terms depending on $d\mathbf{p}/dt$) we have the equations of motion for $\rho(\mathbf{p}, \mathbf{r})$ and $\bar{\rho}(\mathbf{p}, \mathbf{r})$ as [98]

$$\mathbf{v}(\mathbf{p}, \mathbf{r}) \cdot \partial_{\mathbf{r}}\rho(\mathbf{p}, \mathbf{r}) = -i \left[+ H_{vac}(p) + V(\mathbf{r}) + H_{\nu\nu}(\mathbf{p}, \mathbf{r}), \rho(\mathbf{p}, \mathbf{r}) \right], \quad (2.11)$$

$$\mathbf{v}(\mathbf{p}, \mathbf{r}) \cdot \partial_{\mathbf{r}}\bar{\rho}(\mathbf{p}, \mathbf{r}) = -i \left[- H_{vac}(p) + V(\mathbf{r}) + H_{\nu\nu}(\mathbf{p}, \mathbf{r}), \bar{\rho}(\mathbf{p}, \mathbf{r}) \right]. \quad (2.12)$$

The effect of ordinary matter can be “rotated away” by working in the interaction picture [70, 72]. We employ an operator $O(\mathbf{r})$ under which a matrix A transforms to

$$A^{int}(\mathbf{r}) = O(\mathbf{r})AO^{-1}(\mathbf{r}), \quad (2.13)$$

where

$$O(\mathbf{r}) = \exp \left(i \int_0^{\mathbf{r}} d\mathbf{r}' V(\mathbf{r}') \right). \quad (2.14)$$

This choice simplifies the equations of motion by removing the matter term, giving us

$$\mathbf{v}(\mathbf{p}, \mathbf{r}) \cdot \partial_{\mathbf{r}}\rho^{int}(\mathbf{p}, \mathbf{r}) = -i \left[+ H_{vac}^{int}(p, \mathbf{r}) + H_{\nu\nu}^{int}(\mathbf{p}, \mathbf{r}), \rho^{int}(\mathbf{p}, \mathbf{r}) \right], \quad (2.15)$$

$$\mathbf{v}(\mathbf{p}, \mathbf{r}) \cdot \partial_{\mathbf{r}}\bar{\rho}^{int}(\mathbf{p}, \mathbf{r}) = -i \left[- H_{vac}^{int}(p, \mathbf{r}) + H_{\nu\nu}^{int}(\mathbf{p}, \mathbf{r}), \bar{\rho}^{int}(\mathbf{p}, \mathbf{r}) \right]. \quad (2.16)$$

The transformation by $O(\mathbf{r})$ leaves diagonal entries of $\rho(\mathbf{p}, \mathbf{r})$, $\bar{\rho}(\mathbf{p}, \mathbf{r})$, $H_{vac}(p)$ and $H_{\nu\nu}(\mathbf{p}, \mathbf{r})$ unchanged, but the off-diagonal entries become \mathbf{r} -dependent. For example, if $V(\mathbf{r})$ varies adiabatically and only in the radial direction, the vacuum Hamiltonian

changes according to Eq. (2.13) as

$$H_{vac}^{int}(p, r) = H_{vac}(p) + ir \left[V(r), H_{vac}(p) \right] + \frac{(ir)^2}{2!} \left[V(r), \left[V(r), H_{vac}(p) \right] \right] + \dots \quad (2.17)$$

We know that $V(r)$ is a diagonal matrix, so only the off-diagonal elements of $H_0(p)$ are affected by the transformation. The final observables we are going to be interested in, the number fluxes of neutrino flavors, involve only diagonal elements of the density matrix [see Eq. (2.3)], so the interaction basis is well suited for our purposes.

2.2 Effects of source geometry

The nonlinear equations of motion Eq. (2.11) simplify considerably if self-maintained coherence occurs in a dense neutrino gas and all modes can be assumed to evolve in the same way. For this section we restrict ourselves to a source radiating only neutrinos and with no matter background, although an analogous argument may be easily constructed in the general case.

Our demand of self-maintained coherence is defined by

$$\rho(\mathbf{p}, \mathbf{r}) = P(\mathbf{r}) f(\mathbf{p}, \mathbf{r}). \quad (2.18)$$

Here, $f(\mathbf{p}, \mathbf{r}) = \text{Tr}(\rho(\mathbf{p}, \mathbf{r}))$ is a scalar occupation number density, summed over all flavors, while for N flavors $P(\mathbf{r})$ is a $N \times N$ matrix normalized as $\text{Tr}(P(\mathbf{r})) = 1$, which contains the flavor information. We define

$$\langle \mathbf{v}(\mathbf{r}) \rangle \equiv \frac{\int d\mathbf{p} \mathbf{v}(\mathbf{p}, \mathbf{r}) f(\mathbf{p}, \mathbf{r})}{\int d\mathbf{p} f(\mathbf{p}, \mathbf{r})} \quad (2.19)$$

as the momentum average of $\mathbf{v}(\mathbf{p}, \mathbf{r})$ at location \mathbf{r} with respect to the distribution function $f(\mathbf{p}, \mathbf{r})$. The angle-brackets will mean suitable momentum averages as above. Now, we find the equations of motion for $P(\mathbf{r})$ by averaging Eq. (2.11) over

all momenta to get

$$\frac{\mathbf{v}(\mathbf{r})}{|\mathbf{v}(\mathbf{r})|} \cdot \partial_{\mathbf{r}} P(\mathbf{r}) = -i [H^{coh}(\mathbf{r}), P(\mathbf{r})], \quad (2.20)$$

where

$$H^{coh}(\mathbf{r}) = \frac{UM^2U^\dagger}{2} \frac{\int d\mathbf{p} p^{-1} f(\mathbf{p}, \mathbf{r})}{|\int d\mathbf{p} \mathbf{v}(\mathbf{p}) f(\mathbf{p}, \mathbf{r})|} = \frac{UM^2U^\dagger}{2} \frac{\langle p^{-1} \rangle}{|\langle \mathbf{v}(\mathbf{r}) \rangle|}. \quad (2.21)$$

Eq. (2.20) is the equation of motion in the coherent approximation, with $H^{coh}(\mathbf{r})$ as the synchronized matrix of oscillation frequencies. The nonlinear terms vanish since the relevant commutator vanishes on integrating over all momenta. Eq. (2.20) is a partial differential equation for the matrix $P_{\mathbf{r}}$. It can be reduced to a set of ordinary differential equations

$$\frac{d\mathbf{r}}{ds} = \frac{\mathbf{v}(\mathbf{r})}{|\mathbf{v}(\mathbf{r})|}, \quad (2.22)$$

$$\frac{dP(\mathbf{r})}{ds} = -i [H^{coh}(\mathbf{r}), P(\mathbf{r})], \quad (2.23)$$

where s is a parameter along the “characteristic line,” or “streamline,” defined by Eq. (2.22). Since $\langle \mathbf{v}(\mathbf{r}) \rangle$ is unique at each location, the streamlines do not intersect each other. Along each streamline, the differential equation Eq. (2.23), for the matrix $P(\mathbf{r})$ is a set of linear coupled ordinary differential equations which can be solved easily and uniquely, given the boundary conditions. This is true for arbitrary source geometries, and one only needs to calculate $\langle \mathbf{v}(\mathbf{r}) \rangle$ relevant to the problem.

Now, calculating $\langle \mathbf{v}(\mathbf{r}) \rangle$ is a purely geometrical problem. One merely needs to find the average velocity vector at each point in space, for a given convex source. For a spherical source of radius r_0 , we find

$$\langle \mathbf{v}(\mathbf{r}) \rangle = \frac{1}{2} \left[1 + \sqrt{1 - \frac{r_0^2}{r}} \right] \hat{r}. \quad (2.24)$$

which tends to \hat{r} for $r \gg r_0$. This tells us that for spherically symmetric problems the evolution is radial, i.e. the streamlines are radial and the dependence on $\langle \mathbf{v}(\mathbf{r}) \rangle$ can be safely ignored at large r . For non-spherical sources one chooses a coordinate system such that $\langle \mathbf{v}(\mathbf{r}) \rangle$ is always along one of the axes.

2.3 Spherically symmetric and isotropic source

The interaction term $H_{\nu\nu}$ in Eq. (2.9) depends on $\theta_{\mathbf{p}\mathbf{q}}$, i.e. the angle between the momenta of interacting neutrinos. Thus while performing the angular integrals therein, the dependence of the neutrino flux on all angular variables must be taken into account. This makes the problem quite complicated, and an approximate treatment is needed in order to gain useful insights. Two levels of approximation have been considered in literature, *viz.* multi-angle and single-angle. In the multi-angle approximation, azimuthal symmetry about the axis defined by the source and observer is usually assumed, but not complete spherical symmetry. This essentially captures the effects of correlations between trajectories with different initial launching angles. The effects of such correlations can have interesting consequences which have been explored in detail [72, 73, 75, 76]. In the single-angle approximation, it is assumed that the flavor evolution does not significantly depend on any of the angular coordinates (i.e. the evolution is spherically symmetric), and thus we can integrate over all angular degrees of freedom trivially. One must then choose a representative value for $\cos\theta_{\mathbf{p}}$, which we take to be $1/2$.

We assume half-isotropic emission from a source of radius r_0 , as defined in [75], and write

$$n_{\nu}(\mathbf{p}, \mathbf{r}) = n_{\nu}(p, r) = n_{\nu}(p, r_0) r_0^2/r^2, \quad (2.25)$$

$$\rho(\mathbf{p}, \mathbf{r}) = \rho(p, r). \quad (2.26)$$

In the steady state, the fluxes of neutrinos and antineutrinos can be written as

$$\Phi_{\nu} = \int dp 2\pi p^2 4\pi r_0^2 n_{\nu}(p, r_0), \quad (2.27)$$

$$\Phi_{\bar{\nu}} = \int dp 2\pi p^2 4\pi r_0^2 \bar{n}_{\nu}(p, r_0), \quad (2.28)$$

the total flux being $\Phi = \Phi_{\nu} + \Phi_{\bar{\nu}}$.

A further ‘‘unification’’ in the notation for neutrinos and antineutrinos is possible by noting that their equations of motion, i.e. Eqs. (2.11) and (2.12), differ only in

the sign of $H_{vac}(p)$. This suggests a change of variables from p to

$$\omega = |\Delta m_{13}^2|/(2p) . \quad (2.29)$$

Using the same convention as [62], we define for neutrinos

$$n_\nu(\omega, r) \equiv n_\nu(p(\omega), r) , \quad \rho(\omega, r) \equiv \rho(p(\omega), r) , \quad (2.30)$$

and for antineutrinos

$$n_\nu(-\omega, r) \equiv \bar{n}_\nu(p(\omega), r) , \quad \rho(-\omega, r) \equiv \bar{\rho}(p(\omega), r) . \quad (2.31)$$

The negative values of ω thus correspond to antineutrinos. Then we need to solve only for $\rho(\omega, r)$, albeit at the cost of extending the domain of ω to both positive and negative values.

With this reparametrization the vacuum Hamiltonian $H_{vac}(p)$ is now written as $H_{vac}(\omega, h)$, where

$$h = \frac{\Delta m_{13}^2}{|\Delta m_{13}^2|} = \pm 1 \quad (2.32)$$

encoding normal or inverted mass hierarchy. The $H_{\nu\nu}(\mathbf{p}, \mathbf{r})$ term in Eq. (2.9) simplifies to ³

$$H_{\nu\nu}(r) = \mu(r) \int_{-\infty}^{\infty} d\omega f(\omega) \rho(\omega, r) \text{sgn}(\omega) . \quad (2.33)$$

in terms of the distribution function

$$f(\omega) = \frac{1}{\Phi} \frac{|\Delta m_{13}^2|^3 \pi^2 r_0^2}{\omega^4} n_\nu(\omega, r_0) , \quad (2.34)$$

normalized as $\int_{-\infty}^{\infty} d\omega f(\omega) = 1$, and the neutrino potential

$$\mu(r) = \mu_0 g(r) . \quad (2.35)$$

³ Note that $H_{\nu\nu}(\mathbf{p}, \mathbf{r})$ depended on \mathbf{p} only through the direction of \mathbf{p} . This dependence no longer survives in the single-angle approximation.

Here μ_0 is the neutrino potential at the neutrinosphere:

$$\mu_0 \equiv \mu(r_0) = \frac{3\sqrt{2}G_F\Phi}{128\pi^4 r_0^2}, \quad (2.36)$$

and the “geometric dilution factor” $g(r)$ is given by

$$\begin{aligned} g(r) &\equiv \frac{4r_0^2}{3r^2} \int_{\sqrt{1-(r_0/r)^2}}^1 d(\cos\theta_{\mathbf{q}}) (1 - \cos\theta_{\mathbf{q}} \cos\theta_{\mathbf{p}}) \Big|_{\cos\theta_{\mathbf{p}}=1/2} \\ &= \frac{4r_0^2}{3r^2} \left(1 - \sqrt{1 - \frac{r_0^2}{r^2} - \frac{r_0^2}{4r^2}} \right). \end{aligned} \quad (2.37)$$

The geometric dilution factor equals unity for $r = r_0$, whereas at large r_0 , it decreases as $1/r^4$. The decrease of neutrino densities from a finite source accounts for a factor of $1/r^2$, whereas the additional dilution factor of approximately $1/r^2$ arises from the integral in Eq. (2.37), due to the decreasing angle subtended by the source and reduced collinearity, which are encoded in the limits and the integrand respectively [69]. Note that the exact numerical factors depend on the choice of $\cos\theta_{\mathbf{p}}$.

The total flux Φ remains conserved as long as there is no explicit temporal variation of the overall luminosity. We work in the steady state approximation and assume the luminosity to be constant in time. Slow variations in it may be taken into account by including an additional time dependent factor. Note that $f(\omega)$ is independent of r , which embodies the fact that the normalized neutrino spectrum does not change. Using Eq. (2.3), we can also write the flavor dependent ω -spectra $f_{\nu_\alpha}(\omega, r)$ as

$$f_{\nu_\alpha}(\omega, r) = f(\omega)\rho_{\nu_\alpha\nu_\alpha}(\omega, r). \quad (2.38)$$

Note that $f_{\nu_e}(\omega, r)$ contains the spectra of both ν_e and $\bar{\nu}_e$, and depends on r only through $\rho_{\nu_e\nu_e}(\omega, r)$. It would be a constant on the trajectory if there were no flavor evolution of $\rho_{\nu_e\nu_e}(\omega, r)$. For later use, we define the energy integrated neutrino fluxes

for each flavor as

$$\Phi_{\nu_e}(r) = \Phi \int_0^\infty d\omega f_{\nu_e}(\omega, r) , \quad (2.39)$$

$$\Phi_\nu = \Phi_{\nu_e}(r) + \Phi_{\nu_x}(r) + \Phi_{\nu_y}(r) , \quad (2.40)$$

$$\Phi_{\bar{\nu}_e}(r) = \Phi \int_{-\infty}^0 d\omega f_{\nu_e}(\omega, r) , \quad (2.41)$$

$$\Phi_{\bar{\nu}} = \Phi_{\bar{\nu}_e}(r) + \Phi_{\bar{\nu}_x}(r) + \Phi_{\bar{\nu}_y}(r) . \quad (2.42)$$

With these approximations, the problem is reduced to an ordinary one dimensional problem along the radial direction. We can also drop the dependence on $\langle \mathbf{v}(\mathbf{r}) \rangle$ because it is significantly different from 1, only very close to the source. We denote the derivative with respect to r using a “dot”, and using Eqs. (2.11) and (2.12), arrive at the single-angle equations of motion

$$\dot{\rho}(\omega, r) = -i \left[+ H_{vac}(\omega, h) + V(r) + H_{\nu\nu}(r), \rho(\omega, r) \right] . \quad (2.43)$$

We have thus used the spherical symmetry of the problem, and the simple energy dependence, to rephrase the equations of motion in a somewhat simpler form. This single-angle approximation is probably crude, but it has been shown in numerical simulations (for two flavors) that this approximation seems to work reasonably well [76]. It also seems that the multi-angle effects are suppressed when the neutrino and antineutrino spectra are not identical [75]. We assume the above results to hold true for three flavors as well, and ignore multi-angle effects in this work. Thus, for an analytical understanding of various flavor conversion phenomena associated with this system, we confine our discussion to the steady-state single-angle half-isotropic approximation that we have outlined above.

Chapter 3

Nonlinear Neutrino Oscillations

In this chapter we rewrite the equations for flavor evolution, which end up resembling those of a classical spinning top (or more precisely a gyroscope). This allows us to recover results already known for two-flavors, and to investigate the effect of three-flavor mixing. We solve the equations of motion and end the chapter with a classification of the various linear and nonlinear flavor conversion mechanisms. The results in this chapter are based on the papers: B. Dasgupta and A. Dighe, “*Collective three-flavor oscillations of supernova neutrinos*,” *Physical Review D* **77**, 113002 (2008), [arXiv:0712.3798 [hep-ph]] and B. Dasgupta, A. Dighe, A. Mirizzi and G. G. Raffelt, “*Spectral split in prompt supernova neutrino burst: Analytic three-flavor treatment*,” *Physical Review D* **77** (2008) 113007, [arXiv:0801.1660 [hep-ph]].

3.1 Bloch vector notation

We have a bunch of equations involving 3×3 matrices. But all components of these matrices are not independent. These matrices are all hermitian, and it is better to get rid of the redundant degrees of freedom. It is thus useful to re-express the density matrices and the Hamiltonian as Bloch vectors. The idea, analogous to the two-flavor case, is to express the matrices in a basis of hermitian matrices, and to study the motion of the vectors constructed out of the expansion coefficients (which are called the Bloch vectors). In our problem, we choose the basis consisting of the

3×3 identity matrix I , and the 8 Gell-Mann matrices Λ_a given by

$$\begin{aligned}
 \Lambda_1 &= \begin{bmatrix} 0 & 1 & 0 \\ 1 & 0 & 0 \\ 0 & 0 & 0 \end{bmatrix}, \quad \Lambda_2 = \begin{bmatrix} 0 & -i & 0 \\ i & 0 & 0 \\ 0 & 0 & 0 \end{bmatrix}, \quad \Lambda_3 = \begin{bmatrix} 1 & 0 & 0 \\ 0 & -1 & 0 \\ 0 & 0 & 0 \end{bmatrix}, \\
 \Lambda_4 &= \begin{bmatrix} 0 & 0 & 1 \\ 0 & 0 & 0 \\ 1 & 0 & 0 \end{bmatrix}, \quad \Lambda_5 = \begin{bmatrix} 0 & 0 & -i \\ 0 & 0 & 0 \\ i & 0 & 0 \end{bmatrix}, \quad \Lambda_6 = \begin{bmatrix} 0 & 0 & 0 \\ 0 & 0 & 1 \\ 0 & 1 & 0 \end{bmatrix}, \\
 \Lambda_7 &= \begin{bmatrix} 0 & 0 & 0 \\ 0 & 0 & -i \\ 0 & i & 0 \end{bmatrix}, \quad \Lambda_8 = \frac{1}{\sqrt{3}} \begin{bmatrix} 1 & 0 & 0 \\ 0 & 1 & 0 \\ 0 & 0 & -2 \end{bmatrix}, \tag{3.1}
 \end{aligned}$$

which satisfy the $SU(3)$ Lie algebra

$$[\Lambda_a, \Lambda_b] = if_{abc} \Lambda_c, \tag{3.2}$$

where a, b, c are integers from 1 to 8. Note that the normalization for the matrices is chosen such that

$$\text{Tr}(\Lambda_a \Lambda_b) = 2\delta_{ab}. \tag{3.3}$$

The structure constants f_{abc} are antisymmetric under exchange of any two indices and are specified by

$$f_{123} = 2; \quad f_{147}, f_{165}, f_{246}, f_{257}, f_{345}, f_{376} = 1; \quad f_{678}, f_{458} = \sqrt{3}. \tag{3.4}$$

Note that basis of traceless matrices Λ_a can be expressed as a semi-direct sum of

$$\mathbb{K} = \{\Lambda_1, \Lambda_2, \Lambda_3, \Lambda_8\} \quad \text{and} \quad \mathbb{Q} = \{\Lambda_4, \Lambda_5, \Lambda_6, \Lambda_7\}, \tag{3.5}$$

i.e. for $K_a \in \mathbb{K}$ and $Q_a \in \mathbb{Q}$ we have

$$[K_a, Q_b] \in \mathbb{K}, \quad [Q_a, Q_b] \in \mathbb{K} \quad \text{and} \quad [Q_a, K_b] \in \mathbb{Q}. \tag{3.6}$$

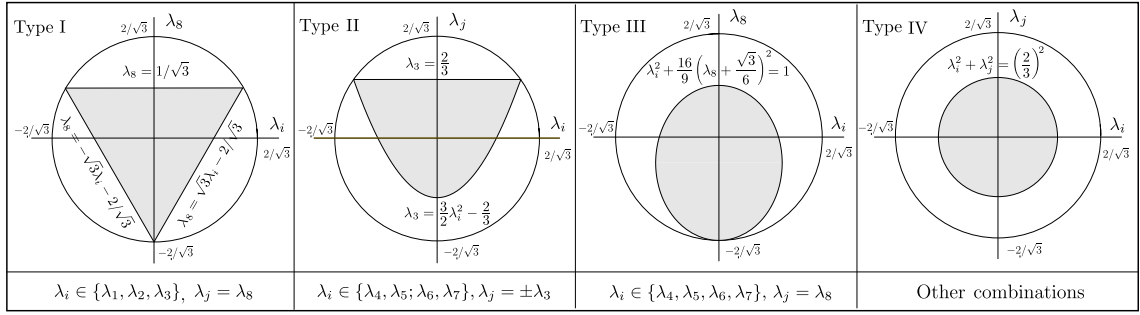


Figure 3.1: The shape of the Bloch-ball for a vector $\lambda_i \hat{e}_i$. The figure has been taken from [99].

In fact this is not the only choice of \mathbb{K} and \mathbb{Q} that has this property. In addition to the decomposition

$$\mathbb{K}^{ex} = \{\Lambda_1, \Lambda_2, \Lambda_3, \Lambda_8\} \quad \text{and} \quad \mathbb{Q}^{ex} = \{\Lambda_4, \Lambda_5, \Lambda_6, \Lambda_7\}, \quad (3.7)$$

as above, we could also choose

$$\mathbb{K}^{ey} = \{\Lambda_3, \Lambda_4, \Lambda_5, \Lambda_8\} \quad \text{and} \quad \mathbb{Q}^{ey} = \{\Lambda_1, \Lambda_2, \Lambda_6, \Lambda_7\} \quad \text{or} \quad (3.8)$$

$$\mathbb{K}^{xy} = \{\Lambda_3, \Lambda_6, \Lambda_7, \Lambda_8\} \quad \text{and} \quad \mathbb{Q}^{xy} = \{\Lambda_1, \Lambda_2, \Lambda_4, \Lambda_5\}, \quad (3.9)$$

which satisfy the conditions in Eq. (3.6). The meaning of the superscripts (ex, ey, xy) on \mathbb{K} and \mathbb{Q} will become clear later.

Using the basis matrices I and Λ_a , we now express any 3×3 hermitian matrix X as a vector \mathbf{X} in the $SU(3)$ generator space (with unit vectors \hat{e}_i) as

$$X = \frac{1}{3} X_0 I + \frac{1}{2} \mathbf{X} \cdot \mathbf{\Lambda}. \quad (3.10)$$

We call \mathbf{X} the Bloch vector corresponding to the matrix X . The vector \mathbf{X} must lie completely within an eight-dimensional compact volume, called the Bloch ball, whose various two-dimensional sections are shown in Fig. 3.1. We say that the vector \mathbf{X} is contained in \mathbb{K}^{ex} ($\mathbb{K}^{ey}, \mathbb{K}^{xy}$) if the matrix X can be expressed solely as a linear combination of $\Lambda_a \in \mathbb{K}^{ex}$ ($\mathbb{K}^{ey}, \mathbb{K}^{xy}$).

We reparameterize our equations using Eq. (3.10), and define the Bloch vectors

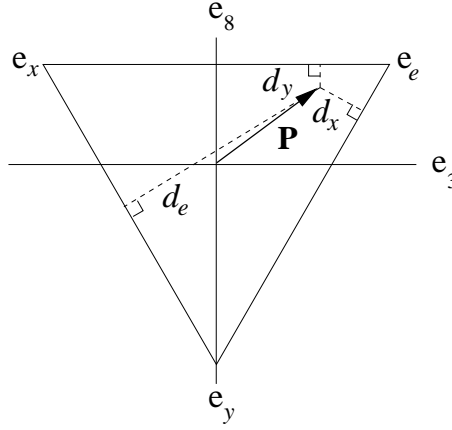


Figure 3.2: The projection of a polarization vector representing a neutrino \mathbf{P} on the \mathbf{e}_3 - \mathbf{e}_8 plane.

corresponding to the density matrices as

$$\rho(\omega, r) = \frac{1}{3} P_0(\omega, r) I + \frac{1}{2} \mathbf{P}(\omega, r) \cdot \mathbf{\Lambda} . \quad (3.11)$$

Note that $\mathbf{\Lambda}$ is an eight-vector of 3×3 matrices. The scalar $P_0(\omega, r)$ and the polarization vector $\mathbf{P}(\omega, r)$ encode the flavor content of neutrinos of energy $p = |\Delta m_{13}^2|/(2\omega)$ at a distance r for $\omega > 0$. The negative values of ω encode the same information for antineutrinos. Since $\rho(\omega, r)$ has been normalized to have unit trace by definition, $P_0(\omega, r)$ is equal to one. We will therefore not worry about the zeroth component of the polarization vector henceforth. For a pure state, $\mathbf{P}(\omega, r)$ lies on the boundary of the shaded region in Fig. 3.1, and has the magnitude $2/\sqrt{3}$. For a mixed state, the magnitude of $\mathbf{P}(\omega, r)$ is smaller and the vector lies within the shaded region.

We assume that all neutrinos are produced as flavor eigenstates, i.e. the primary flux consists of $n_{\nu_\alpha}(p, r_0)$ and $\bar{n}_{\nu_\alpha}(p, r_0)$ with energy p . The initial density matrix $\rho(p, r_0)$ is therefore $\text{Diag}\left(n_{\nu_e}(p, r_0), n_{\nu_x}(p, r_0), n_{\nu_y}(p, r_0)\right)$, and similarly for antineutrinos. The initial polarization vector may be written as

$$\mathbf{P}(\omega, r_0) = \frac{f_{\nu_e}(\omega, r_0) - f_{\nu_x}(\omega, r_0)}{f(\omega)} \hat{\mathbf{e}}_3 + \frac{f_{\nu_e}(\omega) + f_{\nu_x}(\omega) - 2f_{\nu_y}(\omega, r_0)}{\sqrt{3} f(\omega)} \hat{\mathbf{e}}_8 . \quad (3.12)$$

The polarization vector $\mathbf{P}(\omega, r)$, when projected onto the \mathbf{e}_3 - \mathbf{e}_8 plane, must lie within the triangle in Fig. 3.2, where we show a representative $\mathbf{P}(\omega, r)$ projected on the \mathbf{e}_3 - \mathbf{e}_8 plane. The pure electron flavor is represented by

$$\mathbf{e}_e = \hat{\mathbf{e}}_3 + \frac{\hat{\mathbf{e}}_8}{\sqrt{3}}. \quad (3.13)$$

The ν_e or $\bar{\nu}_e$ content with energy p at position r is given by

$$\rho_{\nu_e \nu_e}(p, r) = \frac{n_{\nu_e}(p, r)}{n_\nu(p)} = \frac{f_{\nu_e}(\omega, r)}{f(\omega)} = \frac{1}{3} + \frac{\mathbf{P} \cdot \mathbf{e}_e}{2} = \frac{d_e}{\sqrt{3}}. \quad (3.14)$$

The projection of \mathbf{P} on $\hat{\mathbf{e}}_e$ is thus related to $\rho_{\nu_e \nu_e}(p, r) = f_{\nu_e}(\omega, r)/f(\omega)$ as above. The same quantity can be easily visualized from the figure as $d_e/\sqrt{3}$, where d_e is the distance of the tip of \mathbf{P} from the side of the triangle that is perpendicular to $\hat{\mathbf{e}}_e$ (as shown in the figure). The number of ν_x and ν_y are also similarly calculated. Negative values of ω encode the same information for the antineutrinos. This gives a simple pictorial way to represent the flavor content of the ensemble by plotting the tip of the projection of $\mathbf{P}(\omega, r)$ on the \mathbf{e}_3 - \mathbf{e}_8 plane.¹

For the mass term in the Hamiltonian, we have

$$H_{vac}(\omega, h) = h\omega \left(\frac{1}{3} B_0 I + \frac{1}{2} \mathbf{B} \cdot \mathbf{\Lambda} \right), \quad (3.15)$$

where

$$\begin{aligned} h \mathbf{B} = & \epsilon c_{13} \sin 2\theta_{12} \hat{\mathbf{e}}_1 + \left(s_{13}^2 - \epsilon(c_{12}^2 - c_{13}^2 s_{12}^2) \right) \hat{\mathbf{e}}_3 \\ & + (1 - \epsilon s_{12}^2) \sin 2\theta_{13} \hat{\mathbf{e}}_4 - \epsilon s_{13} \sin 2\theta_{12} \hat{\mathbf{e}}_6 \\ & + \left((-2 + \epsilon)(3c_{13}^2 - 1) + 3\epsilon s_{13}^2(2c_{12}^2 - 1) \right) / (2\sqrt{3}) \hat{\mathbf{e}}_8. \end{aligned} \quad (3.16)$$

Note that ω for neutrinos is always positive in this convention, and the negative sign of Δm_{13}^2 for inverted hierarchy is absorbed into \mathbf{B} . We make use of the the

¹Note that probability conservation in this representation corresponds to the theorem that the sum of the lengths of perpendiculars dropped from any point inside an equilateral triangle to the three sides is a constant.

smallness of the ratio of the two mass square differences, defined as

$$\epsilon = \Delta m_{12}^2 / \Delta m_{13}^2 \quad (3.17)$$

to account for effects that arise from the mixing of the third flavor. The sign of ϵ is positive for normal mass hierarchy ($\Delta m_{13}^2 > 0$), and negative otherwise. This, along with the overall sign due to h , guarantees that the contributions from Δm_{12}^2 always have the same sign. Note that B_2, B_5, B_7 vanish in the absence of CP -violation.

The MSW potential defined in Eq. (2.8) may be represented as

$$V(r) = \lambda(r) \left(\frac{1}{3} L_0 I + \frac{1}{2} \mathbf{L} \cdot \mathbf{\Lambda} \right), \quad (3.18)$$

where $\lambda(r) = \sqrt{2} G_F n_{e^-}(r)$. The vector \mathbf{L} parameterizes the effect of background electrons, and is given by

$$\mathbf{L} = \hat{\mathbf{e}}_3 + \hat{\mathbf{e}}_8 / \sqrt{3}. \quad (3.19)$$

The $H_{\nu\nu}(r)$ term defined in Eq. (2.33) can also be simply written as

$$H_{\nu\nu}(r) = \mu(r) \left(\frac{1}{3} D_0 I + \frac{1}{2} \mathbf{D}(r) \cdot \mathbf{\Lambda} \right), \quad (3.20)$$

where $\mathbf{D}(r)$ is defined as

$$\mathbf{D}(r) = \int d\omega f(\omega) \mathbf{P}(\omega, r) \operatorname{sgn}(\omega). \quad (3.21)$$

In the next section, we shall express the evolution equation, i.e. Eq. (2.43) in terms of the Bloch vectors $\mathbf{P}(\omega, r), \mathbf{B}(\omega, h), \mathbf{L}$ and $\mathbf{D}(r)$.

3.2 Generalized gyroscope equations

We have expressed our problem in terms of the eight-dimensional Bloch vectors, and now we shall see that the equations of motion formally resemble the equations of a gyroscope. To make this apparent, we define \times as a generalized ‘‘cross product’’

[100] with f_{abc} as the structure constants, instead of the usual ϵ_{abc} that appears in the two-flavor approximation, e.g.

$$\mathbf{B} \times \mathbf{P} \equiv \sum_{a,b=1}^8 f_{abc} \mathbf{B}_a \mathbf{P}_b \hat{\mathbf{e}}_c . \quad (3.22)$$

This makes it possible to write the equations of motion, i.e. Eq. (2.43), compactly as

$$\dot{\mathbf{P}}(\omega, r) = \left(\omega \mathbf{B} + \lambda(r) \mathbf{L} + \mu(r) \mathbf{D}(r) \right) \times \mathbf{P}(\omega, r) \equiv \mathbf{H}(\omega, r) \times \mathbf{P}(\omega, r) , \quad (3.23)$$

where $\mathbf{P}(\omega, r)$, \mathbf{B} , \mathbf{L} , $\mathbf{D}(r)$ are defined in Eqs. (3.11), (3.16), (3.19) and (3.21) respectively. The couplings ω , $\mu(r)$ and $\lambda(r)$ are defined in Eqs. (2.29), (2.37) and (3.18) respectively. Equation (3.23) resembles the equation of a spin in an external magnetic field, or equivalently, that of a gyroscope. We must remember that this similarity is purely formal, because unlike in the two-flavor case, we cannot write an arbitrary Bloch vector as a linear combination of two Bloch vectors and their cross product. We shall show in Sec. 3.3 that under certain approximations these generalized gyroscope equations can be given a geometrical interpretation.

The effects of the matter term $\lambda(r) \mathbf{L}$ in Eq. (3.23) can be rotated away by going to the interaction frame as described in Eq. (2.13), where a matrix A becomes $A^{int} = OAO^{-1}$. In order to determine the Bloch vector corresponding to A^{int} , we equate

$$\frac{A_0}{3} I + \sum_{a=1}^8 \frac{A_a \Lambda_a}{2} = OAO^{-1} . \quad (3.24)$$

Multiplying both sides by Λ_a and taking trace, we get

$$A_a^{int} = \text{Tr}(\Lambda_a OAO^{-1}) , \quad (3.25)$$

where we have used $\text{Tr}(\Lambda_a \Lambda_b) = 2\delta_{ab}$. In particular, the Bloch vector \mathbf{B}^{int} may be

written using Eqs. (2.14) and (3.25) as

$$\begin{aligned} \mathbf{B}^{int}(r) = & B_1 \cos \zeta(r) \hat{\mathbf{e}}_1 + B_1 \sin \zeta(r) \hat{\mathbf{e}}_2 + B_3 \hat{\mathbf{e}}_3 \\ & + B_4 \cos \zeta(r) \hat{\mathbf{e}}_4 + B_4 \sin \zeta(r) \hat{\mathbf{e}}_5 + B_6 \hat{\mathbf{e}}_6 + B_7 \hat{\mathbf{e}}_7 + B_8 \hat{\mathbf{e}}_8 , \end{aligned} \quad (3.26)$$

where $\zeta(r) = \int_0^r V(r') dr'$. In dense matter, $B_a^{int}(r)$ oscillates rapidly with the frequency $\sim V(r)$, mimicking a suppression in the relevant mixing angles as in the two-flavor case [60].

We also define the “signed” and “unsigned” n^{th} moments (with $n \geq 0$) of $\mathbf{P}(\omega, r)$ as

$$\mathbf{D}^{(n)}(r) = \int d\omega \omega^n f(\omega) \mathbf{P}(\omega, r) \text{sgn}(\omega) , \quad (3.27)$$

$$\mathbf{S}^{(n)}(r) = \int d\omega \omega^n f(\omega) \mathbf{P}(\omega, r) . \quad (3.28)$$

Note that $\mathbf{D}^{(0)}$ is same as \mathbf{D} , and we will therefore refer to $\mathbf{S}^{(0)}$ as \mathbf{S} . The evolution of these moments are governed by

$$\dot{\mathbf{D}}^{(n)}(r) = \mathbf{B} \times \mathbf{D}^{(n+1)}(r) + \left(\lambda(r)\mathbf{L} + \mu(r)\mathbf{D}(r) \right) \times \mathbf{D}^{(n)}(r) , \quad (3.29)$$

$$\dot{\mathbf{S}}^{(n)}(r) = \mathbf{B} \times \mathbf{S}^{(n+1)}(r) + \left(\lambda(r)\mathbf{L} + \mu(r)\mathbf{D}(r) \right) \times \mathbf{S}^{(n)}(r) . \quad (3.30)$$

We see that the higher moments turn up in equations of motion of the lower moments. If we take the dot product of Eq. (3.29) with $\mathbf{D}^{(n)}(r)$, and of Eq. (3.30) with $\mathbf{S}^{(n)}(r)$, we get

$$\begin{aligned} \partial_r |\mathbf{D}^{(n)}(r)|^2 &= \mathbf{D}^{(n)}(r) \cdot \mathbf{B} \times \mathbf{D}^{(n+1)}(r) , \\ \partial_r |\mathbf{S}^{(n)}(r)|^2 &= \mathbf{S}^{(n)}(r) \cdot \mathbf{B} \times \mathbf{S}^{(n+1)}(r) . \end{aligned} \quad (3.31)$$

The above dependence of the moments on r implies that there is likely to be a redistribution of flavor as a function of ω . It will be interesting to investigate if these moment equations can be used to predict the nature of the redistribution of flavor spectra.

3.3 Heavy-Light factorization of dynamics

The three-flavor dynamics in the traditional matter-driven scenario can be factorized into the so-called “heavy” (H) and “light” (L) MSW resonances that occur at densities corresponding to $\Delta m_{\text{atm}}^2 \approx \Delta m_{13}^2$ and $\Delta m_{\odot}^2 \approx \Delta m_{12}^2$ respectively. Appropriate combination of the effective two-flavor dynamics in these two sectors approximates the three-flavor result reasonably well. We now proceed to illustrate a similar simplification for nonlinear effects as well. Let us first introduce the notion of “heavy” and “light” subspaces of the Bloch-sphere. In the \mathbb{K} - \mathbb{Q} decomposition shown in Eq. (3.8), the vectors contained in \mathbb{K}^{ey} are termed “heavy” (written with superscript H) whereas those contained in \mathbb{Q}^{ey} are termed “light” (written with superscript L). A general vector \mathbf{X} may be decomposed as

$$\mathbf{X} = \mathbf{X}^H + \mathbf{X}^L . \quad (3.32)$$

In particular, \mathbf{B} in Eq. (3.16) may be expressed as $\mathbf{B} = \mathbf{B}^H + \mathbf{B}^L$, with

$$\begin{aligned} h\mathbf{B}^H &= \left(s_{13}^2 - \epsilon(c_{12}^2 - c_{13}^2 s_{12}^2) \right) \hat{\mathbf{e}}_3 + (1 - \epsilon s_{12}^2) \sin 2\theta_{13} \hat{\mathbf{e}}_4 \\ &\quad + \left((-2 + \epsilon)(3c_{13}^2 - 1) + 3\epsilon s_{13}^2(2c_{12}^2 - 1) \right) / (2\sqrt{3}) \hat{\mathbf{e}}_8 , \\ h\mathbf{B}^L &= \epsilon c_{13} \sin 2\theta_{12} \hat{\mathbf{e}}_1 - \epsilon s_{13} \sin 2\theta_{12} \hat{\mathbf{e}}_6 . \end{aligned} \quad (3.33)$$

The component \mathbf{B}^H appears primarily due to Δm_{13}^2 , and the other component \mathbf{B}^L vanishes if $\epsilon = 0$. Note that for two-flavors, or equivalently in the $\epsilon = 0$ limit, \mathbf{B} is completely contained in \mathbb{K}^{ey} . Now, note the following structure in the equations of motion of a polarization vector:

$$\dot{\mathbf{P}}^H(\omega, r) = \mathbf{H}^H(\omega, r) \times \mathbf{P}^H(\omega, r) + \mathbf{H}^L(\omega, r) \times \mathbf{P}^L(\omega, r) , \quad (3.34)$$

$$\dot{\mathbf{P}}^L(\omega, r) = \mathbf{H}^L(\omega, r) \times \mathbf{P}^H(\omega, r) + \mathbf{H}^H(\omega, r) \times \mathbf{P}^L(\omega, r) . \quad (3.35)$$

It is clear from the above set of equations that if $\epsilon = 0$ and one begins with \mathbf{P} contained in \mathbb{K}^{ey} , then \mathbf{P} always remains in \mathbb{K}^{ey} , i.e. $\mathbf{P}^L(\omega, r) = 0$ identically. To

investigate this case closely, we write Eq. (3.34) for each component of \mathbf{P}^H as ²

$$\dot{P}_3 = H_4 P_5 - H_5 P_4, \quad (3.36)$$

$$\dot{P}_4 = H_5 P_3 - H_3 P_5 + \sqrt{3}(H_5 P_8 - H_8 P_5), \quad (3.37)$$

$$\dot{P}_5 = H_3 P_4 - H_4 P_3 + \sqrt{3}(H_8 P_4 - H_4 P_8), \quad (3.38)$$

$$\dot{P}_8 = \sqrt{3}(H_4 P_5 - H_5 P_4). \quad (3.39)$$

Note that $\dot{P}_8 = \sqrt{3} \dot{P}_3$. This suggests that we could rotate our coordinates in the \mathbf{e}_3 - \mathbf{e}_8 plane by $-2\pi/3$, so that \tilde{P}_8 in the rotated frame becomes a constant of motion. While going to the rotated frame, the components X_3 and X_8 of any Bloch vector \mathbf{X} transform as

$$\begin{pmatrix} \tilde{X}_3 \\ \tilde{X}_8 \end{pmatrix} = \begin{pmatrix} -1/2 & -\sqrt{3}/2 \\ \sqrt{3}/2 & -1/2 \end{pmatrix} \begin{pmatrix} X_3 \\ X_8 \end{pmatrix}. \quad (3.40)$$

The other components remain unchanged.

This leads to the following simplified equations of motion for the two-flavor case:

$$\dot{\tilde{P}}_3 = -2(H_4 P_5 - H_5 P_4), \quad (3.41)$$

$$\dot{\tilde{P}}_4 = -2(H_5 \tilde{P}_3 - \tilde{H}_3 P_5), \quad (3.42)$$

$$\dot{\tilde{P}}_5 = -2(\tilde{H}_3 P_4 - H_4 \tilde{P}_3), \quad (3.43)$$

$$\dot{\tilde{P}}_8 = 0. \quad (3.44)$$

This is the two-flavor limit, where the state ν_x does not participate in the evolution. This is a consequence of all the polarization vectors initially being contained in \mathbb{K}^{ey} . The rotated “tilde” frame can therefore be called as the “ $e - y$ ” frame.

The Eqs. (3.41), (3.42) and (3.43) can be simply written as

$$\dot{\mathbf{P}}^{ey} = \mathbf{H}^{ey} \times \mathbf{P}^{ey}, \quad (3.45)$$

where the “ \times ” can now be taken to be the usual cross product in a three-dimensional

²In the following sections, the dependence of the Bloch vectors and the parameters on ω and r is implicit.

space spanned by $\{\mathbf{e}_3^{e_y}, \mathbf{e}_4, \mathbf{e}_5\}$. This clearly exhibits the “gyration” of \mathbf{P} about \mathbf{H} , while the component of \mathbf{P} along $\mathbf{e}_8^{e_y}$ remains constant. The projection of \mathbf{P} changes only along $\mathbf{e}_3^{e_y}$, which corresponds to $\nu_e \leftrightarrow \nu_y$ flavor conversions. The problem is thus reduced to the two-flavor limit, for which analytical solutions have been discussed in literature [59, 60, 61, 62, 63].

In the two-flavor limit, it is observed that there are three qualitatively different kinds of motion of the polarization vector in the flavor space. The most familiar case is oscillations in vacuum/matter, where the neutrino-antineutrino density is small ($\mu \ll \omega$) and each $\mathbf{P}(\omega)$ precesses about \mathbf{B} with frequency ω . The other extreme is when the neutrino-antineutrino density is very large ($\mu \gg \omega$). In such a situation, all $\mathbf{P}(\omega)$ remain tightly bound together and precess with the average ω of the ensemble, giving rise to synchronized oscillations. The intermediate regime ($\mu \gtrsim \omega$) is when the $\mathbf{P}(\omega)$ remain bound together to a large extent, but have a tendency to relax to the state that has the lowest energy. The system is analogous to a pendulum/gyroscope that tries to relax to its vertically downward state, whatever state one might start in. This motion is called bipolar oscillation.

The motion changes qualitatively and quantitatively with the inclusion of the third flavor. There are two kinds of contribution due to the inclusion of the third flavor. First, we have some extra contributions to \mathbf{B}^H that depend on ϵ , which changes the effective values of ω and θ_{13} . These do not change the motion qualitatively. The second type of contribution is more interesting. It is due to the excursions of the polarization vectors into the \mathbb{Q} subspace under the influence of \mathbf{B}^L . In particular, the length of \mathbf{P}^H is not preserved anymore. To see this clearly, we take the dot product of \mathbf{P}^H with Eq. (3.34) and that of \mathbf{P}^L with Eq. (3.35) to get

$$|\dot{\mathbf{P}}^H|^2/2 = -|\dot{\mathbf{P}}^L|^2/2 = \mathbf{P}^H \cdot \mathbf{H}^L \times \mathbf{P}^L . \quad (3.46)$$

We can clearly see that $|\mathbf{P}^H|$, which was a conserved quantity in the two-flavor case, no longer remains so. The non-conservation is proportional to $|\mathbf{H}^L|$ and $|\mathbf{P}^L|$, both of which go to zero in the two-flavor limit. The addition of the third flavor makes the motion of the projection of \mathbf{P} in the \mathbf{e}_3 – \mathbf{e}_8 plane fairly complicated in general,

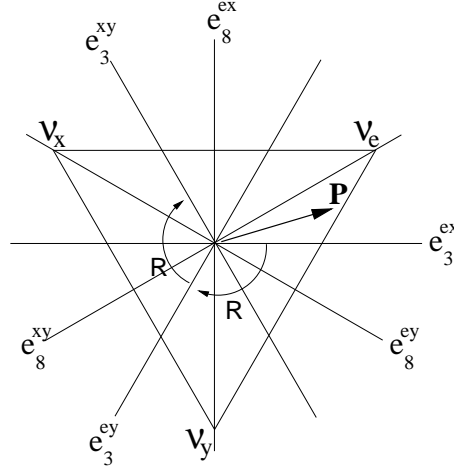


Figure 3.3: Useful coordinate choices on \mathbf{e}_3 – \mathbf{e}_8 plane.

and we shall study it in some interesting regimes in Sec. 3.5.

3.4 Three-flavor dynamics

In this section we extend the method presented in the last section, to include the leading corrections due to the mixing of the third flavor. Let us illustrate our prescription in the vacuum limit, where the matter effects as well as the nonlinear effects are neglected. The prescription will later be easily generalized to finite matter densities and significant neutrino-neutrino interactions.

From Eq. (3.16), the Bloch vector \mathbf{B} may be decomposed as

$$\omega \mathbf{B} = h\omega \mathbf{B}^{(1)} + h\epsilon\omega \mathbf{B}^{(2)} + h\epsilon\omega s_{13} \mathbf{B}^{(3)} \quad (3.47)$$

with

$$\mathbf{B}^{(1)} = s_{13}^2 \hat{\mathbf{e}}_3 - 2(3c_{13}^2 - 1)/(2\sqrt{3}) \hat{\mathbf{e}}_8 + (1 - \epsilon s_{12}^2) \sin 2\theta_{13} \hat{\mathbf{e}}_4, \quad (3.48)$$

$$\mathbf{B}^{(2)} = -(c_{12}^2 - c_{13}^2 s_{12}^2) \hat{\mathbf{e}}_3 + (3c_{13}^2 - 1)/(2\sqrt{3}) \hat{\mathbf{e}}_8 + c_{13} \sin 2\theta_{12} \hat{\mathbf{e}}_1, \quad (3.49)$$

$$\mathbf{B}^{(3)} = 3s_{13}(2c_{12}^2 - 1)/(2\sqrt{3}) \hat{\mathbf{e}}_8 - \sin 2\theta_{12} \hat{\mathbf{e}}_6. \quad (3.50)$$

Note that $\mathbf{B}^{(1)}$ lies completely in \mathbb{K}^{ey} , $\mathbf{B}^{(2)}$ in \mathbb{K}^{ex} , and $\mathbf{B}^{(3)}$ in \mathbb{K}^{xy} .

In Fig. 3.3, we show three coordinate frames $e-x$, $e-y$ and $x-y$ in the \mathbf{e}_3 - \mathbf{e}_8 plane. These frames are defined such that, if \mathbf{P} is the projection of \mathbf{P} in the \mathbf{e}_3 - \mathbf{e}_8 plane, the components $\mathbf{B}^{(1)}$, $\mathbf{B}^{(2)}$, $\mathbf{B}^{(3)}$ in Eq. (3.50) separately cause \mathbf{P} to move along \mathbf{e}_3^{ey} , \mathbf{e}_3^{ex} , \mathbf{e}_3^{xy} respectively. In order to reduce the motions due to $\mathbf{B}^{(1)}$, $\mathbf{B}^{(2)}$, $\mathbf{B}^{(3)}$ separately to two flavor problems as in Sec. 3.3, we write

$$\mathbf{B}^{ey} = \mathbf{R}\mathbf{B}^{(1)}, \quad \mathbf{B}^{ex} = \mathbf{B}^{(2)}, \quad \mathbf{B}^{xy} = \mathbf{R}^2\mathbf{B}^{(3)}, \quad (3.51)$$

where \mathbf{R} is the rotation matrix in Eq. (3.40) that rotates the \mathbf{X}_3 and \mathbf{X}_8 components of a Bloch vector in the \mathbf{e}_3 - \mathbf{e}_8 plane by $-2\pi/3$. The vectors \mathbf{B}^{ey} , \mathbf{B}^{ex} , \mathbf{B}^{xy} are then simply $\mathbf{B}^{(1)}$, $\mathbf{B}^{(2)}$, $\mathbf{B}^{(3)}$ in the frames $e-y$, $e-x$, $x-y$ respectively.

We can then write Eq. (3.47) as

$$\omega\mathbf{B} = \omega^{ey}\mathbf{R}^{-1}\mathbf{B}^{ey} + \omega^{ex}\mathbf{B}^{ex} + \omega^{xy}\mathbf{R}^{-2}\mathbf{B}^{xy}, \quad (3.52)$$

with the “frequencies” defined as

$$\omega^{ey} = h\omega \quad \omega^{ex} = h\epsilon\omega \quad \omega^{xy} = h\epsilon\omega s_{13} \sin 2\theta_{12}, \quad (3.53)$$

and the “magnetic fields” as

$$\mathbf{B}^{ey} = \cos 2\theta_{13} \hat{\mathbf{e}}_3 + (1 - \epsilon s_{12}^2) \sin 2\theta_{13} \hat{\mathbf{e}}_{\perp}^{ey} - (1 - 3s_{13}^2)/(\sqrt{3}) \hat{\mathbf{e}}_8 \quad (3.54)$$

$$\mathbf{B}^{ex} = -(c_{12}^2 - c_{13}^2 s_{12}^2) \hat{\mathbf{e}}_3 + c_{13} \sin 2\theta_{12} \hat{\mathbf{e}}_{\perp}^{ex} + (3c_{13}^2 - 1)/(2\sqrt{3}) \hat{\mathbf{e}}_8, \quad (3.55)$$

$$\mathbf{B}^{xy} = -\hat{\mathbf{e}}_{\perp}^{xy} - \sqrt{3}s_{13} \cos 2\theta_{12}/(4 \sin 2\theta_{12}) \hat{\mathbf{e}}_8. \quad (3.56)$$

The vectors \mathbf{e}_4 , \mathbf{e}_1 , \mathbf{e}_6 are the directions transverse to the \mathbf{e}_3 - \mathbf{e}_8 plane that are relevant in the three frames, and can be written as \mathbf{e}_{\perp}^{ey} , \mathbf{e}_{\perp}^{ex} , \mathbf{e}_{\perp}^{xy} respectively. The $B^{\alpha\beta}$ are normalized such that $|B_3^{\alpha\beta}|^2 + |B_{\perp}^{\alpha\beta}|^2 = 1 + \mathcal{O}(\epsilon, s_{13}^2)$. The separate motion due to each $B^{\alpha\beta}$ is then a precession about $B_3^{\alpha\beta} \hat{\mathbf{e}}_3 + B_{\perp}^{\alpha\beta} \hat{\mathbf{e}}_{\perp}$ with a frequency $\omega^{\alpha\beta}$, where the half-angle of the cone is given by $\tan \theta^{\alpha\beta} = |B_{\perp}^{\alpha\beta}/B_3^{\alpha\beta}|$.

The net motion of the polarization vector may be interpreted as the combination of two-flavor precessions about \mathbf{e}_{\perp}^{ey} , \mathbf{e}_{\perp}^{ex} and \mathbf{e}_{\perp}^{xy} respectively. It can immediately be

seen from Eq. (3.53) that

$$|\omega^{ey}| \gg |\omega^{ex}| \gg |\omega^{xy}|, \quad (3.57)$$

i.e. the precession frequencies are hierarchical. Therefore, the motion due to slower frequencies may be neglected over short time scales. More precisely, if we coarse-grain the equation of motion Eq. (3.23) in r over scales corresponding to ω^{ey} , the effects of ω^{ex} and ω^{xy} are negligible. The slowest variation in the solution is due to ω^{xy} , which modulates the faster motion due to ω^{ex} , which in turn modulates the motion at still shorter scales due to ω^{ey} .

Let us denote the evolution of $\mathbf{P}(r)$ under the action of \mathbf{B}^{ey} , \mathbf{B}^{ex} , \mathbf{B}^{xy} by the operators $\mathbf{S}^{ey}(r)$, $\mathbf{S}^{ex}(r)$, $\mathbf{S}^{xy}(r)$ respectively. As long as the condition in Eq. (3.57) is valid, we can write

$$\mathbf{P}(r) = \mathbf{S}^{ey}(r) \mathbf{S}^{ex}(r) \mathbf{S}^{xy}(r) \mathbf{P}(0), \quad (3.58)$$

where the evolution operators are of the form

$$\mathbf{S}^{ey}(r) = \mathbf{R}^{-1} \begin{pmatrix} \eta(\omega^{ey}, \theta^{ey}, \mu, r) & 0 \\ 0 & 1 \end{pmatrix} \mathbf{R}, \quad (3.59)$$

$$\mathbf{S}^{ex}(r) = \begin{pmatrix} \eta(\omega^{ex}, \theta^{ex}, \mu, r) & 0 \\ 0 & 1 \end{pmatrix}, \quad (3.60)$$

$$\mathbf{S}^{xy}(r) = \mathbf{R}^{-2} \begin{pmatrix} \eta(\omega^{xy}, \theta^{xy}, \mu, r) & 0 \\ 0 & 1 \end{pmatrix} \mathbf{R}^2. \quad (3.61)$$

Here $\eta(\omega^{\alpha\beta}, \theta^{\alpha\beta}, \mu, r)$ are the evolution functions that can be calculated in a two-flavor approximation using the results in previous literature. In general, the frequencies of these evolution functions are determined by $\omega^{\alpha\beta}$ s and the amplitudes are determined by the effective mixing angle $\theta^{\alpha\beta}$ s. Each evolution operator $\mathbf{S}^{\alpha\beta}$ takes the state \mathbf{P} to the respective $\alpha - \beta$ frame in which $P_8^{\alpha\beta}$ stays constant and $P_3^{\alpha\beta}$ undergoes precession, and brings \mathbf{P} back to the $\mathbf{e}_3 - \mathbf{e}_8$ frame after precession. Note that the matrices $\mathbf{S}^{\alpha\beta}$ are not unitary. The order in which they are operated should be such that the slower oscillations act like an amplitude modulation for the faster ones.

It is easy to calculate $\rho_{\nu_e\nu_e}$ using Eq. (3.14) as

$$\rho_{\nu_e\nu_e}(r) = \frac{1}{3} + \frac{\mathbf{P}(r) \cdot \mathbf{e}_e}{2} = \frac{1}{3} + \frac{1}{\sqrt{3}} \left(-\frac{\sqrt{3}}{2} P_3^{ey}(r) + \frac{1}{2} P_8^{ey}(r) \right), \quad (3.62)$$

where $\mathbf{P}(r)$ is given by Eq. (3.58), and P_3^{ey}, P_8^{ey} are components along \mathbf{e}_3^{ey} and \mathbf{e}_8^{ey} respectively. If neglect effects of the slowest frequency ω^{xy} , the expressions for $P_3^{ey}(r)$ and $P_8^{ey}(r)$ may be written as

$$P_3^{ey}(r) = \eta(\omega^{ey}, \theta^{ey}, \mu, r) \left(-\frac{1}{2} \eta(\omega^{ex}, \theta^{ex}, \mu, r) P_3(0) - \frac{\sqrt{3}}{2} P_8(0) \right), \quad (3.63)$$

$$P_8^{ey}(r) = \left(+\frac{\sqrt{3}}{2} \eta(\omega^{ex}, \theta^{ex}, \mu, r) P_3(0) - \frac{1}{2} P_8(0) \right). \quad (3.64)$$

In the presence of ordinary matter and when the nonlinear effects may be neglected, the same prescription stays valid, simply with the replacements

$$\hat{\mathbf{e}}_1 \rightarrow \cos \zeta(r) \hat{\mathbf{e}}_1 + \sin \zeta(r) \hat{\mathbf{e}}_2, \quad \hat{\mathbf{e}}_4 \rightarrow \cos \zeta(r) \hat{\mathbf{e}}_4 + \sin \zeta(r) \hat{\mathbf{e}}_5 \quad (3.65)$$

with $\zeta(r) = \int_0^r V(r') dr'$. It may be seen from Eq. (3.26) that these replacements take \mathbf{B} to \mathbf{B}^{int} , so that the effect of MSW is taken into account by going to the interaction frame. As observed in Sec. 3.2, fast oscillations with a frequency $\sim V(r)$ will average out the sinusoidal terms, thus decreasing the contribution from the transverse components of $\mathbf{B}^{(int)\alpha\beta}$.

The above solution works even when the nonlinear effects dominate. The nonlinear potential $H_{\nu\nu}(r)$ in Eq. (2.43) is independent of energy, therefore neutrinos of all energies precess with a common frequency in all the two-flavor subspaces. The motion is therefore similar to the vacuum case discussed above, with the replacement $\omega \rightarrow \langle \omega \rangle$ as given in Sec. 3.5.2. We have thus completed our program of expressing three-flavor effects purely in terms of two-flavor effects. The r -dependent functions $\eta(r)$ are known analytically for oscillations in vacuum and for synchronized oscillations, where we can explicitly check our ansatz. In the case of bipolar oscillations, the situation is more complicated since these are not sinusoidal oscillations, rather

\mathbf{P} remains almost static for a period of time and swings through the lowest energy state in a rapid burst. As a result, the fast- or slow-ness of bipolar oscillations as compared to the other precessions is time dependent. We therefore can obtain a qualitative understanding of bipolar oscillations in the three neutrino framework, but only a heuristic form of the analytic solution. We provide some explicit solutions for $\eta(r)$ in the next section.

3.5 Flavor conversion mechanisms

For two flavors, one can obtain exact/approximate analytical solutions to the equations of motion for the limiting values of matter density ($\lambda(r)$) and neutrino density ($\mu(r)$). We showed in Sec. 3.4 that the three-flavor case can be thought to be a superposition of two two-flavor evolutions. In this section we illustrate that explicitly using some simple examples.

For the numerical evaluations in this section, we fix $|\Delta m_{\text{atm}}^2| = 2.5 \times 10^{-3} \text{ eV}^2$ and $\theta_{12} = 0.6$. We also choose a box-spectrum for the neutrino flux i.e. $f(\omega)$ is a constant for ω corresponding to the energy range $E = (1-51) \text{ MeV}$, and zero elsewhere. We use the publicly available Sundials CVODE package [101] to solve the equations.

3.5.1 Vacuum and MSW oscillations

We start with looking at neutrino oscillations in vacuum/matter, with no nonlinear effects. Although this situation has been analyzed in literature in great detail, we illustrate it here in order to familiarize the reader with the analysis in terms of $\mathbf{P}_3^{ey}, \mathbf{P}_8^{ey}$ and the “ $\mathbf{e}_3\text{--}\mathbf{e}_8$ ” triangle. This triangle, shown in Fig. 3.4, helps in understanding the three-neutrino features of flavor conversions. The projection of \mathbf{P} on the $\mathbf{e}_3\text{--}\mathbf{e}_8$ plane represents the flavor content, the allowed region being an equilateral triangle. The three vertices of the triangle represent the three states ν_e, ν_x and ν_y (anticlockwise, from top right). States that lie on the edges connecting them are admixtures of only those two flavors. The interior of the triangle represents

- If ω and $\epsilon\omega$ were commensurate, the orbits in the triangle would be closed curves. However, that is a fine-tuned situation. In general, if ϵ is not rational, the orbits do not close, but drift parallel to themselves periodically. Indeed, the orbits are analogous to the well-known Lissajous figures.
- P_8^{ey} only has slow modes corresponding to the frequency $\epsilon\omega$. These slow oscillations modulate the amplitude of the upper envelope of $|P_3^{ey}|$ because the maximum value that $|P_3^{ey}|$ can take is reduced when P_8^{ey} deviates from its maximum value of $1/\sqrt{3}$. The above can be clearly seen from the triangle diagram.
- P_3^{ey} oscillations involve both frequencies, ω and $\epsilon\omega$. The maximum deviation of P_3^{ey} from unity is governed by the amplitude of modulation of its upper envelop (which depends on $\sin^2 2\theta_{13}$) and the amplitude of faster oscillations superimposed on it (which depends on $\sin^2 2\theta_{12}$).
- In the two-flavor limit we ignore the mixing with ν_x , and as a result P_8^{ey} remains constant. In the triangle, this corresponds to the motion being confined to a line parallel to the \mathbf{e}_3^{ey} axis. Indeed, the effect of the third flavor is to extend the motion of \mathbf{P} to the entire triangle, as opposed to only along a line. The deviation of \mathbf{P} from this line quantifies the extent of three-flavor effects.
- The amplitude of oscillations can be read off from the triangle as the extent of the orbit along the $\nu_e-\nu_y$ edge ($2\sin^2 2\theta_{13}$) and along the $\nu_e-\nu_x$ edge ($2\sin^2 2\theta_{12}$).
- In the presence of matter, mixing angles are suppressed or enhanced depending on the energy and matter density. For $\lambda \sim \epsilon\omega$, the MSW resonance occurs, and the effective mixing angle becomes almost maximal, as it happens for the low energy mode shown in the figure. At $\lambda \gg \epsilon\omega$, the state ν_x decouples because of the suppression of the mixing angle in matter, making this an effectively two-flavor $\nu_e \leftrightarrow \nu_y$ problem. The oscillations in P_8^{ey} have vanishing amplitude and the motion in the triangle is restricted to the $\nu_e-\nu_y$ edge.

- At even larger matter densities, $\lambda \gg \omega$, the amplitude of $\nu_e \leftrightarrow \nu_y$ oscillations, which is the amplitude of P_3^{ey} oscillations, starts decreasing and the motion in the triangle becomes more and more confined to be near the ν_e vertex as in the case of the high energy mode shown in the figure.

All the above features may be understood analytically through Eqs. (3.62)-(3.64) and the two-flavor evolution functions

$$\eta(\omega^{ey}, \theta^{ey}, \mu \rightarrow 0, r) = 1 - 2 \sin^2 2\theta_{13} \sin^2 \left(\frac{h\omega r}{2} \right), \quad (3.66)$$

$$\eta(\omega^{ex}, \theta^{ex}, \mu \rightarrow 0, r) = 1 - 2 \sin^2 2\theta_{12} \sin^2 \left(\frac{h\epsilon\omega r}{2} \right). \quad (3.67)$$

The above expressions are approximate, since we ignore the slowest frequency modes (depending on ω^{xy}) and assume complete factorization. We find however, that these expressions agree with the numerical solution reasonably well.

In the case of finite but constant matter density, we use the angles $\theta^{\alpha\beta}$ and frequencies $\omega^{\alpha\beta}$ in matter, both of which are energy dependent. Note that the amplitudes in this case are proportional to $2 \sin^2 2\theta^{\alpha\beta}$ in matter and can be maximal (spanning a full edge of the triangle) when there is an MSW resonance.

When the matter density encountered by the neutrino varies such that neutrinos pass through an MSW resonance, they undergo flavor transitions with adiabaticities depending on their energy, the relevant mixing angle and the matter profile. In the limit of a small mixing angle, a completely adiabatic H resonance is represented by a reflection of the neutrino state about \mathbf{e}_8^{ey} in the \mathbf{e}_3 - \mathbf{e}_8 triangle. A non-adiabatic H resonance corresponds to a state that tries to move towards this reflected point, but does not completely succeed. Passage through the L resonance similarly corresponds to a reflection about \mathbf{e}_8^{ex} .

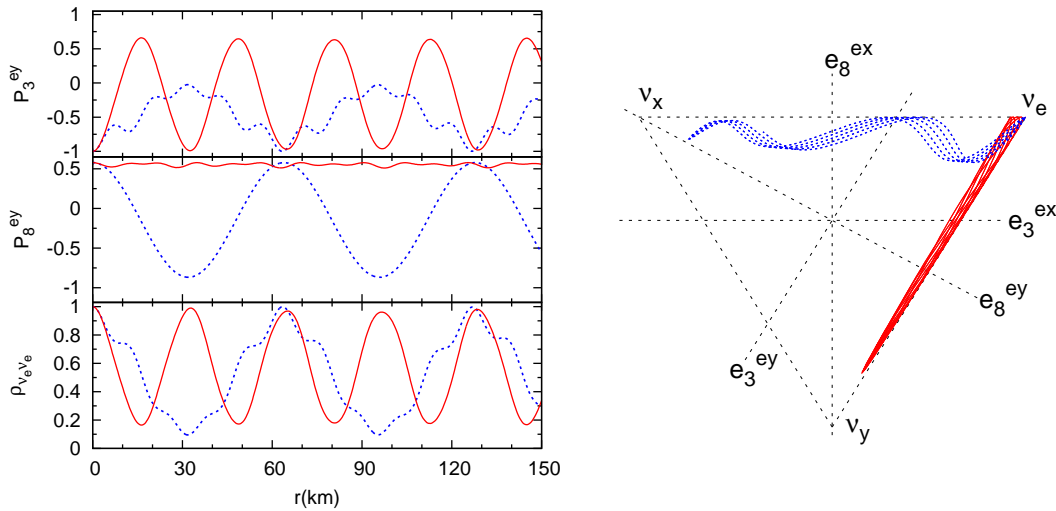


Figure 3.5: Synchronized oscillations for neutrinos of $E = 20.0$ MeV and 29.6 MeV, which overlap completely. We choose $\epsilon = 1/5$ to emphasize the nature of oscillations, $\theta_{13} = 0.2$ and $\mu = 100 \text{ km}^{-1}$. Oscillations in vacuum and matter are shown by dotted (blue) and undotted (red) lines respectively. For matter, we choose normal hierarchy and $\lambda = 0.5 \text{ km}^{-1}$. Note that the orbits on the triangle are the same for different energies.

3.5.2 Synchronized oscillations

At extremely large neutrino densities, it is expected that neutrinos of all energies oscillate synchronously³ with a common frequency $\langle \omega^{\alpha\beta} \rangle$ about $\mathbf{B}^{\alpha\beta}$, given in the two-flavor case by [94, 95]

$$\langle \omega^{\alpha\beta} \rangle = \frac{\omega^{\alpha\beta}}{\omega} \frac{\mathbf{D} \cdot \mathbf{D}^{(1)}}{|\mathbf{D}|^2}, \quad (3.68)$$

where \mathbf{D} 's are the moments defined in Eq. (3.28). The frequency $\langle \omega^{\alpha\beta} \rangle$ crucially depends on the neutrino energy spectrum. The box-spectrum that we have chosen corresponds to $\langle \omega^{ey} \rangle \approx 0.49 \text{ km}^{-1}$. In Fig. 3.5 we show P_3^{ey} , P_8^{ey} and $\rho_{\nu_e \nu_e}$ as functions of the radial coordinate r for synchronized neutrino oscillations.

The following observations may be made from the figure:

- The observations in Sec. 3.5.1 remain true, except that neutrinos of all energies oscillate with a common frequency in vacuum in the two flavor limits of each

³It has been shown in [102] that the synchronization is not perfect for “non-trivial” initial spectra, and one can get self-induced parametric resonance.

of the $\alpha - \beta$ subspaces. The response of all neutrinos to the neutrino-neutrino potential is thus identical.

- Even in the presence of matter, the synchronized oscillation amplitude is independent of energy, unlike what happens for non-linear oscillations.
- The amplitude of the slower oscillations is almost maximal because, in the chosen example, $\lambda \sim \epsilon \langle \omega \rangle$.
- The orbits drift periodically, even if ω and $\epsilon \omega$ are commensurate, because $\langle \omega \rangle$ and $\langle \epsilon \omega \rangle$ are not commensurate in general. This is due to corrections to Eq. (3.68) arising out of incomplete synchronization.

The above observations are explained analytically along the same lines as the vacuum/MSW case. The two-flavor evolution functions are given by

$$\eta(\omega^{ey}, \theta^{ey}, \mu \gg \omega^{ey}, r) = 1 - 2 \sin^2 \langle 2\theta_{13} \rangle \sin^2 \left(\frac{h \langle \omega \rangle r}{2} \right), \quad (3.69)$$

$$\eta(\omega^{ex}, \theta^{ex}, \mu \gg \omega^{ex}, r) = 1 - 2 \sin^2 \langle 2\theta_{12} \rangle \sin^2 \left(\frac{h \epsilon \langle \omega \rangle r}{2} \right). \quad (3.70)$$

In the plots we see that fast oscillations have wavelength $2\pi/\omega \approx 12$ km. This matches the value of $\langle \omega^{ey} \rangle$ calculated from Eq. (3.68).

In the presence of a finite matter density, the MSW potential λ also takes an effective average value given by [94, 95]

$$\langle \lambda \rangle = \lambda \frac{\mathbf{D} \cdot \mathbf{S}}{|\mathbf{D}|^2}. \quad (3.71)$$

Naturally, the mixing angle is also the same for all energies, since

$$\sin^2 \langle 2\theta^{\alpha\beta} \rangle = \frac{\sin^2 2\theta^{\alpha\beta}}{(\langle \lambda \rangle / \langle \omega^{\alpha\beta} \rangle - \cos 2\theta^{\alpha\beta})^2 + \sin^2 2\theta^{\alpha\beta}}. \quad (3.72)$$

Thus not only the frequency, but also the amplitude of oscillations is universal in the synchronized limit. The MSW resonance is collective, occurring with the same adiabaticity for all neutrinos/antineutrinos at the same λ when the relevant

condition is met, as was shown in the two-flavor case [94, 95, 96]. The factorization shown in Sec. 3.3 allows the result to be extended to the three-flavor situation.

3.5.3 Bipolar Oscillations

When the hierarchy is inverted and there are comparable numbers of neutrinos and antineutrinos in the system, i.e. $\mu|\mathbf{D}| \sim \omega|\mathbf{B}|$, the influence of the ω and μ terms in the equations of motion depends crucially on the relative orientation of \mathbf{D} , \mathbf{B} and the magnitude of \mathbf{D} itself. This subtle interplay gives rise to bipolar oscillations.

Many of the notions about bipolar oscillations in the two-flavor formalism [60, 61] remain valid with three flavors, since they do not depend on the number of flavors, or equivalently, on the dimensionality of the Bloch vectors. The system is best understood in terms of the ‘‘pendulum vector’’ \mathbf{Q} defined in the interaction picture as [60, 61]

$$\mathbf{Q} \equiv \mathbf{S} - \frac{\omega}{\mu}\mathbf{B}, \quad (3.73)$$

in terms of which the equations of motion are

$$\dot{\mathbf{Q}} = \mu\mathbf{D} \times \mathbf{Q} - \frac{\omega}{\mu}\dot{\mathbf{B}}, \quad (3.74)$$

$$\dot{\mathbf{D}} = \omega\mathbf{B} \times \mathbf{Q}. \quad (3.75)$$

The absence of $\lambda(r)$ is deceptive. The \mathbf{B} contains λ , and in principle that could be important, but it turns out that the dependence on λ is only logarithmic.

The antisymmetry of the generalized cross product in Eq. (3.22) implies that even in the case of three flavors, $|\mathbf{Q}|^2$ and $\mathbf{D} \cdot \mathbf{B}$ are conserved for large μ .

In the two-flavor case, the motion can be understood in terms of a spherical pendulum [60, 61], with the total energy given by $\omega\mathbf{B} \cdot \mathbf{Q} + \mu|\mathbf{D}|^2/2$. Starting with ν_e and $\bar{\nu}_e$, for normal hierarchy, the pendulum is stable and executes only small oscillations, because \mathbf{Q} points in the direction of \mathbf{B} already. For inverted hierarchy, however, \mathbf{Q} behaves like an inverted pendulum, which tries to relax to its stable position. The polarization vectors then remain almost static, but periodically dip to

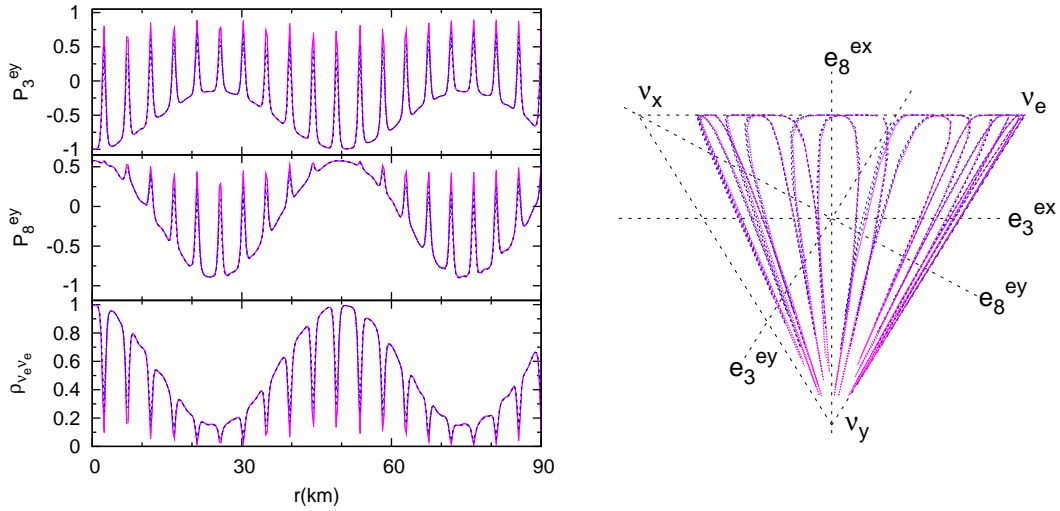


Figure 3.6: Bipolar oscillations at small λ for neutrinos (dotted, blue) and 20% fewer antineutrinos (undotted, pink) of different energies, which almost overlap. We choose inverted hierarchy, $|\epsilon| = 1/30$, $\theta_{13} = 0.01$, $\mu = 10 \text{ km}^{-1}$ and $\lambda = 0.001 \text{ km}^{-1}$. Note that the plots are the same for different energies, because of strong collective behavior.

the configuration with the lowest potential energy $\mathbf{B} \cdot \mathbf{Q}$. Thus for inverted hierarchy, one can have a large flavor swap during the dip. The duration between successive dips is given by $\tau^{bip} \approx \sqrt{\omega\mu|\mathbf{Q}|}$ with logarithmic corrections depending on θ and λ . Since $\mu > \omega$, individual \mathbf{P} remain bound to each other, and therefore behave identically to \mathbf{Q} .

Addition of a third flavor may change the behavior significantly, as we show in Figs. 3.6 and 3.7 for two extreme values of λ . We consider the case of inverted hierarchy, and a box-spectrum of energies $E = (1-51) \text{ MeV}$ with the number of antineutrinos as $(1 - \alpha)$ times the number of neutrinos, with $\alpha = 0.2$. Given that the hierarchy in the solar sector is normal, we expect bipolar effect only in the $e - y$ subspace, combined with usual neutrino oscillations in the $e - x$ subspace. The following observations may be made from the figures:

- The evolution of both P_3^{ey} and P_8^{ey} consists of a series of bipolar “kinks” as in the two-flavor case [60, 61], modulated by an envelope with the frequency $\langle \omega^{ex} \rangle$. The evolutions for neutrinos and antineutrinos closely follow one another, which is expected from the conservation of $\mathbf{B} \cdot \mathbf{D}$.

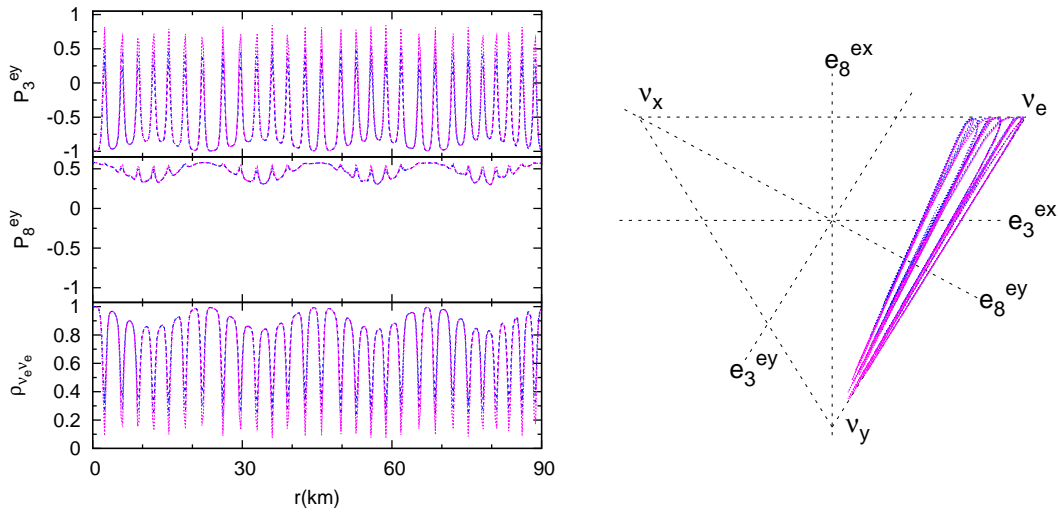


Figure 3.7: Bipolar oscillations at large λ for neutrinos (dotted, blue) and antineutrinos (undotted, pink) of different energies, which almost overlap. We choose inverted hierarchy, $|\epsilon| = 1/30$, $\theta_{13} = 0.01$, $\mu = 10 \text{ km}^{-1}$ and $\lambda = 0.3 \text{ km}^{-1}$. Note that the plots are the same for different energies, because of strong collective behavior.

- Significant three-flavor effects are present for small λ , since the whole triangle is seen to be filled with oscillations, forming a “petal structure” (Fig. 3.6). It may be interpreted as a combination of slow $\nu_e \leftrightarrow \nu_x$ oscillations and bipolar oscillations that tend to take the state towards ν_y in periodic bursts.
- The extent of motion towards ν_y depends mainly on the asymmetry α , whereas that towards ν_x depends on $\sin^2 2\theta_{12}$.
- For large λ (Fig. 3.7), the oscillations in the $e - x$ sector are suppressed since the effective mixing angle θ_{12} in matter becomes small. The amplitude of the bipolar motion is however not affected substantially.

Bipolar oscillations (even in the two-flavor limit) do not have a sinusoidal form, hence they are not associated with a fixed frequency. They may be looked upon as a combination of a low frequency (during the time that the ν_y component is stationary, which we shall call the A phase) and a high frequency (the sudden dip towards ν_y , which we shall call the B phase). Therefore, our prescription in Sec. 3.4 has to be applied with care. Note that the order of evolution matrices in Eq. (3.61) is supposed to be in the decreasing order of frequencies. Even if we neglect the

slow evolution due to \mathbf{B}^{xy} , strictly speaking during the A phase, one should use the order $\mathbf{S}^{ex}\mathbf{S}^{ey}$ and during the B phase, the order should be $\mathbf{S}^{ey}\mathbf{S}^{ex}$. However, we find numerically that the evolution $\mathbf{S}^{ex}\mathbf{S}^{ey}$ closely matches the three-flavor solution over the complete evolution. This therefore may be taken to be the heuristic solution for the bipolar oscillations in the three-flavor case.

We have not considered normal hierarchy, in which we expect that starting with ν_e we'll have a stable system that will not undergo bipolar oscillations, whereas starting with ν_x or ν_y , we'll have independent bipolar oscillations towards ν_e .

3.5.4 Spectral splitting

As a system of neutrinos and antineutrinos transits from the nonlinear regime ($\mu \gg \omega$) to vacuum ($\mu \sim 0$), the polarization vectors \mathbf{P} keep trying to align with \mathbf{H} in the adiabatic approximation. Due to the conservation of $\mathbf{B} \cdot \mathbf{D}$, as shown in Sec. 3.5.3, this alignment is not possible for all \mathbf{P} . The way the system aligns maximally while still obeying the constraint, is to align only a part of the spectrum, while anti-aligning some parts. This causes sharp changes in the final spectrum, that are called spectral splits.

In general, we do not know how to predict the final spectrum accurately. We shall therefore confine ourselves to the situations where there is only one spectral split, thus one can predict the final spectra just on the basis of conservation laws. The dynamics of spectral splitting are not clear, except when adiabaticity predicts a single split [62, 63].

It is simpler to understand this phenomenon in the instantaneous mass basis. i.e. the interaction picture in mass basis. In the chosen basis, $\mathbf{B} = \mathbf{B}^H + \epsilon\mathbf{B}^L$, where \mathbf{B}^H is along \mathbf{e}_8 and \mathbf{B}^L is along \mathbf{e}_3 . The equation of motion for the global polarization vector is

$$\dot{\mathbf{D}} = (\mathbf{B}^H + \epsilon\mathbf{B}^L) \times \mathbf{M}, \quad (3.76)$$

where the ‘‘magnetic moment’’ of the system is $\mathbf{M} = \int d\omega f(\omega)\omega \mathbf{P}(\omega)$. In the mass

basis this is

$$\dot{\mathbf{D}} = - \left(\frac{2}{\sqrt{3}} \mathbf{e}_8 + \epsilon \mathbf{e}_3 \right) \times \mathbf{M}. \quad (3.77)$$

The vector on the r.h.s. is orthogonal to both \mathbf{e}_3 and \mathbf{e}_8 . The reason is that $f_{a38} = 0$ for $a = 1, \dots, 8$ and for all permutations of the indices. As a consequence, the vector $\dot{\mathbf{D}}$ has no \mathbf{e}_3 or \mathbf{e}_8 component so that $\dot{D}_3 = 0$ and $\dot{D}_8 = 0$. In a general basis this implies

$$\partial_r(\mathbf{D} \cdot \mathbf{B}^H) = 0 \quad \text{and} \quad \partial_r(\mathbf{D} \cdot \mathbf{B}^L) = 0. \quad (3.78)$$

This is the equivalent of “flavor-lepton number conservation” $\partial_r(\mathbf{D} \cdot \mathbf{B}) = 0$ in the two-flavor context [60, 61, 62, 63]. In other words, in the three-flavor context we have two flavor-lepton numbers that are separately conserved.

We now explain the factorization of the two spectral splits [79, 80]. The first split to develop is driven by the atmospheric mass difference and thus can be called the H split. As in [62, 63] we go to a rotating frame, at first rotating around the \mathbf{B}^H direction with the frequency ω_c^H . The single-mode Hamiltonians in this co-rotating frame are

$$\mathbf{H} \approx (\omega - \omega_c^H) \mathbf{B}^H + \mu \mathbf{P}, \quad (3.79)$$

neglecting for now the much smaller term $\epsilon\omega\mathbf{B}^L$. This is justified because, when $\mu \gtrsim \omega$ (and thus $\mu \gg \epsilon\omega$), the ensemble of neutrinos is in a regime where we expect spectral splitting along \mathbf{e}_8 and synchronized oscillations along \mathbf{e}_3 . Flavor conversion is thus driven primarily by \mathbf{B}^H , while \mathbf{B}^L gives sub-leading corrections due to the synchronized oscillations. Similarly, when $\mu \sim \epsilon\omega$, flavor conversion proceeds efficiently via a spectral split along \mathbf{e}_3 and is driven by \mathbf{B}^L , while \mathbf{B}^H drives vacuum oscillations along \mathbf{e}_8 .

Now, as μ adiabatically goes to zero, the co-rotation frequency ω_c^H approaches the final split frequency ω_s^H and the modes with $\omega > \omega_s^H$ will orient themselves along \mathbf{B}^H , those with $\omega < \omega_s^H$ in the $-\mathbf{B}^H$ direction. The value of ω_s^H is fixed by the conservation of P_8 . Since the evolution associated with \mathbf{B}^H has saturated, we can

next go into a frame rotating around \mathbf{B}^L where

$$\mathbf{H} \approx (\omega - \omega_c^L) \mathbf{B}^L + \mu \mathbf{P} \quad (3.80)$$

and repeat the analogous argument.

A crucial requirement for the splits to develop is the preparation of the system for the split by the generation of components of \mathbf{P} that are transverse to \mathbf{B} . Bipolar oscillations do this easily for inverted hierarchy, independent of matter effects. For the normal hierarchy, this may be achieved by MSW conversions, should they occur before the nonlinear effects end. These two kinds of splits are called “Bipolar-prepared” and “MSW-prepared” spectral splits respectively. We illustrate each of these in the following.

Bipolar-prepared spectral splits

For illustrating bipolar oscillation initiated splits, we choose two situations, with large and small λ (Fig. 3.8 and 3.9 respectively) and the hierarchy is taken to be inverted. We take box-like initial spectra $f(\omega)$ for ν_e and $\bar{\nu}_e$ energies and the flux asymmetry $\alpha = 0.33$. We observe the following from the figures:

- For large λ , there is only a single split for neutrinos, which can be seen in P_3^{ey} . The split is not visible in the triangle since the neutrinos are confined to the ν_e - ν_y edge. However, the low energy neutrinos move towards ν_e and the high energy ones towards ν_y .
- for small λ , the split is not only in P_3^{ey} but also in P_8^{ey} . There also are oscillations with large amplitudes. Some neutrino states drift towards and ultimately reach ν_y , while the others keep oscillating between ν_e and ν_x .

The above observations can be understood as follows. For large λ , the solar mixing angle is suppressed and hence the problem reduces essentially to a two-flavor one in the $e - y$ subspace. Thus, the split is only in P_3^{ey} . The split happens in neutrinos since there are more neutrinos than antineutrinos at any given energy. For small λ ,

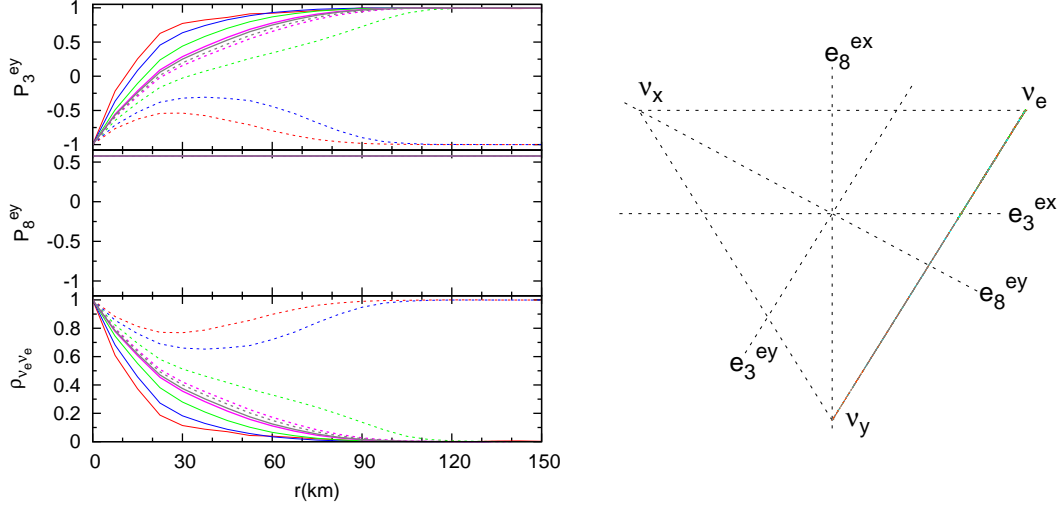


Figure 3.8: Spectral splits at large λ for neutrinos (dotted) and 33% fewer antineutrinos (undotted) with energies $E = (1-51)$ MeV. In the $\rho_{\nu_e \nu_e}$ plot, the energy of neutrinos (antineutrinos) increases (decreases) top downwards. The energies (in MeV) of the modes, shown in the figure, are 1.0 (Red), 1.5 (Blue), 3.5 (Green), 12.5 (Pink) and 32.0 (Grey). We take inverted hierarchy, $|\epsilon| = 1/30$, $\theta_{13} = 0.01$, $\mu = 10^5 (50/r(\text{km}))^4 \text{ km}^{-1}$ and $\lambda = 10 \text{ km}^{-1}$. In the \mathbf{e}_3 – \mathbf{e}_8 triangle, the evolution is always along the ν_e – ν_y edge.

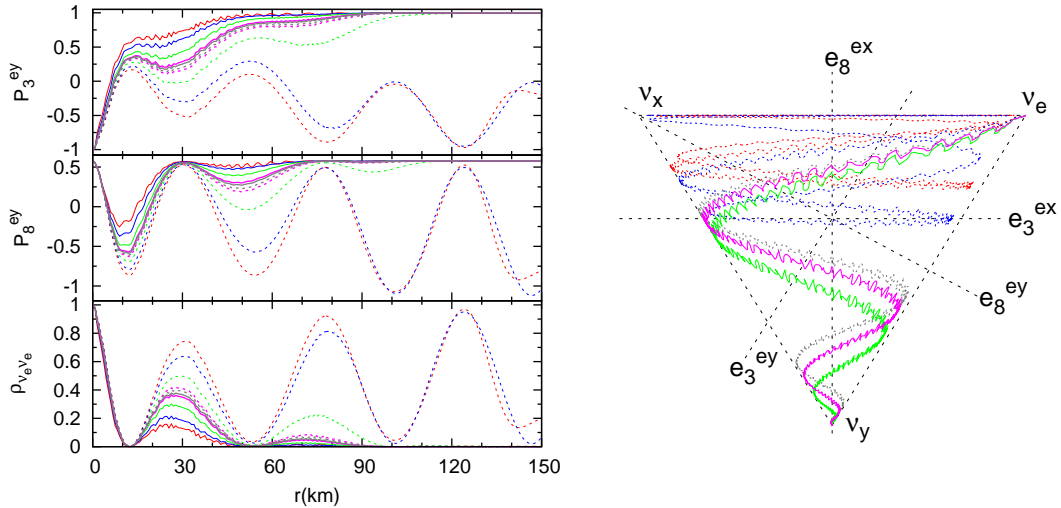


Figure 3.9: Spectral splits at small λ for neutrinos (dotted) and 33% fewer antineutrinos (undotted) with energies $E = (1-51)$ MeV. The conventions for lines is the same as that in Fig. 3.8. We take inverted hierarchy, $\epsilon = 1/30$, $\theta_{13} = 0.01$, $\mu = 10^5 (50/r(\text{km}))^4 \text{ km}^{-1}$ and $\lambda = 0.1 \text{ km}^{-1}$. In the \mathbf{e}_3 – \mathbf{e}_8 triangle, we show only some of the representative energies that have different behaviors.

in addition to the above split, there are large $\nu_e \leftrightarrow \nu_x$ oscillations, which give rise to a split that is observable also in P_8^{ey} , which was absent for large λ . In either case, the position of the split can be determined from the conservation of $\mathbf{B} \cdot \mathbf{D}$ after the split.

MSW-prepared spectral splits

Spectral splits can also be prepared by MSW effects. We consider a situation where the system passes the two MSW level crossings before the neutrino-neutrino interactions become small. The subsequent evolution to the point where the neutrino-neutrino interaction becomes negligible will then produce spectral splits. We can follow the two-flavor treatment almost step by step because the present three-flavor system is simplified by the mass-gap hierarchy $\epsilon \approx 1/30 \ll 1$. While the two conserved flavor-lepton numbers present in the three flavor case lead to two spectral splits, these will occur in sequence and their dynamics factorizes in practice.

To illustrate the dynamics of the split we consider an explicit example with only neutrinos, so that $\mathbf{D} = \int_0^\infty d\omega f(\omega) \mathbf{P}(\omega)$, and an initial “box spectrum” for $f(\omega)$, of the form

$$\rho_{ee}(\omega) = \begin{cases} (2\omega_0)^{-1} & \text{for } 0 \leq \omega \leq 2\omega_0 \\ 0 & \text{otherwise} \end{cases} . \quad (3.81)$$

At high densities $\rho_{ee}(\omega)$ coincides with $\tilde{\rho}_{33}(\omega)$ in normal hierarchy and with $\tilde{\rho}_{22}(\omega)$ in inverted hierarchy. After the MSW crossings the spectrum is still of box-like because the assumed strong neutrino-neutrino interaction ensures the same semi-adiabatic for all energies. However, \mathbf{P} now has transverse components generated due to MSW crossing. Note that after the MSW transitions we neglect ordinary matter so that the propagation eigenstates are identical with the mass eigenstates and $\tilde{\rho} = \rho$.

The situation can be visualized in terms of the \mathbf{e}_3 – \mathbf{e}_8 triangle diagram shown in Fig. 3.10 (left panel). Each point in the interior and on the boundary of the triangle represents the projection of the polarization vector \mathbf{P} in the \mathbf{e}_3 – \mathbf{e}_8 plane. For normal hierarchy, neutrinos from the ν_e burst start in the state $\nu_e \approx \tilde{\nu}_3$, where by “tilde”, we represent the instantaneous mass eigenstates. The H crossing shifts

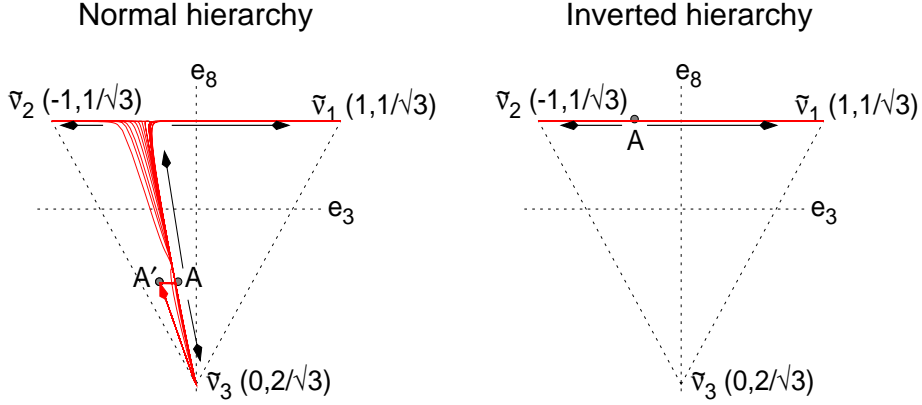


Figure 3.10: Projection of the polarization vectors $\mathbf{P}(\omega)$ on the \mathbf{e}_3 - \mathbf{e}_8 plane for our box-example. The vertices of the triangle represent instantaneous mass eigenstates. The MSW transitions, prepare the system and place it at the point A in the interior of the triangle (See the text for details.).

the neutrino state from the $\tilde{\nu}_3$ vertex towards the $\tilde{\nu}_2$ state, but only partially, due to the semiadiabatic nature of the transition. After that crossing, all neutrinos find themselves at the point A' inside the triangle. The L crossing further transports the state along a line parallel to the $\tilde{\nu}_2$ - $\tilde{\nu}_1$ edge towards $\tilde{\nu}_1$, again only partly due to the semiadiabaticity. Before the split, all the neutrinos are thus at a point A in the interior of the triangle.

The H split takes the $\omega > \omega_s^H$ modes towards the $\tilde{\nu}_3$ state ($P_3 = 0, P_8 = -2/\sqrt{3}$) and the modes $\omega < \omega_s^H$ towards some combination of $\tilde{\nu}_1$ and $\tilde{\nu}_2$, while conserving the total P_3 and P_8 . Since $\epsilon \ll 1$, the H and L splits are well separated and the high- ω modes reach the $\tilde{\nu}_3$ vertex, i.e. the H split saturates, before the L split begins. The low- ω modes propagating towards the $P_8 = 1/\sqrt{3}$ line encounter the L split that tends to take the $\omega > \omega_s^L$ modes towards $\tilde{\nu}_2$ ($P_3 = -1, P_8 = 1/\sqrt{3}$) and the $\omega < \omega_s^L$ modes towards $\tilde{\nu}_1$ ($P_3 = 1, P_8 = 1/\sqrt{3}$). In the adiabatic limit, i.e. given sufficient time to propagate from $\mu \rightarrow \infty$ to $\mu \rightarrow 0$, the H and L splits result in all neutrinos reaching one of the three vertices of the \mathbf{e}_3 - \mathbf{e}_8 triangle.

Using the conservation law for P_3 and P_8 of one can evaluate the split frequencies ω_s^H and ω_s^L . For $\omega < \omega_s^H$ we have $P_8 \rightarrow 1/\sqrt{3}$, while for $\omega > \omega_s^H$ they reach $-2/\sqrt{3}$.

In the limit of perfect adiabaticity, the conservation of P_8 implies

$$2\omega_0 P_8(0) = \frac{1}{\sqrt{3}} \omega_H^s - \frac{2}{\sqrt{3}} (2\omega_0 - \omega_H^s), \quad (3.82)$$

where P_8^0 is the common value of P_8 before the split begins. For this example, $P_8^0 = -0.50$, leading to $\omega_s^H = 0.76 \omega_0$.

When the H split saturates, all modes with $\omega > \omega_s^H$ have $P_8 = -2/\sqrt{3}$, and hence $P_3 = 0$ due to the conservation of the norm of \mathbf{P} . These modes have reached the bottom vertex of the \mathbf{e}_3 - \mathbf{e}_8 triangle and hence cannot split further due to the L split. On the other hand, for modes with $\omega < \omega_s^H$ a second split in $P_3(\omega)$ happens. These modes approach $P_3 = +1$ for $\omega < \omega_s^L$ and $P_3 = -1$ for $\omega > \omega_s^L$. Applying the conservation law for P_3 gives us

$$2\omega_0 P_3(0) = \omega_L^s - (\omega_s^H - \omega_s^L). \quad (3.83)$$

For this example $P_3^0 = -0.14$ so that $\omega_s^L = 0.24 \omega_0$.

For inverted hierarchy, the initial state here is $\tilde{\nu}_2$. The nonadiabatic L crossing takes the neutrino states partly towards $\tilde{\nu}_1$. After the L crossing and before the split, the neutrino state for all modes is along the $\tilde{\nu}_1$ - $\tilde{\nu}_2$ edge, at A as shown in Fig. 3.10 (right panel), where $P_8 = 1/\sqrt{3}$. Since all neutrinos already are in one of the extreme values of P_8 , the H split is inoperational. This corresponds to ρ_{33} remaining in its MSW-prepared initial value of 0. The L split takes $\rho_{11} \rightarrow +1$ for $\omega < \omega_s^L$ and $\rho_{11} \rightarrow 0$ for $\omega > \omega_s^L$, and vice versa for ρ_{22} . In the inverted hierarchy we have an effective two-flavor case in the $\tilde{\nu}_1$ - $\tilde{\nu}_2$ subsector. This is a consequence of the MSW-prepared initial condition. Initially $P_8^0 = 1/\sqrt{3}$. Applying now the conservation of P_8 we obtain $\omega_s^H = 2\omega_0$, i.e., the split occurs at the edge of the box and thus is not visible. The conservation law for P_3 and using in our case $P_3^0 = -0.38$, one obtains $\omega_s^L = 0.62 \omega_0$.

We show in Fig. 3.11 the mass-basis spectra of P_3 and P_8 . Thin lines are the MSW-prepared initial spectra. Thick lines show the numerical final spectra. Dotted lines show the adiabatic limiting behavior based on the lepton-number conservation

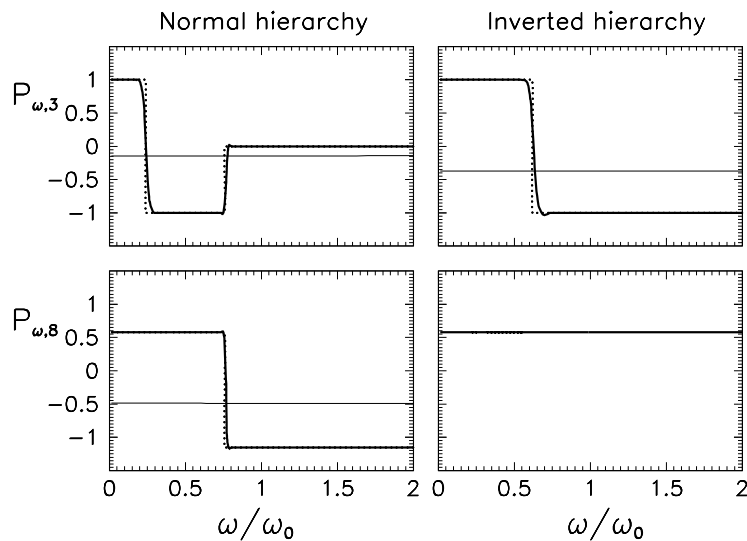


Figure 3.11: The 3 and 8 components of $\mathbf{P}(\omega)$. Thin line: initial box spectrum. Thick line: numerically evaluated final spectrum. Dotted line: analytical prediction for final spectrum.

laws. Once more the agreement is striking. We have of course assumed complete factorization of H and L splits, this requires the H split to saturate before the L split begins to occur. Imperfect adiabaticity merely leads to a smoothing of the splits which otherwise are sharp spectral steps.

3.5.5 Summarized results

We started with a general framework to calculate flavor evolution of nonlinearly coupled neutrinos and antineutrinos. We showed how to reduce any source geometry to a quasi-spherical source. We then worked out the three-flavor effects analytically, and showed that there is a sense in which the full problem breaks apart into the H and L sectors. We then generalized the known two-flavor results to explicitly demonstrate the various flavor conversion mechanisms, *viz.* vacuum oscillations, MSW oscillations, synchronized oscillations, bipolar oscillations and spectral splits, in the three-flavor case and confirmed numerically that our framework gives consistent results. We shall apply this framework to SN neutrinos in the next chapter.

Chapter 4

Flavor Conversions of Supernova Neutrinos

In this chapter, we study the effect of nonlinear oscillations and their interplay with subsequent MSW transitions inside an iron-core SN. We apply the formalism developed in Chapter 3 and identify the regions of the star where different flavor conversion mechanisms are at work. This allows us to predict the features in the observable neutrino and antineutrino spectra. We present results for inverted hierarchy, because nonlinear effects are not expected to play a significant part for normal hierarchy¹. These results are based on the paper: B. Dasgupta and A. Dighe, “*Collective three-flavor oscillations of supernova neutrinos*,” Physical Review D **77**, 113002 (2008), [arXiv:0712.3798 [hep-ph]].

4.1 Reference SN model

We define a reference SN model for our numerical study. Our input comprises of the neutrino parameters (the mass-square differences Δm_{atm}^2 and Δm_{\odot}^2 and the mixing angles θ_{13} and θ_{12}), the source geometry (parameterized by neutrinosphere radius r_0), primary neutrino fluxes F_{ν_α} (parameterized by the number flux Φ_{ν_α} , the average energy $\langle E_{\nu_\alpha} \rangle$, and the pinching ξ_{ν_α}), initial flavor state (encoded into $\mathbf{P}^0(\omega)$), MSW

¹However, during the neutronization burst phase of an O-Ne-Mg SN, this need not be true.

potential (denoted as $\lambda(r)$) and the neutrino potential (denoted as $\mu(r)$). With these inputs, we can analytically predict $\mathbf{P}(\omega)$ at the end of nonlinear evolution. Then we take the MSW crossings into account and write down the neutrino fluxes $F_{\nu_\alpha}^{obs}$ arriving at Earth.

4.1.1 Neutrino masses and mixings

We take $|\Delta m_{\text{atm}}^2| = 2.5 \times 10^{-3} \text{ eV}^2$, $|\epsilon| = |\Delta m_{\odot}^2 / \Delta m_{\text{atm}}^2| = 1/30$, $\theta_{12} = 0.6$, and two representative values of θ_{13} , *viz.* $\theta_{13} = 0.001$ (small) and 0.1 (large).

4.1.2 SN geometry and fluxes

The SN model is defined by the following choice for the emission geometry, initial flavor dependent spectra and fluxes, the neutrino potential and the matter density profile. We would like to emphasize that these choices are canonical and more importantly, the specific value of the luminosity or the spatial dependence of the neutrino potential does not affect results significantly. Any large initial value of μ (such that it exceeds ω) and its slow decrease with r gives almost identical results. In other words, the results are not fine-tuned. However, the results would depend on the flavor spectra and the matter density profile, as these determine the initial conditions, the neutrino potential and the effective mixing parameters.

Emission geometry

Neutrinos with different energies and flavors start freestreaming at different r , but flavor evolution does not start until much later. Thus the radius of the neutrinosphere r_0 is used only to set the initial conditions. We therefore use the “bulb-model” of neutrino emission from the SN as discussed in [72] with a nominal neutrinosphere at $r_0 = 10 \text{ km}$. We assume steady-state half-isotropic emission from the neutrinosphere. This completely defines the kinematics of all neutrinos and antineutrinos emitted from the SN.

Initial fluxes and spectra

We now define the flavor composition of the SN neutrinos. The flavor-dependent primary neutrino spectra at r_0 are parameterized as [24]

$$F_{\nu_\alpha}(E) = \Phi_{\nu_\alpha} \frac{N(\xi_{\nu_\alpha})}{\langle E_{\nu_\alpha} \rangle} \left(\frac{E}{\langle E_{\nu_\alpha} \rangle} \right)^{\xi_{\nu_\alpha}} \exp \left[-(\xi_\alpha + 1) \frac{E}{\langle E_{\nu_\alpha} \rangle} \right], \quad (4.1)$$

where $N(\xi) = (1 + \xi)^{1+\xi}/\Gamma(1 + \xi)$. This spectrum is normalized such that

$$\int_0^\infty dE_{\nu_\alpha} F_{\nu_\alpha}(E_{\nu_\alpha}) = \Phi_{\nu_\alpha} \quad (4.2)$$

and has the average energy $\langle E_{\nu_\alpha} \rangle$.

The above parameterization has the advantage that the spectra can be analytically integrated, including the effects of spectral pinching through ξ_α .

The number flux Φ_{ν_α} is given by $\Phi_{\nu_\alpha} = L_{\nu_\alpha}/\langle E_{\nu_\alpha} \rangle$, where L_{ν_α} is the luminosity in the flavor ν_α .

We assume the above parameters to be

$$\begin{aligned} L_{\nu_\alpha} &= 1.5 \times 10^{51} \text{ ergs/sec}, \quad \xi_\alpha = 3 \\ \langle E_{\nu_e} \rangle &= 10 \text{ MeV}, \quad \langle E_{\bar{\nu}_e} \rangle = 15 \text{ MeV}, \quad \langle E_{\nu_{x,y}, \bar{\nu}_{x,y}} \rangle = 20 \text{ MeV}. \end{aligned} \quad (4.3)$$

This choice reflects the hierarchy of number fluxes found in typical supernova models [23, 24]

$$\Phi_{\nu_e} > \Phi_{\bar{\nu}_e} > \Phi_{\nu_x} = \Phi_{\bar{\nu}_x} = \Phi_{\nu_y} = \Phi_{\bar{\nu}_y}. \quad (4.4)$$

This scenario has been extensively studied analytically as well as numerically, and gives straightforward predictions for neutrino flavor conversions. Although it is not obvious that this hierarchy is maintained at late times, in the following we will assume it as our benchmark. We must remark that qualitatively different primary neutrino spectra and/or yet undiscovered flavor effects may yield different predictions for flavor conversion and the analysis will have to be repeated appropriately.

4.1.3 Neutrino potential and matter density profile

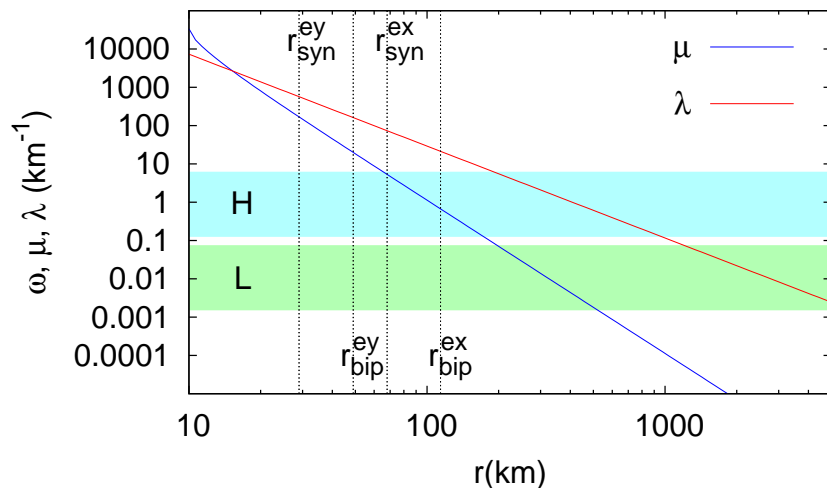


Figure 4.1: The profiles of $\lambda(r)$ and $\mu(r)$ for the SN model chosen in this section, along with the bands for the MSW resonances H and L . Also indicated are the terminal values of r where synchronized /bipolar oscillations for the $e - y$ and $e - x$ flavors take place.

Neutrino potential

The neutrino potential for $r > r_0$ for the choice of parameters in Eq. (4.3) is given by

$$\mu(r) = 0.45 \times 10^5 g(r) \text{ km}^{-1}, \quad (4.5)$$

where $g(r)$ is given in Eq. (2.37).

Matter potential

We choose the shock-wave simulation inspired density profile that corresponds to ²

$$\lambda(r) = 1.84 \times 10^6 / r^{2.4} \text{ km}^{-1}. \quad (4.6)$$

The profiles of $\lambda(r)$ and $\mu(r)$ are shown in Fig. 4.1.

²This is the same as the one used in [41] at $t=4$ sec.

4.2 Flavor conversions inside a supernova

Let's recall that $E \sim p = |\Delta m_{\text{atm}}^2|/(2\omega)$, we can rewrite the above information in terms of ω , if desired. Combining Eq. (3.12) with the definitions of moments in (3.28), allows us to calculate the values of $\mathbf{D}(r_0)$, $\mathbf{S}(r_0)$ and $\mathbf{D}^{(1)}(r_0)$ for the above spectrum as

$$\mathbf{D}(r_0) = \frac{(\langle E_{\bar{\nu}_e} \rangle - \langle E_{\nu_e} \rangle) \langle E_{\nu_x} \rangle}{\langle E_{\nu_e} \rangle \langle E_{\nu_x} \rangle + \langle E_{\bar{\nu}_e} \rangle (4\langle E_{\nu_e} \rangle + \langle E_{\nu_x} \rangle)} \mathbf{e}_e = \frac{1}{11} \mathbf{e}_e, \quad (4.7)$$

$$\mathbf{S}(r_0) = \frac{(\langle E_{\nu_e} \rangle + \langle E_{\bar{\nu}_e} \rangle) \langle E_{\nu_x} \rangle - 2\langle E_{\nu_e} \rangle \langle E_{\bar{\nu}_e} \rangle}{(\langle E_{\nu_e} \rangle + \langle E_{\bar{\nu}_e} \rangle) \langle E_{\nu_x} \rangle + 4\langle E_{\nu_e} \rangle \langle E_{\bar{\nu}_e} \rangle} \mathbf{e}_e = \frac{2}{11} \mathbf{e}_e, \quad (4.8)$$

$$\mathbf{D}^{(1)}(r_0) = \frac{2\Delta m_{13}^2}{3} \frac{1/\langle E_{\nu_e} \rangle^2 + 1/\langle E_{\bar{\nu}_e} \rangle^2 - 2/\langle E_{\nu_x} \rangle^2}{1/\langle E_{\nu_e} \rangle + 1/\langle E_{\bar{\nu}_e} \rangle + 4/\langle E_{\nu_x} \rangle} \mathbf{e}_e = 0.215 \mathbf{e}_e \text{ km}^{-1}. \quad (4.9)$$

Using the above expressions, $\langle \omega \rangle \equiv \mathbf{D} \cdot \mathbf{D}^{(1)} / |\mathbf{D}|^2$ is calculated to be

$$\langle \omega \rangle = 2.37 \text{ km}^{-1}, \quad (4.10)$$

which allows us to write $\langle \omega^{ey} \rangle = \langle \omega \rangle$ and $\langle \omega^{ex} \rangle = \epsilon \langle \omega \rangle$ in terms of $\langle \omega \rangle$, as per Eq. (3.68). This sets the ‘‘scale’’ for the problem. When $\mu \gg \langle \omega \rangle$, we have synchronized oscillations, when $\mu \gtrsim \langle \omega \rangle$ we have bipolar oscillations, as μ becomes less than $\langle \omega \rangle$ spectral splits develop. Then as $\lambda = \omega$, we have the MSW resonances. All of these happen for both the H ($\nu_e - \nu_y$) and the L ($\nu_e - \nu_x$) sector. Knowing $\mu(r)$ and $\lambda(r)$ we can predict the radii r at which various flavor conversions take place.

We expect synchronized oscillations in the region where $\mu > 4\langle \omega^{ey} \rangle S_3^{ey} / (D_3^{ey})^2 \approx 208 \text{ km}^{-1}$ [76], which corresponds to $r_{\text{syn}}^{ey} \approx 30 \text{ km}$ in our example. In the further region till $\mu \approx \langle \omega^{ey} \rangle / D_3^{ey} \approx 26 \text{ km}^{-1}$ [76], which corresponds to $r_{\text{bip}}^{ey} \approx 49 \text{ km}$, $\nu_e \leftrightarrow \nu_y$ bipolar oscillations are expected. Beyond this region the spectral split in the $e - y$ sector should develop, and subsequently MSW resonances should take place, which would be either completely adiabatic (large θ_{13}) or completely non-adiabatic (small θ_{13}) for the values of θ_{13} we consider. Similarly we calculate for the $e - x$ flavors, the relevant values of $r_{\text{syn}}^{ex} \sim 68 \text{ km}$ and $r_{\text{bip}}^{ex} \sim 114 \text{ km}$ for approximate boundaries of synchronized and bipolar oscillations in the $e - x$ sector. However, no bipolar oscillations take place in the $e - x$ sector since the corresponding hierarchy is

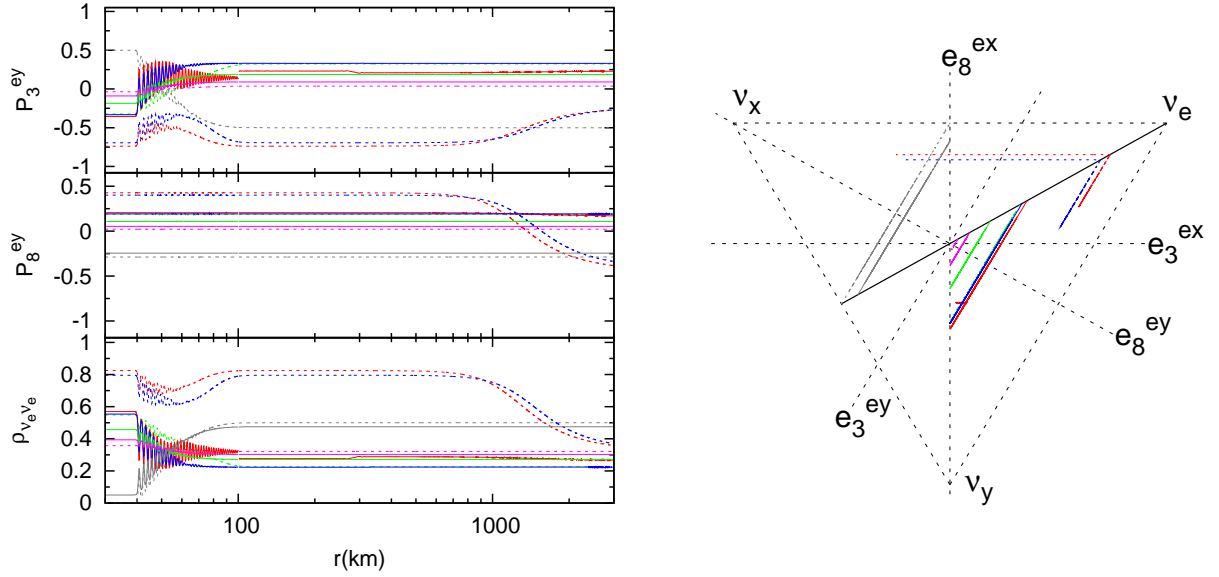


Figure 4.2: The flavor evolution of representative energy modes of ν_e (dotted) and $\bar{\nu}_e$ (undotted) for the density profile in Fig. 4.1, with $\theta_{13} = 0.001$. In the $\rho_{\nu_e \nu_e}$ plot, the energy of neutrinos as well as antineutrinos increases top downwards. The energies (in MeV) of the modes, shown in the figure, are 2.5 (Red), 3.6 (Blue), 9.4 (Green), 13.3 (Pink) and 50.0 (Grey). In the triangle plot, the bold line passing through ν_e is where all the neutrino and antineutrino states initially lie.

normal. In Fig. 4.1, we show the positions corresponding to r_{syn}^{ey} , r_{bip}^{ey} , r_{syn}^{ex} and r_{bip}^{ex} .

4.2.1 Small θ_{13}

Fig. 4.2 shows the flavor evolutions in terms of P_3^{ey} , P_8^{ey} and the \mathbf{e}_3 – \mathbf{e}_8 triangle for neutrinos as well as antineutrinos, for $\theta_{13} = 0.001$. This small value of θ_{13} ensures that the MSW resonance H in antineutrinos is nonadiabatic, so that the effects of this resonance are not felt. One can then clearly identify the nonlinear effects. We make the following observations and interpretations based on the figure:

- All the neutrinos and antineutrinos initially lie on a line passing through ν_e in the \mathbf{e}_3 – \mathbf{e}_8 triangle. This is because the initial conditions are taken to be symmetric in ν_x and ν_y .
- The flavor evolution starts only at $r = 40$ km, which is slightly beyond r_{syn}^{ey} . Before this point, the oscillations are synchronized, with a vanishing amplitude since $\lambda \gg \langle \omega^{ey} \rangle$.

- Between $r = 40$ and 60 km, $\nu_e \leftrightarrow \nu_y$ bipolar oscillations are observed as rapid dips in P_3^{ey} , and consequently in $\rho_{\nu_e\nu_e}$. These oscillations vanish when $r \gtrsim r_{bip}^{ey}$.
- Around $r \approx 60$ km, a spectral split develops in neutrinos along P_3^{ey} . The spectral split tends to keep the low energy neutrinos at their original position, while taking the high energy neutrinos as well as almost all antineutrinos towards $P_3^{ex} = 0$.³
- Between $r \approx 100 - 1000$ km, antineutrinos of different energies undergo the H resonance. However the resonance is highly nonadiabatic and does not cause any flavor conversion.
- At $r = 1000$ km and beyond, the effects of the MSW resonance L come into play, resulting in $\nu_e \leftrightarrow \nu_x$ conversion. Since the high energy neutrinos are already close to $P_3^{ex} = 0$, there is effectively no flavor conversion. However the low energy neutrinos tend to convert to ν_x , which is seen as a movement parallel to the $\nu_e - \nu_x$ edge in the $\mathbf{e}_3 - \mathbf{e}_8$ triangle.
- Since all the flavor conversions can be understood as a net effect of two-flavor phenomena taking place in well-separated regions in the star, the flavor transitions in the $\mathbf{e}_3 - \mathbf{e}_8$ triangle are always parallel to the $\nu_e - \nu_x$ edge or $\nu_e - \nu_y$ edge.

Thus, for a small θ_{13} , the nonlinear effects can be clearly identified, whereas the effects due to the H resonance are absent. We calculate the flavor evolution till $r = 5000$ km. The nonlinear effects have almost vanished by this time. Further MSW resonances due to the shock wave [21, 34, 35, 36, 37, 38, 39, 40, 41, 42, 43, 44], as well as possible effects of stochastic density fluctuations or turbulence [45, 46, 47] will govern flavor conversions here onwards. Our calculations thus provide initial conditions for neutrino spectra at this point.

In Fig. 4.3, we show the neutrino and antineutrino spectra at $r = 5000$ km. We see that ν_e with $E \gtrsim 7$ MeV convert almost completely to ν_y due to the spectral

³ There seems to be a spectral split in antineutrinos as well, at very low energies. This is similar to the observation in [76], and may be the effect of multiple-crossing of the spectra.

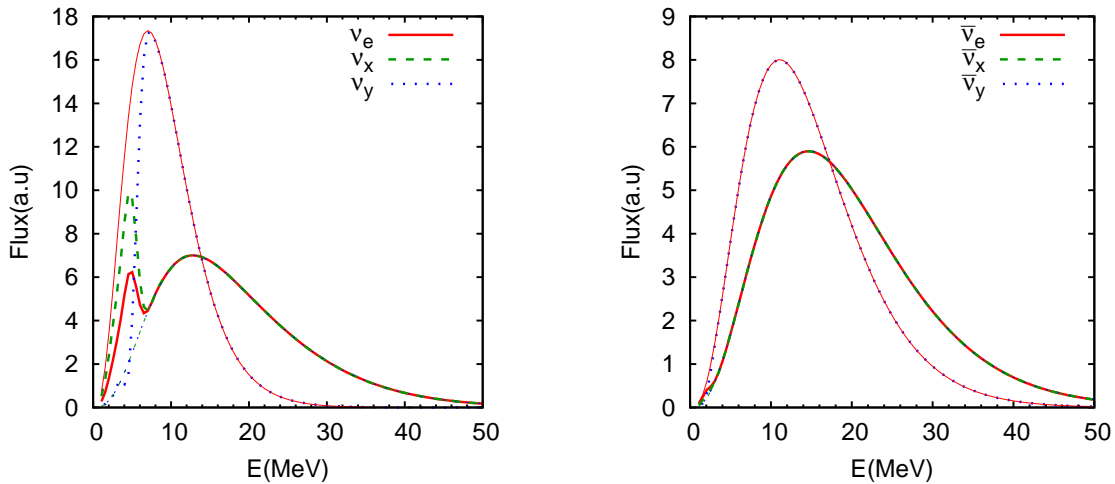


Figure 4.3: Neutrino and antineutrino spectra at $r = 5000$ km for $\theta_{13} = 0.001$. The e , x and y flavors are shown in red(solid), green(dashes) and blue(dots). The thin lines/dashes/dots are for initial spectra and thick ones for the final spectra. The ν_e and ν_y spectra get swapped for $E \gtrsim 7$ MeV, whereas the lower energy ν_e spectrum partially mixes with ν_x . In the antineutrino sector, the $\bar{\nu}_e$ and $\bar{\nu}_y$ spectra are almost completely swapped, while the $\bar{\nu}_x$ spectrum remains unaffected.

split, whereas lower energy ν_e convert partially to ν_x at the L resonance. In the antineutrino sector, the $\bar{\nu}_e$ and $\bar{\nu}_y$ spectra are almost all completely swapped due to the spectral split, while the $\bar{\nu}_x$ spectrum remains unaffected.

4.2.2 Large θ_{13}

At large θ_{13} values, the H resonance at $r \approx 100$ – 1000 km is adiabatic, and causes significant flavor conversions in antineutrinos. In Fig. 4.4, we show the flavor evolution for $\theta_{13} = 0.1$. While the signatures of synchronized and bipolar oscillations as well as the spectral split remain identical to the $\theta_{13} = 0.001$ case, the H resonance can be seen to change the antineutrino picture substantially. The conversions in the neutrino sector, on the other hand, are identical to the small θ_{13} case. The following observations can be made from the figure.

- The spectral split gives rise to a complete $\bar{\nu}_e$ – $\bar{\nu}_y$ conversion, which takes antineutrinos to $P_3^{ex} = 0$.
- The H resonance again swaps the $\bar{\nu}_e$ – $\bar{\nu}_y$ spectra, thus undoing the earlier effect

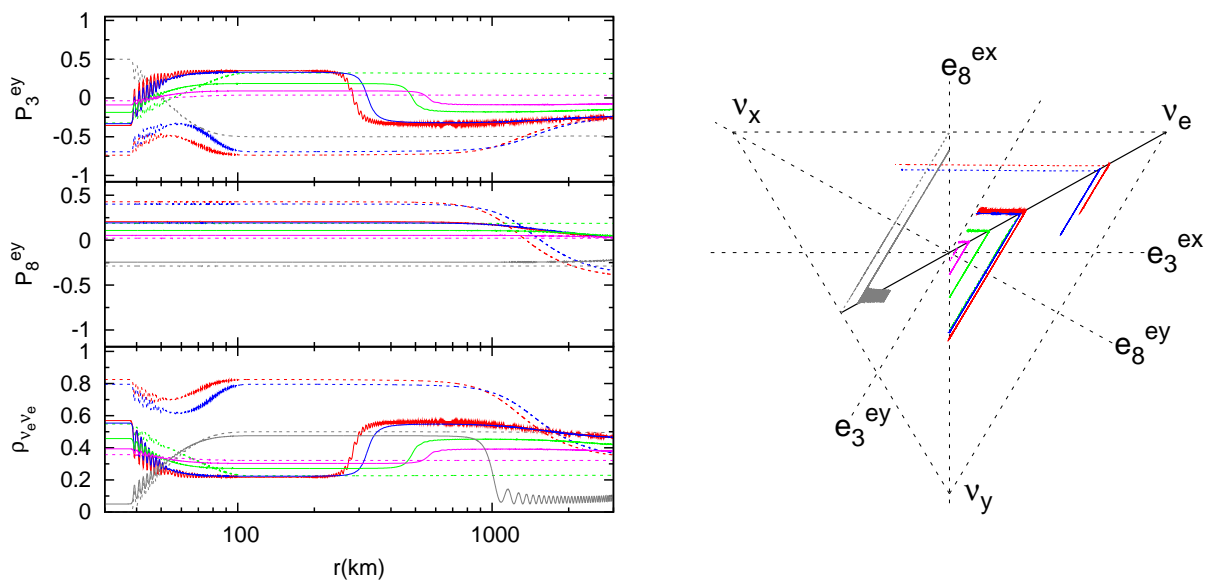


Figure 4.4: The flavor evolution of some representative energy modes of ν_e (dotted) and $\bar{\nu}_e$ (undotted) for the density profile in Fig. 4.1, with $\theta_{13} = 0.1$. The convention for the lines is the same as in Fig. 4.2.

of the spectral split. This takes the antineutrinos back to their starting position in the triangle.

- Antineutrinos are now not on the $P_3^{ex} = 0$ line as in the small θ_{13} case. As a result, the large value of θ_{12} causes substantial $\bar{\nu}_e - \bar{\nu}_x$ conversion as the neutrinos emerge from the L resonance region.

The neutrino and antineutrino spectra at $r = 5000$ km are shown in Fig. 4.5. We see that the neutrino spectra have the same characteristics as for small θ_{13} . In the antineutrino sector, complete $\bar{\nu}_e - \bar{\nu}_y$ spectral split and the reconversion at the H resonance cancel each other, whereas the large value of θ_{12} partially mixes the $\bar{\nu}_e - \bar{\nu}_x$ spectra.

The value of θ_{13} thus affects the $\bar{\nu}_e$ spectra substantially. At larger θ_{13} values, where the H resonance is more adiabatic, the $\bar{\nu}_e$ spectrum is softer. The $\bar{\nu}_x$ spectrum is also affected at large θ_{13} , as opposed to the small θ_{13} case.

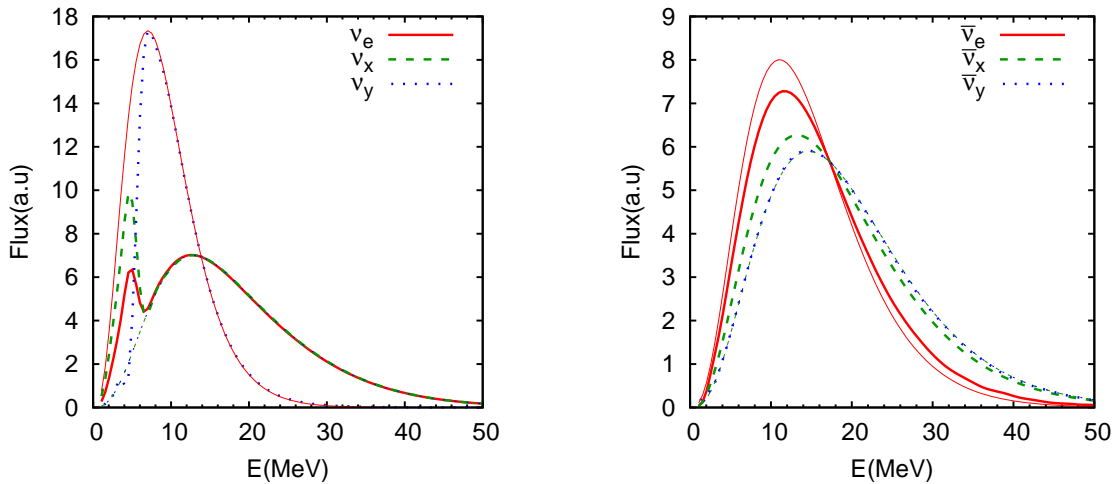


Figure 4.5: Neutrino and antineutrino spectra at $r = 5000$ km for $\theta_{13} = 0.1$. The e , x and y flavors are shown in red(solid), green(dashes) and blue(dots). The thin lines/dashes/dots are for initial spectra and thick ones for the final spectra. The ν_e and ν_y spectra get swapped for $E \gtrsim 7$ MeV, whereas the lower energy ν_e spectrum partially mixes with ν_x . In the antineutrino sector, the $\bar{\nu}_e$ and $\bar{\nu}_x$ spectra are partially mixed, while the $\bar{\nu}_y$ spectrum remains unaffected.

4.2.3 Summarized results

It is thus clear that the neutrino fluxes that reach Earth from a SN, are very different from the primary fluxes, even if MSW effects are unimportant. The nonlinear effects can themselves cause large flavor conversions. In particular for inverted hierarchy, we learn that the ν_e and ν_y spectra are exchanged above a certain split-energy E_c due to nonlinear effects. For antineutrinos the swap occurs over the complete spectrum. In the normal hierarchy, nonlinear effects do not have a significant effect. The MSW conversions cause further flavor conversions, and while the conversion probabilities have not changed from the traditional expectation, the primary fluxes entering the resonances are now vastly different. This leads to different flavor composition of the fluxes of neutrinos and antineutrinos arriving on Earth, than was traditionally expected.

These fluxes can be calculated using our understanding of nonlinear effects and the level-crossing diagrams. At the detectors on Earth one is typically sensitive to the ν_e and/or $\bar{\nu}_e$ flux, and so we summarize the expectations for these fluxes in Tables 4.1 and 4.2. The expressions in the table describe all the features of ν_e and

$\bar{\nu}_e$ spectra in Figs. 4.3 and 4.5. We have taken the L resonance to be adiabatic. In the case of multiple H resonances, as may occur during the shock wave propagation or turbulence, P_H may be taken to be the effective jump probability (it may have a nontrivial dependence on energy and time). Note that Earth matter effects are present only when $F_{\nu_e/\bar{\nu}_e}^{obs}$ is a nontrivial combination of $F_{\nu_e/\bar{\nu}_e}$ and $F_{\nu_x,\nu_y/\bar{\nu}_x,\bar{\nu}_y}$.

Normal hierarchy

$$F_{\nu_e}^{obs} = s_{12}^2 (P_H F_{\nu_e} + (1 - P_H) F_{\nu_y}) + c_{12}^2 F_{\nu_x}$$

$$F_{\bar{\nu}_e}^{obs} = c_{12}^2 F_{\bar{\nu}_e} + s_{12}^2 F_{\bar{\nu}_x}$$

Table 4.1: Neutrino and antineutrino fluxes in normal hierarchy arriving on Earth from a SN.

Inverted hierarchy

$$F_{\nu_e}^{obs} = \begin{cases} s_{12}^2 F_{\nu_e} + c_{12}^2 F_{\nu_x} & (E < E_c) \\ s_{12}^2 F_{\nu_y} + c_{12}^2 F_{\nu_x} & (E > E_c) \end{cases}$$

$$F_{\bar{\nu}_e}^{obs} = s_{12}^2 F_{\bar{\nu}_x} + c_{12}^2 ((1 - P_H) F_{\bar{\nu}_e} + P_H F_{\bar{\nu}_y})$$

Table 4.2: Neutrino and antineutrino fluxes in inverted hierarchy arriving on Earth from a SN.

These are the observable fluxes in terms of the primary fluxes for the scenario that we have considered. If the initial fluxes have the same ordering as in Eq. (1.16) but with slightly changed parameters, the outcome would be similar. However, if the initial fluxes have a different ordering, or if the nonlinear evolution is nonadiabatic the situation is likely to be different.

Chapter 5

Signatures of Nonlinear Supernova Neutrino Oscillations

The nonlinear flavor oscillations of SN neutrinos leave distinctive imprints on the neutrino spectra observable on Earth. In this chapter we discuss some possible outcomes for neutrino physics and astrophysics based on the papers: B. Dasgupta, A. Dighe and A. Mirizzi, “*Identifying neutrino mass hierarchy at extremely small θ_{13} through Earth matter effects in a supernova signal,*” Physical Review Letters **101** (2008) 171801, [arXiv:0802.1481 [hep-ph]] and B. Dasgupta, A. Dighe, A. Mirizzi and G. G. Raffelt, “*Spectral split in prompt supernova neutrino burst: Analytic three-flavor treatment,*” Physical Review D **77** (2008) 113007, [arXiv:0801.1660 [hep-ph]] respectively.

5.1 Determination of mass hierarchy using Earth matter effects

We have seen in the previous chapter that nonlinear effects have different outcomes for normal and inverted hierarchy. As a consequence, neutrino fluxes which are further processed by MSW matter effects are significantly different for the two hierarchies, even at extremely small θ_{13} values. This sensitivity presents a novel

possibility to determine the mass hierarchy at small θ_{13} . We propose a new method for determining the neutrino mass hierarchy, which works for extremely small values of θ_{13} using this possibility.

As before, we assume the hierarchy of number fluxes [23, 24]

$$\Phi_{\nu_e} > \Phi_{\bar{\nu}_e} > \Phi_{\nu_x} = \Phi_{\bar{\nu}_x} = \Phi_{\nu_y} = \Phi_{\bar{\nu}_y} . \quad (5.1)$$

Although it is not obvious that this hierarchy is maintained at late times, in the following we will assume it as our benchmark. We remark again that qualitatively different primary neutrino spectra and/or yet undiscovered flavor effects may yield different predictions for flavor conversion and the analysis will have to be repeated appropriately.

We concentrate on the $\bar{\nu}_e$ spectra observable through inverse beta decay reactions $\bar{\nu}_e + p \rightarrow n + e^+$ at water Cherenkov detectors. In inverted hierarchy, MSW matter effects in SN envelope are characterized in terms of the level-crossing probability P_H [34, 103] of antineutrinos, which is in general a function of the neutrino energy and θ_{13} . In the following, we consider two extreme limits, $P_H \simeq 0$ when $\sin^2 \theta_{13} \gtrsim 10^{-3}$ (“large”), and $P_H \simeq 1$ when $\sin^2 \theta_{13} \lesssim 10^{-5}$ (“small”).

While propagating through the Earth, the $\bar{\nu}_e$ and $\bar{\nu}_x$ spectra partially mix. The neutrino fluxes F_ν^{obs} at the Earth surface for normal hierarchy, as well as for inverted hierarchy with large θ_{13} , are given in terms of the the primary fluxes F_ν by

$$\begin{aligned} F_{\bar{\nu}_e}^{obs} &= \cos^2 \theta_{12} F_{\bar{\nu}_e} + \sin^2 \theta_{12} F_{\bar{\nu}_x} , \\ F_{\bar{\nu}_x}^{obs} &= \sin^2 \theta_{12} F_{\bar{\nu}_e} + \cos^2 \theta_{12} F_{\bar{\nu}_x} . \end{aligned} \quad (5.2)$$

For inverted hierarchy with small θ_{13} , we have

$$\begin{aligned} F_{\bar{\nu}_e}^{obs} &= \cos^2 \theta_{12} F_{\bar{\nu}_y} + \sin^2 \theta_{12} F_x^0 \approx F_x^0 , \\ F_{\bar{\nu}_x}^{obs} &= \sin^2 \theta_{12} F_{\bar{\nu}_y} + \cos^2 \theta_{12} F_{\bar{\nu}_x} \approx F_{\bar{\nu}_x} . \end{aligned} \quad (5.3)$$

Earth effect can be taken into account by just mapping $\cos^2 \theta_{12} \rightarrow P(\bar{\nu}_1 \rightarrow \bar{\nu}_e)$ and $\sin^2 \theta_{12} \rightarrow 1 - P(\bar{\nu}_1 \rightarrow \bar{\nu}_e)$, where $P(\bar{\nu}_1 \rightarrow \bar{\nu}_e)$ is the probability that a state entering the Earth as mass eigenstate $\bar{\nu}_1$ is detected as $\bar{\nu}_e$ at the detector.

From Eqs. (5.2) and (5.3), one expects to observe Earth matter effect in normal hierarchy independently of θ_{13} , while in inverted hierarchy it is expected only at large θ_{13} . For small θ_{13} and inverted hierarchy, the $\bar{\nu}_e$ spectrum arriving at the Earth is identical to the $\bar{\nu}_x$ spectrum arriving at the Earth, so any oscillation effect among them is unobservable. This implies that if next generation neutrino experiments bound θ_{13} to be small, from the (non)observation of Earth matter effect we could identify the neutrino mass hierarchy.

A strategy to observe Earth matter signatures in neutrino oscillations is to compare the signal at two detectors. The difference between the $\bar{\nu}_e$ flux $F_{\bar{\nu}_e}^A$ at a shadowed detector and the $\bar{\nu}_e$ flux $F_{\bar{\nu}_e}^B$ at a detector that is not shadowed by the Earth can be written as

$$\Delta F = F_{\bar{\nu}_e}^A - F_{\bar{\nu}_e}^B = f_{\text{reg}}(F_{\bar{\nu}_e} - F_{\bar{\nu}_x}) , \quad (5.4)$$

for normal hierarchy as well as for inverted hierarchy with large θ_{13} . Here $f_{\text{reg}} = P(\bar{\nu}_1 \rightarrow \bar{\nu}_e) - \cos^2 \theta_{12}$ is the Earth regeneration factor. In inverted hierarchy for small θ_{13} , we get $\Delta F = 0$. If the $\bar{\nu}$ trajectories cross only the Earth mantle, characterized by an approximately constant density, f_{reg} is simply given by [104]

$$f_{\text{reg}} = -\sin 2\tilde{\theta}_{12} \sin(2\tilde{\theta}_{12} - 2\theta_{12}) \sin^2 \left(\frac{\Delta\tilde{m}_{\odot}^2 L}{4E} \right) , \quad (5.5)$$

where $\tilde{\theta}_{12}$ is the effective value of the antineutrino mixing angle θ_{12} in matter, $\Delta\tilde{m}_{\odot}^2$ is the solar mass squared difference in matter, and L is the path length in Earth. In Earth matter, we have $\sin 2\tilde{\theta}_{12} > 0$ and $\sin(2\tilde{\theta}_{12} - 2\theta_{12}) < 0$, which tells us that $f_{\text{reg}} \geq 0$.

The flavor dependent primary neutrino spectra $F_{\nu_\alpha}(E)$ in terms of $\langle E \rangle_{\nu_\alpha}$ is the average energy for the different neutrino species, and ξ_{ν_α} is the spectral pinching

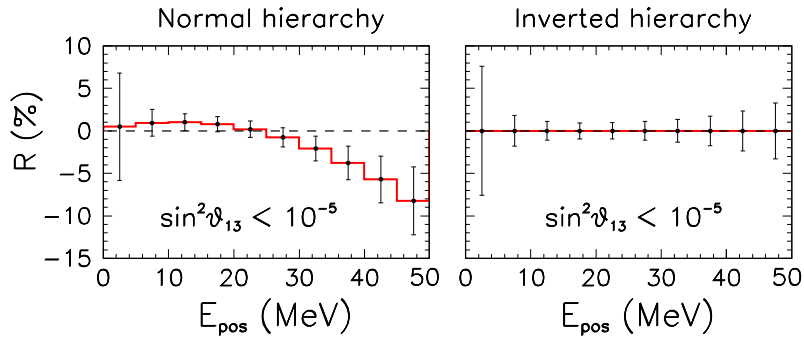


Figure 5.1: Plot of the ratio R defined in Eq. 5.7, as a function of the observable positron energy for normal hierarchy (left panel) and inverted hierarchy (right panel), with $\sin^2 \theta_{13} \lesssim 10^{-5}$. For $\sin^2 \theta_{13} \gtrsim 10^{-3}$, the ratio R will be identical to the left panel for either hierarchy.

parameter. The neutrino flux at the neutrinosphere can then be estimated to be

$$F_{\nu_\alpha} = \frac{L_{\nu_\alpha}}{\langle E_{\nu_\alpha} \rangle} f_{\nu_\alpha}(E) , \quad (5.6)$$

where L_{ν_α} is the luminosity in the ν_α flavor and $f_{\nu_\alpha}(E)$ is the distribution function in Eq.(4.1). All SN models robustly predict $\langle E_{\bar{\nu}_e} \rangle < \langle E_{\bar{\nu}_x} \rangle \approx \langle E_{\bar{\nu}_y} \rangle$, as well as $\xi_{\alpha\bar{\nu}_e} \approx \xi_{\alpha\bar{\nu}_x} \approx \xi_{\alpha\bar{\nu}_y}$. This implies that the sign of $(F_{\bar{\nu}_e}^0 - F_{\bar{\nu}_x}^0)$ is positive at low energies (before the crossing of the $\bar{\nu}_e$ and $\bar{\nu}_x$ spectra) and negative at higher energies.

The net result is that when we compare the antineutrino fluxes between a shadowed and an unshadowed detector, we will have $\Delta F > 0$ at low energies and $\Delta F < 0$ at high energies in the case of normal mass hierarchy, or in inverted mass hierarchy with large θ_{13} . In inverted hierarchy with small θ_{13} , one expects a ΔF compatible with zero.

To illustrate the above, we consider a galactic supernova explosion at a distance of 10 kpc, with luminosities $L_{\bar{\nu}_x} = L_{\bar{\nu}_y} = 0.8L_{\bar{\nu}_e}$ and total emitted energy $E_b = 3 \times 10^{53}$ erg. We also choose $\langle E_{\bar{\nu}_e} \rangle = 15$ MeV, $\langle E_{\bar{\nu}_x} \rangle = \langle E_{\bar{\nu}_y} \rangle = 18$ MeV, and $\nu_\alpha = 3$, inspired by the results of the Garching simulations [24, 105]. We analyze the detection of the above signal using two large water Cherenkov detectors A and B of fiducial mass 0.4 megaton each, as proposed for upcoming experiments [106, 107, 108]. We compare the number of events in detector A , where neutrinos arrive after

traversing $L = 8000$ km in Earth mantle with an approximately constant density $\rho = 4.5$ g/cm³, with another detector B for which the supernova is not shadowed by the Earth ($L = 0$). The reference values for features of the detectors, e.g., energy resolution and interaction cross sections, are the same as in [42]. We choose $\Delta m_{\odot}^2 = 8 \times 10^{-5}$ eV² and $\sin^2 \theta_{12} = 0.29$ as the oscillation parameters relevant for the Earth matter effect.

We define

$$R \equiv (N_A - N_B)/N_B \quad (5.7)$$

as the difference between the number of $\bar{\nu}_e$ events at the shadowed detector and the unshadowed detector, normalized to the number of events at the unshadowed detector. In Fig. 5.1, we plot the ratio R as a function of the measured positron energy E_{pos} for $\bar{\nu}_e$ in normal hierarchy (left panel) and inverted hierarchy (right panel) for $\sin^2 \theta_{13} \lesssim 10^{-5}$. The error bars show the statistical error in R . In the other extreme case of $\sin^2 \theta_{13} \gtrsim 10^{-3}$, both the normal and inverted hierarchy would correspond to the left panel.

Let us consider the scenario where θ_{13} is known to be small. From the figure, in normal hierarchy the ratio R is positive for $E_{\text{pos}} \lesssim 25$ MeV and negative at higher energy. The low energy spectrum is dominated by statistical error, but for $E_{\text{pos}} \gtrsim 30$ MeV the depletion of the signal with respect to the unshadowed detector is clearly visible, with $|R| \gtrsim 5\%$. On the other hand, in inverted hierarchy we find $R = 0$. The difference in the predictions of two hierarchies is significant and should be observable. Primary spectra taken from Livermore simulations [23], which predict a larger difference between $\bar{\nu}_e$ and $\bar{\nu}_x$ average energies, would show a more pronounced Earth effect. We emphasize that our method is based on a model independent signature which does not rely on fitting or extracting any parameters.

The comparison of the neutrino signal in two detectors is also possible using only a single megaton class water Cherenkov detector together with the km³ ice Cherenkov detector IceCube at the South Pole [109]. Even though IceCube cannot reconstruct the neutrino spectrum at SN energies, the ratio of luminosities at these two detectors can be determined rather accurately, which will show about 5% time variation if

Earth effect is indeed present [36]. Moreover, if a large scintillator detector [106] is built, its superior energy resolution would allow the observation of the modulations induced by the earth effect in the spectrum, without the need to compare the signal with another unshadowed detector [37].

The swap of the $\bar{\nu}$ spectra due to nonlinear effects does not depend on the exact neutrino density profile as long as the propagation is adiabatic [62], whose validity we have checked for typical SN profiles and θ_{13} as low as 10^{-10} . Decoherence effects are highly suppressed due to the $\nu_e\text{-}\bar{\nu}_e$ flux asymmetry [75], and other multi-angle effects also do not affect the net antineutrino conversions substantially [76]. Moreover, with an extremely small θ_{13} , the detailed matter density profile near the H resonance is immaterial, and the effects of density fluctuations or turbulence may safely be ignored. Therefore, one can make the following statements: (i) Observation of Earth matter effects cannot be explained in inverted hierarchy (ii) Nonobservation of Earth matter effects cannot be explained in normal hierarchy (unless the primary fluxes are almost identical). Our proposed method is thus quite robust, and would be able to identify the mass hierarchy. It is not only competitive with the long baseline strategy proposed in [110], but also offers an independent astrophysical resolution to the hierarchy determination problem.

If θ_{13} is known to be large, the hierarchy can be determined through a number of other observables in the SN burst itself: signatures of SN shock-wave propagation in the $\bar{\nu}_e$ signal [21, 42, 45], the ν_e signal during the neutronization burst [111], or the direct, albeit extremely challenging, observation of the spectral split in ν_e spectrum [84] at a large liquid Argon detector [112]. In fact the hierarchy may even be identified at the long baseline experiments. However in such a scenario, the Earth matter effects act as an evidence for nonlinear flavor conversions, thus giving us confidence about our understanding of the processes happening in the core of the star.

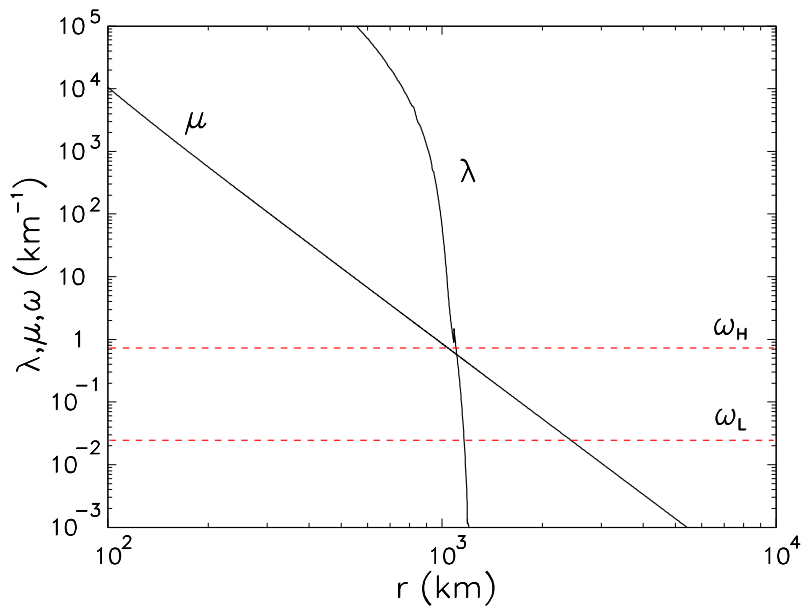


Figure 5.2: Profile of the matter potential λ and the effective neutrino potential μ for an O-Ne-Mg core collapse SN [14, 113, 114, 115].

5.2 Progenitor dependence of SN neutronization burst signal

An interesting new case is motivated by the class of O-Ne-Mg core-collapse supernovae [14, 113, 114, 115]. Supernovae with the lowest progenitor masses of $(8-10) M_{\odot}$, encompassing perhaps 30% of all cases, collapse even before forming an iron core. In state-of-the-art numerical simulations these supernovae explode even in a spherically symmetric treatment, largely because their envelope mass is very small. By the same token, the matter density profile above the core is very steep even at the time of core bounce. In this case the H and L level crossings occur very close to the neutrino sphere and may well lie deeply within the region where nonlinear effects are important. This is illustrated in Fig. 5.2 where we show $\lambda(r) = \sqrt{2}G_{\text{F}}n_e(r)$ of an O-Ne-Mg core progenitor star [14, 113, 114]. We also show $\omega^H = \langle \Delta m_{\text{atm}}^2 / 2E \rangle$ and $\omega^L = \langle \Delta m_{\odot}^2 / 2E \rangle$ as horizontal lines, where the average is over the Fermi-Dirac spectrum of neutrino energies described below. The intersection of $\lambda(r)$ with these lines indicates the locations of the H and L level crossings.

In Fig. 5.2 we also show the effective neutrino potential $\mu = \sqrt{2}G_{\text{F}}F_{\nu_e} \langle 1 - \cos \theta \rangle_{\text{eff}}$,

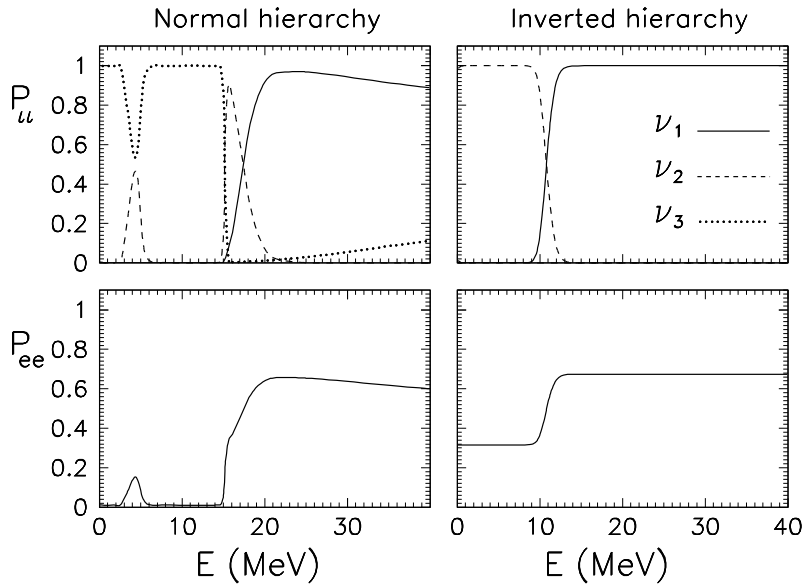


Figure 5.3: Mass eigenstate fractions P_{ii} as well as the ν_e survival probabilities far away from the star, numerically computed using the SN model of Fig. 5.2 and an initial flux of pure ν_e .

where θ is the angle between different neutrino trajectories and $\langle \dots \rangle_{eff}$ stands for a suitable average. At large distances, μ scales approximately as r^{-4} . nonlinear neutrino effects driven by Δm_{atm}^2 are important for $\mu(r) \gtrsim \omega_H$ and driven by Δm_{\odot}^2 for $\mu(r) \gtrsim \omega_L$.

Duan et al. [86] have shown that in this case the interplay of ordinary MSW conversions with nonlinear oscillations leads to interesting effects. We start with a pure ν_e flux with a Fermi-Dirac spectrum ($\langle E_{\nu_e} \rangle = 11$ MeV, degeneracy parameter $\eta = 3$), and numerically calculate the mass eigenstate fractions P_{ii} and the ν_e survival probabilities P_{ee} far away from the star, as shown in Fig. 5.3. Our results are in qualitative agreement with Fig. 2 of [86]. However, our P_{ee} is constructed as an incoherent sum of the mass fractions, thus representing the physical situation far away from the star, where the oscillatory features seen in Duan et al.'s P_{ee} have disappeared.

In inverted hierarchy, one observes that the neutrinos emerging from the star are in the ν_2 state at low energies and in the ν_1 state at high energies, with the transition taking place around $E \approx 12$ MeV. This results in a step function in energy for P_{ee} .

In the normal hierarchy, the neutrinos emerging from the star are in ν_1 state for $E \gtrsim 17$ MeV, in ν_2 state for $15 \text{ MeV} \lesssim E \lesssim 17$ MeV, and in the ν_3 state for $E \lesssim 15$ MeV. The bump seen around 5 MeV is due to an abrupt change in the matter density profile used for the computation (see [86] for details), and we do not address it here. The transition at $E \approx 15$ MeV is rather sharp, however the one at $E \approx 17$ MeV is not as abrupt. This results in a two-step function for P_{ee} , with the step at $E \approx 17$ MeV somewhat smoothed out.

This is an example of a “MSW prepared spectral split” as shown in Sec. 3.5.4, i.e. first the synchronized MSW resonances take place and generate off-diagonal terms in the density matrix, and then the splits develop in the usual way. In a three-flavor treatment, the step-like feature actually consists of two narrowly spaced splits for the normal hierarchy and a single split for the inverted hierarchy.

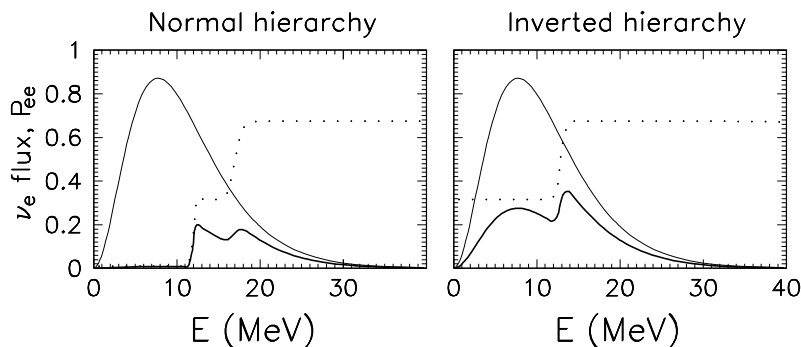


Figure 5.4: Initial (thin) and final (thick) spectrum for a Fermi-Dirac distribution with the typical parameters. The numerical final spectrum is for our toy-model supernova where the MSW crossings and spectral-split region are far separated. Dotted curves represent the survival probability P_{ee} for electron neutrinos.

In Fig. 5.3 we show the above-mentioned features of the neutrino spectrum for the neutronization burst of a O-Ne-Mg supernova. This signal is quite different from the neutronization burst signal expected from an iron-core supernova, where there are no such splits in the neutrino spectrum in either hierarchy.

To detect this signal one needs a detector that is sensitive to ν_e , e.g. liquid Argon detectors. With detectors at present, we do not have enough events to identify the spectra, and the only difference would manifest in the form of a depletion of the number of events even for both normal and inverted hierarchy. This signal is

degenerate with the signal from an iron core supernova for normal hierarchy and large θ_{13} , where ν_e undergo an adiabatic MSW resonance leading to a flux depletion. This is ground for dangerous confusion.

However, if we have a larger detector that gathers enough events and has enough energy resolution to be able to see the splits, we speculate that this may be useful for distinguishing the supernova progenitor using neutrinos and allow for better characterization of different types of supernovae.

Chapter 6

Impact on the Diffuse Supernova Neutrino Background

In this chapter, we look at the impact of nonlinear oscillations on the flux of neutrinos from all past SN. We find that depending on the hierarchy and the mixing scenario the fluxes can change by up to 50% due to nonlinear effects alone. Although there are large astrophysical uncertainties, this strong dependence can in principle be very useful to rule out some scenarios if we measure the diffuse supernova neutrino background flux. This chapter is based on the paper: S. Chakraborty, S. Choubey, B. Dasgupta and K. Kar, “*Effect of Collective Flavor Oscillations on the Diffuse Supernova Neutrino Background,*” *Journal of Cosmology and Astroparticle Physics* **09** (2008) 013, [arXiv:0805.3131 [hep-ph]].”

6.1 Diffuse SN neutrino background

Supernovae are relatively rare events in our galaxy. It is estimated that in galaxies similar to ours they occur at a rate of about 1 to 3 per century [27], which prompts consideration of the alternative strategy to detect neutrinos from supernovae that are further away. Neutrinos accumulated in the Universe from all the SN explosions in the past and present epoch form a cosmic background, known as the diffuse supernova neutrino background (DSNB) or supernova relic neutrinos [29, 30].

The expected flux of these DSNB neutrinos depends mainly on the SN rate and the “typical” flavor dependent flux of neutrinos from supernovae.

Estimation of the DSNB flux has been performed in previous literature [116], focussing on DSNB detection via $\bar{\nu}_e$ scattering off protons at water Cherenkov detectors [117] and large liquid scintillator detectors [118]. On the other hand, ν_e detection has been considered at a liquid argon detector [119] and at Sudbury Neutrino Observatory (SNO) [120, 121]. In [122], authors have performed a detailed comparative study of ν_e detection in different future large scale observatories – by interaction of ν_e on oxygen in water Cherenkov detectors, on carbon in liquid scintillator detectors and on argon in liquid argon detectors. Experimentally, the best upper limits at 90 % C.L. of $6.8 \times 10^3 \nu_e \text{ cm}^{-2}\text{s}^{-1}$ ($25 \text{ MeV} < E_{\nu_e} < 50 \text{ MeV}$) and $1.2 \bar{\nu}_e \text{ cm}^{-2}\text{s}^{-1}$ ($E_{\bar{\nu}_e} > 19.3 \text{ MeV}$) come from the Liquid Scintillation Detector (LSD) [123] and the Super-Kamiokande (SK) detectors [32] respectively. However, stronger bounds can be placed on these fluxes, albeit using somewhat indirect arguments [121, 124]. Some of the theoretical estimates of the DSNB fluxes predict event-rates for $\bar{\nu}_e$ that are tantalizingly close to detection, *e.g.*, the observational upper limit set by the SK collaboration [32]. The prospects for discovery thus seem promising if a large water Cherenkov detector like SK is loaded with 0.02% GdCl_3 [125] or if one or more of the proposed next generation detectors become available.

With the inclusion of nonlinear effects, the observable spectra gets modified. The expected DSNB flux in the case of inverted hierarchy turns out to be quite different from those contained in previous works that disregarded nonlinear effects. Thus the prospects of DSNB detection at antineutrino and/or neutrino detectors are changed.

6.2 Estimation of DSNB flux

The total differential DSNB flux arriving at terrestrial detectors, expressed as the number of neutrinos of flavor ν_α arriving per unit area per unit time per unit energy, due to all supernovae in the Universe up to a maximum redshift z_{max} (assumed to

be 7 for the numerical analysis), is

$$F_{\nu_\alpha}^{obs}(E_{\nu_\alpha}) = \frac{1}{H_0} \int_0^{Z_{max}} R_{SN}(z) F_{\nu_\alpha}((1+z)E_\nu) \frac{dz}{\sqrt{(\Omega_m(1+z)^3 + \Omega_\Lambda)}} . \quad (6.1)$$

Here F_{ν_α} is the neutrino spectra emitted by a SN, E_{ν_α} is the neutrino energy at Earth and $R_{SN}(z)$ is the SN rate per comoving volume at redshift z . Note that the factor $(1+z)$ in the neutrino spectrum $F_{\nu_\alpha}((1+z)E_\nu)$ incorporates the redshift of the energy spectrum. The cosmological parameters are assumed to be given by the standard Λ -CDM cosmology, we have

$$\Omega_m = 0.3 ; \Omega_\Lambda = 0.7 \text{ and } H_0 = 70 h_{70} \text{ km s}^{-1} \text{ Mpc}^{-1} . \quad (6.2)$$

Therefore, we only need to know the SN rate $R_{SN}(z)$ and the differential flux of neutrinos $F_\nu(E_\nu)$, from a typical core-collapse event to calculate the DSNB flux at Earth.

The SN rate $R_{SN}(z)$ is related to $R_{SF}(z)$, through the initial mass function $\varphi(m)$, which describes the differential mass distribution of stars at formation [116, 126]. We assume that all stars that are more massive than $8M_\odot$ give rise to core-collapse events and die on a timescale much shorter than the Hubble time, and that the initial mass function $\varphi(m)$ is independent of redshift. This allows us to relate the star formation rate $R_{SF}(z)$ to the cosmic SN rate $R_{SN}(z)$ as

$$R_{SN}(z) = R_{SF}(z) \frac{\int_{8M_\odot}^{125M_\odot} \varphi(m) dm}{\int_{0.1M_\odot}^{125M_\odot} \varphi(m) m dm} . \quad (6.3)$$

For our estimates, we use the initial mass function from [127], i.e.

$$\varphi(m) \propto \begin{cases} m^{-2.15} & (m > 0.5M_\odot) \\ m^{-1.50} & (0.1M_\odot < m < 0.5M_\odot) \end{cases} . \quad (6.4)$$

Putting the above expression into Eq. (6.3) we find

$$R_{SN}(z) = 0.0132 R_{SF}(z) M_\odot^{-1} . \quad (6.5)$$

It should be noted that the factor connecting R_{SN} and R_{SF} is quite insensitive to the upper limit of the integrations in Eq. (6.3).

Recent careful studies on different indicators of the cosmic star formation rate have been used to calculate the R_{SF} and its normalization. We use the cosmic star formation rate per comoving volume, R_{SF} , from the concordance model advocated in [128, 129], which is given by

$$R_{SF}(z) \propto \begin{cases} (1+z)^{3.44} & z < 0.97 \\ (1+z)^{-0.26} & 0.97 < z < 4.48 \\ (1+z)^{-7.8} & 4.48 < z \end{cases} , \quad (6.6)$$

with the normalization

$$R_{SF}(0) = 0.0197 M_{\odot} \text{yr}^{-1} \text{Mpc}^{-3} . \quad (6.7)$$

This model satisfies the experimental upper limit on DSNB set by SK [32], and is known as the concordance model [126].

We do not know the typical SN neutrino flux accurately, so to estimate the impact of nonlinear effects, we consider an initial spectra with luminosities $L_{\bar{\nu}_x} = L_{\bar{\nu}_y} = 0.5L_{\bar{\nu}_e}$ and $L_{\nu_x} = L_{\nu_y} = 0.625L_{\bar{\nu}_e}$ and total emitted energy $E_b = 3 \times 10^{53}$ erg. We also choose $\langle E \rangle_{\nu_e} = 12$, $\langle E \rangle_{\bar{\nu}_e} = 15$ MeV, $\langle E \rangle_{\bar{\nu}_x, \nu_x} = \langle E \rangle_{\bar{\nu}_y, \nu_y} = 18$ MeV and $\alpha = 3$.

6.3 Expected event rate at detectors

An array of existing and planned detectors could observe the DSNB neutrinos. We consider in particular water Cherenkov detectors (Super-K, Hyper-K) for the antineutrinos. We also consider their enhanced versions with Gadolinium enrichment, leading to efficient neutron tagging and background rejection. We use the standard energy-cuts used for the analysis, so as to avoid the solar neutrinos below 10 MeV and the atmospheric neutrinos above 20 MeV. For detecting the ν_e DSNB, the best option seems to a reasonably large Liquid argon detector. We show the expected

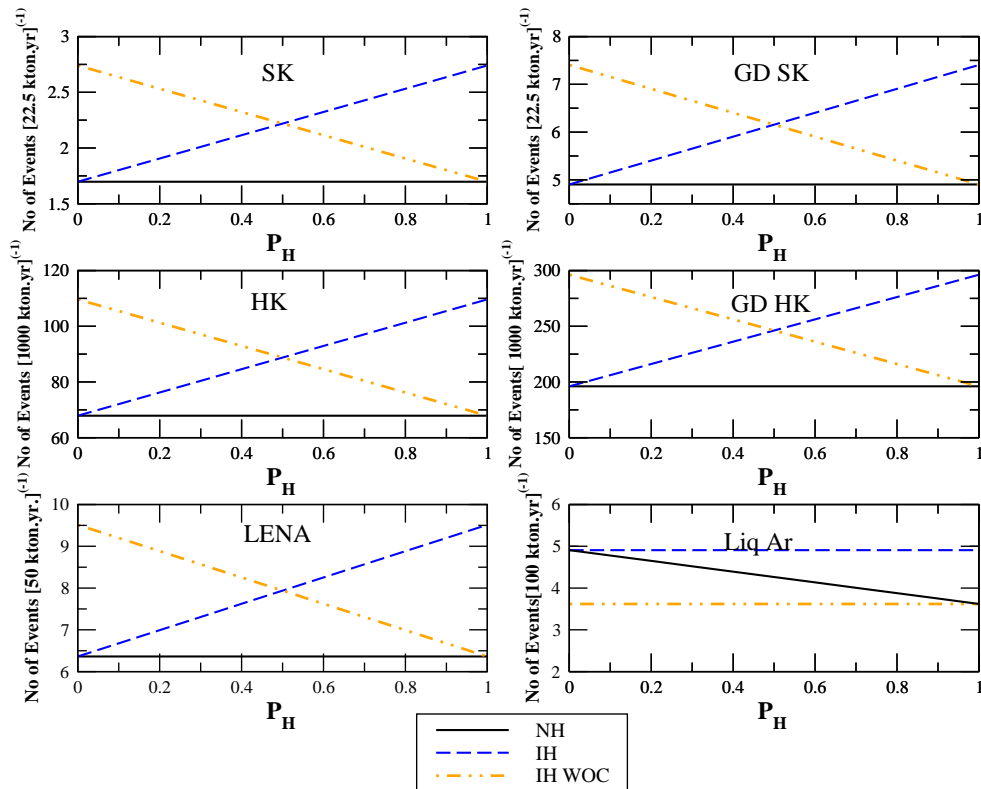


Figure 6.1: Number of expected events as a function of the jump probability P_H between the mass eigenstates ν_1 and ν_3 . Black lines are for normal hierarchy and blue dashed lines for inverted hierarchy. The yellow dashed dotted lines show the case for inverted hierarchy without the nonlinear collective effects (WOC). The label “Gd” denotes availability of Gadolinium tagging in the detector.

event rates in Fig. 6.1.

We find that the event rate can be different from previous estimates (WOC) by up to 50%, and depends on the value of θ_{13} . It is generically true for any choice of primary fluxes. This result will have impact on models of stellar evolution if the DSNB gets detected. In particular, knowing θ_{13} and hierarchy, we will be able to put experimental constraints that those models must satisfy. Again, we remind that this result is only indicative, and the analysis will have to be repeated appropriately for different initial spectra. This is particularly an issue here because the different supernovae will not all have the same spectrum in general.

Chapter 7

Conclusions

Neutrinos streaming from powerful astrophysical sources such as SN are so dense near the source that they must show nonlinear flavor oscillations induced by the neutrino-neutrino forward scattering. Numerical simulations reveal a rich variety of phenomena, some of which have been explained with simple analytic models. In this thesis we explore various formal and phenomenological aspects of these phenomena.

Numerical simulations thus far have been restricted to homogeneous gases evolving in time or to sources with exact spherical symmetry. More general geometries are numerically much more demanding and have not yet been studied in great detail. Therefore, we have studied what might be expected under the assumption that the multi-angle instability plays no role and that the neutrino ensemble is largely characterized by self-maintained coherence. In this case one is led to a unique formulation of the nonlinear equations of motion that imply that nonlinear flavor oscillations should be thought of as a one-dimensional phenomenon along the streamlines of the underlying neutrino flux. Close to the source these streamlines are usually curved even though, of course, the underlying neutrino trajectories are straight. (We have neglected the gravitational bending of trajectories.) Therefore, even if the neutrino stream has no global symmetries, the nonlinear oscillation problem is relatively simple.

We have used the concept of “self-maintained coherence” that applies when the neutrino gas is dense, i.e., when a typical neutrino-neutrino interaction energy μ is large

compared to a typical vacuum oscillation frequency $\langle\omega\rangle = \langle\Delta m^2/2E\rangle$. The neutrino ensemble in this case evolves along a streamline as one unit that can be thought of as being one-dimensional. All neutrino and anti-neutrino polarization vectors point essentially in the same direction in flavor space, the pendulum direction, allowing for the simplifications that lead to our nonlinear equations. We have provided a prescription for defining the effective neutrino-neutrino interaction strength μ that works for general source geometries.

We have developed a formalism to analyze neutrino flavor conversion effects in the full three-flavor framework. It employs the Bloch vector representation for 3×3 density matrices, and naturally generalizes the spin-precession analogy to three flavors. In particular, it is capable of describing three-flavor nonlinear neutrino conversion effects inside a core collapse supernova, like synchronized oscillations, bipolar oscillations and spectral split, which have till now been analytically studied mostly in the two-flavor limit.

We explicitly extend the earlier two-flavor analysis of neutrino flavor conversions inside the SN, which includes neutrino-neutrino interactions, to three flavors, where we neglect the CP violation in the neutrino sector. We use the modified flavor basis (ν_e, ν_x, ν_y) , which is rotated from the flavor basis $(\nu_e, \nu_\mu, \nu_\tau)$ so as to get rid of the mixing angle θ_{23} . We also work in the steady state approximation so that there is no explicit time dependence in the density matrix, assume spherical symmetry and half-isotropic neutrino source, and employ the single-angle approximation that has been shown to be valid in the two-flavor case. This leads to the equations of a gyroscope in eight dimensions, similar to the three dimensional gyroscope equations in the two-flavor case.

In the three-flavor formalism, the density matrix is represented by an eight-dimensional Bloch vector \mathbf{P} . However, the flavor content is determined only by the two components P_3 and P_8 of \mathbf{P} after evolution. Motivated by this observation, we propose the “ \mathbf{e}_3 – \mathbf{e}_8 ” triangle diagram to represent the flavor content of any neutrino state by the projection of \mathbf{P} on the \mathbf{e}_3 – \mathbf{e}_8 plane, which we have termed \mathbf{P} . This not only allows us to visualize the three-flavor transformations in a convenient way, but also

allows us to quantify the extent of three-flavor effects over and above the two-flavor results.

A “heavy-light” factorization holds in the three-flavor treatment for certain initial conditions, so that the three-flavor results may be understood as the two-flavor results with Δm_{atm}^2 modified with terms that depend on Δm_{\odot}^2 . Indeed, in certain situations, the three-flavor neutrino conversions may be factorized into three two-flavor oscillations with hierarchical frequencies. In such cases, the three-flavor conversion probabilities may be constructed from two-flavor results by considering the modulation of higher frequency modes by lower frequency modes.

We have compared our analytic results with the numerical ones for simple cases of an initial pure ν_e state, constant matter densities and no nonlinear effects, as well as for synchronized oscillations, and have found a good agreement even when we ignore the modulation due to the lowest frequency. The additional effect of the third neutrino in these cases is limited to the excursions of the orbit of \mathbf{P} towards ν_x . In the absence of nonlinear effects, though the evolution of all energies is different, the orbit of \mathbf{P} can be seen to be an energy-independent quantity. In the synchronized case, neutrinos of all energies are seen to oscillate with a common frequency, and even undergo MSW resonances at the same matter density and with the same adiabaticity.

In the case of bipolar oscillations, the addition of the third neutrino changes the situation significantly. The analytical results are not so easy to obtain, however the numerical results for an inverted hierarchy show a “petal” pattern in the \mathbf{e}_3 – \mathbf{e}_8 triangle, which can be explained by the combination of $\nu_e \leftrightarrow \nu_y$ bipolar oscillations and $\nu_e \leftrightarrow \nu_x$ sinusoidal oscillations. The value of the MSW potential also plays an important role in determining the extent of the effect of the third flavor. This needs to be explored in more detail.

The spectral split occurs in neutrinos in the inverted hierarchy when one starts with ν_e , owing to the unstable position of the eight-dimensional gyroscope in this case. The ν_e above a certain energy, and almost all $\bar{\nu}_e$, completely convert to ν_y and $\bar{\nu}_y$ respectively. There are no additional split effects from the introduction of the third flavor since the hierarchy in the solar sector is normal. This, however, could

change if neutrinos are not in a pure ν_e state as they enter the bipolar region. This is indeed the case sometimes for the MSW prepared spectral splits, in which one gets two spectral splits. The dynamics of the two spectral splits can be understood in terms of the motion of the neutrino state in the \mathbf{e}_3 – \mathbf{e}_8 triangle diagram, which can explain many of the features of neutrino evolution qualitatively. The number of possible splits can be deduced by the location of the neutrino state inside the triangle after passing through the two MSW resonances. We have also shown how the positions of the splits can be calculated accurately given the initial neutrino spectra, and calculated the ν_e survival probability analytically, that matches the numerical computations.

We have simulated the neutrino flavor conversions numerically by taking a realistic density profile for the iron core SN, and have shown the flavor conversions for inverted hierarchy and two θ_{13} values in the cooling phase. In such a scenario, it is easily possible to identify regions where different nonlinear as well as MSW effects dominate. We are able to predict the regions in which these effects take place, and our three-flavor formalism can explain the features of flavor conversions therein. We also point out an interplay between the nonlinear and MSW effects. For example, the H resonance cancels the effect of the spectral split for antineutrinos, whereas the spectral split makes the L resonance irrelevant for neutrinos above the split energy. If the hierarchy were normal, the nonlinear effects would be effectively absent in the cooling phase. These results give us an overall understanding of flavor conversion in SN.

Determination of the leptonic mixing angle θ_{13} and the neutrino mass hierarchy represent two of the next frontiers of neutrino physics. We have proposed a new possibility for identifying the neutrino mass hierarchy that works for extremely small values of θ_{13} , far beyond the sensitivity of current and future terrestrial neutrino experiments. The sensitivity of supernova neutrino oscillations to the mass hierarchy, for incredibly small values of θ_{13} , is a consequence of the nonlinear neutrino oscillations that take place near the supernova core. These effects interchange the initial $\bar{\nu}_e$ and $\bar{\nu}_\mu$ spectra in the inverted hierarchy, which are then further processed by

MSW effects in the SN envelope. This spectral swap can be revealed by comparing the event rate at a shadowed detector with that at an unshadowed detector. If neutrino oscillation experiments fail to determine the mass hierarchy, then this proposed method could represent the last hope to resolve this issue, provided that large water Cherenkov detectors are available at the time of the next galactic SN explosion. This perspective should be considered when choosing optimal detector locations for upcoming large neutrino detectors [130].

We study the prompt ν_e burst in an O-Ne-Mg core collapse SN. Here, the matter density profile is so steep that the sequence between MSW crossings and nonlinear neutrino oscillations is reversed from what would be expected in a traditional iron-core SN. The three-flavor evolution of a ν_e burst dictates that the system first undergoes two MSW level crossings driven by Δm_{atm}^2 and Δm_{\odot}^2 , respectively, and then undergoes spectral splits by the adiabatically decreasing strength of the neutrino-neutrino interaction. Thus we show that the nonlinear effects depends on the progenitor at early times, which could be both a boon or a bane, depending on our detector capabilities.

Observation of the diffuse supernova neutrino background is another cherished goal of the neutrino astrophysicists. Large number of DSNB events are expected in the next generation detectors and therefore, it should be possible to observe DSNB $\bar{\nu}_e$ in the future. nonlinear effects inside SN significantly change the predicted number of DSNB events if the hierarchy is inverted. We point out that the prediction for the DSNB flux should thus be revised by taking into account these effects. Conversely, if the DSNB is observed, one will have to account for nonlinear effects while placing bounds on various parameters.

We believe that these results will contribute towards a better understanding of the neutrino masses and mixing, as well as supernova astrophysics and cosmology.

Bibliography

- [1] Amsler, C. et al. *Phys. Lett.* **B667**, 1 (2008). [1](#), [2](#)
- [2] Pontecorvo, B. *Sov. Phys. JETP* **7**, 172 (1958). [1](#)
- [3] Maki, Z., Nakagawa, M., and Sakata, S. *Prog. Theor. Phys.* **28**, 870 (1962).
[1](#)
- [4] Bilenky, S. M. and Pontecorvo, B. *Phys. Rept.* **41**, 225 (1978). [2](#)
- [5] Wolfenstein, L. *Phys. Rev.* **D17**, 2369 (1978). [3](#)
- [6] Mikheev, S. P. and Smirnov, A. Y. *Sov. J. Nucl. Phys.* **42**, 913 (1985). [3](#)
- [7] Landau, L. D. *Phys. Z. Sowjetunion.* **2**, 46 (1932). [3](#)
- [8] Zener, C. *Proc. Roy. Soc. Lond.* **A137**, 696 (1932). [3](#)
- [9] Pantaleone, J. T. *Phys. Rev.* **D46**, 510 (1992). [3](#), [12](#)
- [10] Pantaleone, J. T. *Phys. Lett.* **B287**, 128 (1992). [3](#), [12](#)
- [11] Schwetz, T., Tortola, M., and Valle, J. W. F. *New J. Phys.* **10**, 113011 (2008).
[4](#)
- [12] Hannestad, S., Mirizzi, A., Raffelt, G. G., and Wong, Y. Y. Y. *JCAP* **0804**,
019 (2008). [4](#)
- [13] Raffelt, G. G. *Stars as Laboratories for Fundamental Physics : The
Astrophysics of Neutrinos, Axions, and Other Weakly Interacting Particles
(Theoretical Astrophysics)*. University Of Chicago Press, (1996). [5](#), [8](#)

- [14] Kitaura, F. S., Janka, H.-T., and Hillebrandt, W. *Astron.Astrophys.* **450**, 345–350 April (2006). [5](#), [75](#)
- [15] Baade, W. and Zwicky, F. *Proceedings of the National Academy of Science* **20**, 254 (1934). [5](#)
- [16] Brown, G. E., Bethe, H. A., and Baym, G. *Nucl. Phys. A* **375**, 481 (1982). [5](#)
- [17] Colgate, S. A. and White, R. H. *Astrophys. J.* **143**, 626 (1966). [6](#)
- [18] Bethe, H. A. and Wilson, James, R. *Astrophys. J.* **295**, 14 (1985). [6](#)
- [19] Bethe, H. A. *Rev. Mod. Phys.* **62**, 801 (1990). [6](#)
- [20] Janka, H.-T., Langanke, K., Marek, A., Martinez-Pinedo, G., and Mueller, B. *Phys. Rept.* **442**, 38 (2007). [6](#)
- [21] Tomas, R. et al. *JCAP* **0409**, 015 (2004). [6](#), [7](#), [12](#), [63](#), [74](#)
- [22] Odrzywolek, A., Misiaszek, M., and Kutschera, M. *Astropart. Phys.* **21**, 303 (2004). [6](#)
- [23] Totani, T., Sato, K., Dalhed, H. E., and Wilson, J. R. *Astrophys. J.* **496**, 216 (1998). [9](#), [10](#), [59](#), [70](#), [73](#)
- [24] Keil, M. T., Raffelt, G. G., and Janka, H.-T. *Astrophys. J.* **590**, 971 (2003). [9](#), [59](#), [70](#), [72](#)
- [25] Hirata, K. et al. *Phys. Rev. Lett.* **58**, 1490 (1987). [9](#)
- [26] Bionta, R. M. et al. *Phys. Rev. Lett.* **58**, 1494 (1987). [9](#)
- [27] Diehl, R. et al. *Nature* **439**, 45 (2006). [10](#), [79](#)
- [28] Dighe, A. *J. Phys. Conf. Ser.* **136**, 022041 (2008). [10](#)
- [29] Bisnovatyi-Kogan, G. S. and Seidov, Z. F. *Soviet Astronomy* **26**, 132 April (1982). [10](#), [79](#)

- [30] Krauss, L. M., Glashow, S. L., and Schramm, D. N. *Nature* **310**, 191 (1984).
[10](#), [79](#)
- [31] Horiuchi, S., Beacom, J. F., and Dwek, E. *arXiv:astro-ph/0812.3157* (2008).
[10](#)
- [32] Malek, M. et al. *Phys. Rev. Lett.* **90**, 061101 (2003). [10](#), [80](#), [82](#)
- [33] Fuller, G. M., Mayle, R. W., Wilson, J. R., and Schramm, D. N. *Astrophys. J.* **322**, 795 November (1987). [12](#)
- [34] Dighe, A. S. and Smirnov, A. Y. *Phys. Rev.* **D62**, 033007 (2000). [12](#), [15](#), [63](#),
[70](#)
- [35] Lunardini, C. and Smirnov, A. Y. *JCAP* **0306**, 009 (2003). [12](#), [63](#)
- [36] Dighe, A. S., Keil, M. T., and Raffelt, G. G. *JCAP* **0306**, 005 (2003). [12](#), [63](#),
[74](#)
- [37] Dighe, A. S., Keil, M. T., and Raffelt, G. G. *JCAP* **0306**, 006 (2003). [12](#), [63](#),
[74](#)
- [38] Dighe, A. S., Kachelriess, M., Raffelt, G. G., and Tomas, R. *JCAP* **0401**, 004
(2004). [12](#), [63](#)
- [39] Schirato, R. C. and Fuller, G. M. *arXiv:astro-ph/0205390* (2002). [12](#), [63](#)
- [40] Takahashi, K., Sato, K., Dalhed, H. E., and Wilson, J. R. *Astropart. Phys.*
20, 189 (2003). [12](#), [63](#)
- [41] Fogli, G. L., Lisi, E., Montanino, D., and Mirizzi, A. *Phys. Rev.* **D68**, 033005
(2003). [12](#), [60](#), [63](#)
- [42] Fogli, G. L., Lisi, E., Mirizzi, A., and Montanino, D. *JCAP* **0504**, 002 (2005).
[12](#), [63](#), [73](#), [74](#)
- [43] Barger, V., Huber, P., and Marfatia, D. *Phys. Lett.* **B617**, 167 (2005). [12](#), [63](#)
- [44] Dasgupta, B. and Dighe, A. *Phys. Rev.* **D75**, 093002 (2007). [12](#), [63](#)

- [45] Fogli, G. L., Lisi, E., Mirizzi, A., and Montanino, D. *JCAP* **0606**, 012 (2006).
[12](#), [63](#), [74](#)
- [46] Choubey, S., Harries, N. P., and Ross, G. G. *Phys. Rev.* **D74**, 053010 (2006).
[12](#), [63](#)
- [47] Friedland, A. and Gruzinov, A. *arXiv:astro-ph/0607244* (2006). [12](#), [63](#)
- [48] Kneller, J. P., McLaughlin, G. C., and Brockman, J. *Phys. Rev.* **D77**, 045023 (2008). [12](#)
- [49] Minakata, H., Nunokawa, H., Tomas, R., and Valle, J. W. F. *JCAP* **0812**, 006 (2008). [12](#)
- [50] Fogli, G. L., Lisi, E., Mirizzi, A., and Montanino, D. *Phys. Rev.* **D66**, 013009 (2002). [12](#)
- [51] Choubey, S., Harries, N. P., and Ross, G. G. *Phys. Rev.* **D76**, 073013 (2007).
[12](#)
- [52] Thomson, M. J. and McKellar, B. H. J. *Phys. Lett.* **B259**, 113 (1991). [12](#), [17](#)
- [53] Sigl, G. and Raffelt, G. *Nucl. Phys.* **B406**, 423 (1993). [12](#), [16](#), [17](#)
- [54] McKellar, B. H. J. and Thomson, M. J. *Phys. Rev.* **D49**, 2710 (1994). [12](#), [17](#)
- [55] Samuel, S. *Phys. Rev.* **D48**, 1462 (1993). [12](#)
- [56] Kostelecky, V. A. and Samuel, S. *Phys. Rev.* **D52**, 621 (1995). [12](#)
- [57] Pantaleone, J. T. *Phys. Rev.* **D58**, 073002 (1998). [12](#), [13](#)
- [58] Samuel, S. *Phys. Rev.* **D53**, 5382 (1996). [12](#)
- [59] Pastor, S., Raffelt, G. G., and Semikoz, D. V. *Phys. Rev.* **D65**, 053011 (2002).
[12](#), [35](#)
- [60] Hannestad, S., Raffelt, G. G., Sigl, G., and Wong, Y. Y. Y. *Phys. Rev.* **D74**, 105010 (2006). [12](#), [32](#), [35](#), [46](#), [47](#), [50](#)

- [61] Duan, H., Fuller, G. M., Carlson, J., and Qian, Y.-Z. *Phys. Rev.* **D75**, 125005 (2007). [12](#), [35](#), [46](#), [47](#), [50](#)
- [62] Raffelt, G. G. and Smirnov, A. Y. *Phys. Rev.* **D76**, 081301 (2007). [12](#), [22](#), [35](#), [49](#), [50](#), [74](#)
- [63] Raffelt, G. G. and Smirnov, A. Y. *Phys. Rev.* **D76**, 125008 (2007). [12](#), [35](#), [49](#), [50](#)
- [64] Pantaleone, J. T. *Phys. Lett.* **B342**, 250 (1995). [13](#)
- [65] Qian, Y. Z. and Fuller, G. M. *Phys. Rev.* **D51**, 1479 (1995). [13](#)
- [66] Sigl, G. *Phys. Rev.* **D51**, 4035 (1995). [13](#)
- [67] Pastor, S. and Raffelt, G. *Phys. Rev. Lett.* **89**, 191101 (2002). [13](#)
- [68] Balantekin, A. B. and Yuksel, H. *New J. Phys.* **7**, 51 (2005). [13](#)
- [69] Fuller, G. M. and Qian, Y.-Z. *Phys. Rev.* **D73**, 023004 (2006). [13](#), [23](#)
- [70] Duan, H., Fuller, G. M., and Qian, Y.-Z. *Phys. Rev.* **D74**, 123004 (2006). [13](#), [18](#)
- [71] Duan, H., Fuller, G. M., and Qian, Y.-Z. *Phys. Rev.* **D76**, 085013 (2007). [13](#)
- [72] Duan, H., Fuller, G. M., Carlson, J., and Qian, Y.-Z. *Phys. Rev.* **D74**, 105014 (2006). [13](#), [18](#), [21](#), [58](#)
- [73] Duan, H., Fuller, G. M., Carlson, J., and Qian, Y.-Z. *Phys. Rev. Lett.* **97**, 241101 (2006). [13](#), [21](#)
- [74] Raffelt, G. G. and Sigl, G. *Phys. Rev.* **D75**, 083002 (2007). [13](#)
- [75] Esteban-Pretel, A., Pastor, S., Tomas, R., Raffelt, G. G., and Sigl, G. *Phys. Rev.* **D76**, 125018 (2007). [13](#), [14](#), [21](#), [24](#), [74](#)
- [76] Fogli, G. L., Lisi, E., Marrone, A., and Mirizzi, A. *JCAP* **0712**, 010 (2007). [13](#), [21](#), [24](#), [61](#), [63](#), [74](#)

- [77] Esteban-Pretel, A., Pastor, S., Tomas, R., Raffelt, G. G., and Sigl, G. *Phys. Rev. D* **77**, 065024 (2008). [13](#), [17](#)
- [78] Dasgupta, B. and Dighe, A. *Phys. Rev. D* **77**, 113002 (2008). [13](#)
- [79] Duan, H., Fuller, G. M., and Qian, Y.-Z. *Phys. Rev. D* **77**, 085016 (2008). [13](#), [50](#)
- [80] Dasgupta, B., Dighe, A., Mirizzi, A., and Raffelt, G. G. *Phys. Rev. D* **77**, 113007 (2008). [13](#), [50](#)
- [81] Gava, J. and Volpe, C. *Phys. Rev. D* **78**, 083007 (2008). [13](#)
- [82] Dasgupta, B., Dighe, A., Mirizzi, A., and Raffelt, G. G. *Phys. Rev. D* **78**, 033014 (2008). [13](#)
- [83] Blennow, M., Mirizzi, A., and Serpico, P. D. *Phys. Rev. D* **78**, 113004 (2008). [13](#)
- [84] Duan, H., Fuller, G. M., Carlson, J., and Zhong, Y.-Q. *Phys. Rev. Lett.* **99**, 241802 (2007). [13](#), [74](#)
- [85] Dasgupta, B., Dighe, A., and Mirizzi, A. *Phys. Rev. Lett.* **101**, 171801 (2008). [13](#)
- [86] Duan, H., Fuller, G. M., Carlson, J., and Qian, Y.-Z. *Phys. Rev. Lett.* **100**, 021101 (2008). [13](#), [76](#), [77](#)
- [87] Lunardini, C., Muller, B., and Janka, H. T. *Phys. Rev. D* **78**, 023016 (2008). [13](#)
- [88] Chakraborty, S., Choubey, S., Dasgupta, B., and Kar, K. *JCAP* **0809**, 013 (2008). [13](#)
- [89] Kostelecky, V. A., Pantaleone, J. T., and Samuel, S. *Phys. Lett.* **B315**, 46 (1993). [13](#)
- [90] Kostelecky, V. A. and Samuel, S. *Phys. Lett.* **B318**, 127 (1993). [13](#)

- [91] Kostelecky, V. A. and Samuel, S. *Phys. Rev.* **D49**, 1740 (1994). 13
- [92] Kostelecky, V. A. and Samuel, S. *Phys. Lett.* **B385**, 159 (1996). 13
- [93] Dolgov, A. D. et al. *Nucl. Phys.* **B632**, 363 (2002). 13
- [94] Wong, Y. Y. Y. *Phys. Rev.* **D66**, 025015 (2002). 13, 44, 45, 46
- [95] Wong, Y. Y. Y. *AIP Conf. Proc.* **655**, 240 (2003). 13, 44, 45, 46
- [96] Abazajian, K. N., Beacom, J. F., and Bell, N. F. *Phys. Rev.* **D66**, 013008 (2002). 13, 46
- [97] Fogli, G. L., Lisi, E., Marrone, A., Mirizzi, A., and Tamborra, I. *Phys. Rev.* **D78**, 097301 (2008). 14
- [98] Cardall, C. Y. *Phys. Rev.* **D78**, 085017 (2008). 18
- [99] Kimura, G. and Kossakowski, A. *Open Systems & Information Dynamics* **12**(3), 207 (2005). 27
- [100] Kim, C. W., Kim, J., and Sze, W. K. *Phys. Rev.* **D37**, 1072 (1988). 31
- [101] Hindmarsh, A. C., Brown, P. N., Grant, K. E., Lee, S. L., Serban, R., Shumaker, D. E., and Woodward, C. S. *ACM Transactions on Mathematical Software* **31**(3), 363–396 September (2005). Also see the webpage <https://computation.llnl.gov/casc/sundials/main.html>. 40
- [102] Raffelt, G. G. *Phys. Rev.* **D78**, 125015 (2008). 44
- [103] Fogli, G. L., Lisi, E., Montanino, D., and Palazzo, A. *Phys. Rev.* **D65**, 073008 (2002). 70
- [104] Lunardini, C. and Smirnov, A. Y. *Nucl. Phys.* **B616**, 307 (2001). 71
- [105] Raffelt, G. G., Keil, M. T., Buras, R., Janka, H.-T., and Rampp, M. *arXiv:astro-ph/0303226* (2003). 72
- [106] Autiero, D. et al. *JCAP* **0711**, 011 (2007). 72, 74

- [107] Jung, C. K. *AIP Conf. Proc.* **533**, 29 (2000). [72](#)
- [108] Nakamura, K. *Int. J. Mod. Phys.* **A18**, 4053 (2003). [72](#)
- [109] Halzen, F. *Eur. Phys. J.* **C46**, 669 (2006). [73](#)
- [110] de Gouvea, A. and Winter, W. *Phys. Rev.* **D73**, 033003 (2006). [74](#)
- [111] Kachelriess, M. et al. *Phys. Rev.* **D71**, 063003 (2005). [74](#)
- [112] Gil Botella, I. and Rubbia, A. *JCAP* **0310**, 009 (2003). [74](#)
- [113] Nomoto, K. *Astrophys. J.* **277**, 791 February (1984). [75](#)
- [114] Nomoto, K. *Astrophys. J.* **322**, 206 November (1987). [75](#)
- [115] Janka, H.-T., Müller, B., Kitaura, F. S., and Buras, R. *Astron.Astrophys.* **485**, 199–208 July (2008). [75](#)
- [116] Ando, S. and Sato, K. *New J. Phys.* **6**, 170 (2004). [80](#), [81](#)
- [117] Ando, S. *Astrophys. J.* **607**, 20 (2004). [80](#)
- [118] Wurm, M. et al. *Phys. Rev.* **D75**, 023007 (2007). [80](#)
- [119] Cocco, A. G., Ereditato, A., Fiorillo, G., Mangano, G., and Pettorino, V. *JCAP* **0412**, 002 (2004). [80](#)
- [120] Beacom, J. F. and Strigari, L. E. *Phys. Rev.* **C73**, 035807 (2006). [80](#)
- [121] Lunardini, C. *Phys. Rev.* **D73**, 083009 (2006). [80](#)
- [122] Volpe, C. and Welzel, J. *arXiv:astro-ph/0711.3237* (2007). [80](#)
- [123] Aglietta, M. et al. *Astropart. Phys.* **1**, 1 (1992). [80](#)
- [124] Lunardini, C. and Peres, O. L. G. *JCAP* **0808**, 033 (2008). [80](#)
- [125] Beacom, J. F. and Vagins, M. R. *Phys. Rev. Lett.* **93**, 171101 (2004). [80](#)
- [126] Strigari, L. E., Beacom, J. F., Walker, T. P., and Zhang, P. *JCAP* **0504**, 017 (2005). [81](#), [82](#)

- [127] Baldry, I. K. and Glazebrook, K. *Astrophys. J.* **593**, 258 (2003). [81](#)
- [128] Hopkins, A. M. and Beacom, J. F. *Astrophys. J.* **651**, 142 (2006). [82](#)
- [129] Kistler, M. D., Yuksel, H., Beacom, J. F., and Stanek, K. Z. *Astrophys. J.* **673**, L119 (2008). [82](#)
- [130] Mirizzi, A., Raffelt, G. G., and Serpico, P. D. *JCAP* **0605**, 012 (2006). [89](#)

